UNIVERSITÀ DEGLI STUDI DI NAPOLI FEDERICO II

PHD PROGRAM IN EARTH, ENVIRONMENT AND RESOURCES SCIENCES

XXXVI Cycle

PhD Thesis

Realization of an Unmanned Aircraft Magnetometer System

PhD candidate

Filippo Accomando

Advisor:

Prof. Giovanni Florio

Al mio papà

CONTENTS

ABSTRACT

The use of drones has become a reliable strategy that can replace conventional high-altitude manned and ground surveys for most magnetic method applications, thanks to numerous technical reasons. However, to be considered a new viable acquisition approach, this research field has to deal some key issues of primary interest. Therefore, a study aimed at describing the solutions to find the correct employment of this new strategy helps to prove the real advantages with respect to common ground and high-altitude surveying methods.

The main goal of this thesis is to conduct aeromagnetic surveys using unmanned aerial vehicle (UAV). Specifically, the feasibility of a Micro-Fabricated Atomic Magnetometer (MFAM) integrated on multi-rotor UAVs is studied, and several flight designs are investigated, as well as workflow possibilities for optimal data analysis and processing. Despite a large and recent amount of literature available on UAV-borne aeromagnetic systems, this thesis provides original contributions useful for considering this technique as a new trusted geophysical surveying method presenting magnetic investigations of different interest.

Endmembers of two flight configurations, favoring the stability of the system during flight or the minimization of the mobile platform noise, were compared. Results demonstrate that careful processing can return high quality drone-borne data using both flight configurations. The optimal flight solution can be chosen depending on the survey target and flight conditions.

These conclusions allow planning a UAV magnetic survey to map a magmatic dike embedded and scattered among the high vertical steps of a calcareous quarry, whereas outside the excavated area, the steep mountain slope covered by dense bush vegetation makes direct inspection and geological mapping a challenging task. Extremely rugged terrain made the UAV-based magnetic survey the preferred acquisition strategy.

For the first time, a vertical gradient configuration for UAV surveying was designed and compared with terrestrial datasets in different archaeological sites of interest using the MFAM. The results indicate that UAV-borne aeromagnetic systems, even in a vertical gradient configuration, can replace the high quality and resolution typical of conventional terrestrial surveys.

The thesis presents a variety of applications conducted over sites of geological, archaeological, and engineering interest, through different solutions of flight design and sensor integration. The document provides valuable insights for the correct deployment of UAV technologies for magnetic surveys and their future developments.

Preface

This thesis is a manuscript that includes two co-authored papers published in peer-reviewed scientific journals. The document represents the original work of the author under the supervision of Prof. Giovanni Florio, who is also a co-author of the articles listed below:

1. *Accomando, F.; Vitale, A.; Bonfante, A.; Buonanno, M.; Florio, G. Performance of Two Different Flight Configurations for Drone-Borne Magnetic Data. Sensors 2021, 21, 5736.* **(Published- Chapter 4.1).**

2. *Accomando, F., Bonfante, A., Buonanno, M., Natale, J., Vitale, S., & Florio, G. The drone-borne magnetic survey as the optimal strategy for high-resolution investigations in presence of extremely rough terrains: The case study of the Taverna San Felice quarry dike. Journal of Applied Geophysics,2023, 217, 105186.* **(Published- Chapter 4.2).**

For papers 1-2, the author and the supervisor G. Florio acquired and processed the magnetic datasets and then wrote the articles. For paper 1, A. Vitale, A. Bonfante, and M. Buonanno planned and executed the drone flight. For paper 2, A. Bonfante, and M. Buonanno planned and executed the drone flight, while J. Natale and A. Vitale provided all the geological information of the site.

The research findings collected in this manuscript were presented at national and international conferences, where the author received two awards, listed below, as a young researcher for the original contents of his research.

1. **AGLC 'Licio Cernobori' award –** during the *41° GNGTS, 7-9 February 2023* - sponsored by Italian section EAGE-SEG.

2. **'Simone Frigerio'** award – during the *XVII GIT National meeting, 11-13 September 2023* – sponsored by GeoSoul Italia SRL, Hortus SRL, and Symple SRL.

List of Abbreviations

AC alternating current

AGL above ground level

ASL above sea level

DC direct current

DEM digital elevation model

DJI dà-jiāng innovations

EAGE European association of geoscientists and Engineers

GEM geophysical electromagnetic

GIT Geosciences & Information Technologies

GNSS global navigation satellite system

GPR ground penetrating radar

GPS global positioning system

IGRF international geomagnetic reference field

LiPo lithium polymer

MAD-XR Magnetic Anomaly Detection Extended Role

MATLAB matrix laboratory

MGT mobile Geophysical Technologies

OPM optically Pumped Alkali Vapor Magnetometers

RPAS remotely piloted aircraft system

SEG society of exploration geophysicists

SI International System of Units

TMI total magnetic intensity

UAS unmanned aerial systems

UAV unmanned aerial vehicle

USGS United States geologic survey

UXO unexploded ordinance

VLF very low frequency

3D three dimensional

Introduction

Geophysical methods are the primary way to study the Earth through its physical properties. Among these methods, magnetometry surveys passively sense the total magnetic intensity (TMI) and investigate the spatial distribution of magnetized sources such as rocks or mineral deposits, buried ferrous metal objects, and archaeological remains. The magnetic method is fast, reliable, and cheap, and is widely used in near-surface geophysics. Recent technological advances have opened up new data acquisition possibilities, revolutionizing traditional investigation strategies.

In the past, manned airborne and terrestrial surveys were the only exploration methods used. However, both have physical constraints that limit data collection. Planes or helicopters can cover large areas with flights at or above altitudes of 50-100 m but are characterized by low resolution. On the contrary, ground surveys provide high-resolution datasets over very small areas limited to the Earth's surface but may be limited in access and costly in time.

In recent years, an intermediate solution has been introduced by the use of Unmanned Aerial Vehicles (UAVs), also known as remotely piloted aircraft systems (RPAS), model aircraft, remote control aircraft, or drones. Among them, Unmanned Aircraft Systems (UASs) are the most commonly used names that consider all the components mounted on-board, such as sensors, as well as all other ground support elements needed for the flight and/or acquisition. However, their applicability has limitations due to UAV flight regulations and protocols, mainly pertaining to altitude or minimum distance to maintain from urbanized areas, which change between jurisdictions and countries.

UAVs have become standard tools for acquiring spatial data to support various geoscientific analyses, reducing the cost and time necessary to complete a survey, and allowing extension of the prospections even over places of difficult access, while limiting the risks for field personnel. Several geophysical instruments have been mounted on UAVs as payloads, including hyperspectral cameras, magnetometers, radar antennas, gamma-ray detectors, and Very Low Frequency (VLF) sensors, opening the possibility of doing "drone geophysics". In the magnetic case, which will be the geophysical method focused on throughout this thesis, UAV and magnetometers were integrated in a variety of systems thanks to the development of miniaturized, lightweight magnetic sensors and acquisition boards. The integration of UAV and magnetometers is opening new perspectives to the search and modeling of shallow magnetized sources. The possible fields of applications include topics of primary interest today, such as the field of mining exploration, the identification of active faults, or other geological targets. Drone magnetometry also has its role in engineering applications, such as archaeogeophysics and the preliminary studies to the decommissioning of oil industry infrastructures.

To implement a UAV magnetic system, it is necessary to find solutions to technical challenges such as UAV-borne electromagnetic interferences. Scientific literature provides insights to mitigate this noise that operate both in real time, positioning the sensors far enough from the aerial platforms, and in post-processing through the use of spectral filtering.

In this thesis, we frequently refer to the "UAV-borne aeromagnetic system" as the combination of 1) the flight platform used; 2) the suspended magnetometer payload; and 3) all the ancillary elements on-board. In our studies, we always used multi-rotor UAVs, which have been described in numerous studies over the last decade as the most dominant vehicle solution for magnetic surveying due to their functionality and varieties. We mounted these UAVs with the Micro-Fabricated Atomic Magnetometer (MFAM). We designed several flight solutions and acquisition strategies to collect geological, archaeological, and engineering datasets of good quality. We improved a versatile solution that can replace traditional acquisition strategies while maintaining their advantages. All data analysis and processing were performed by us using tools developed in MATLAB, which were customized according to the characteristics of the target of interest.

Research Objectives

The primary objective of this thesis is to develop and evaluate a versatile UAV-borne aeromagnetic system for improved target characterization of magnetic interest. We conducted an in-depth analysis of flight designs and magnetometer-platform integration methods. In this work, we propose several studies to demonstrate how UAV-borne aeromagnetic systems can become a reliable way of investigation, able to replace traditional exploration techniques for a wide variety of applications. Each study highlights the main key issues that could change depending on the target, and how to address them both from a technical and data processing point of view. We show that different approaches are needed to achieve good quality and data resolution.

The main objectives of this thesis are:

1. Develop a versatile UAV-borne aeromagnetic system for improved target characterization of magnetic interest.
2. The compensation of the fields induced by the mobile platform, to be realized from a structural point of view (realization of an aerodynamic housing (bird); choice of the optimal structure to tie the bird to the drone ; choice of the optimal distance from the vehicle), from the point of view of noise estimation for different sensors attitude (pitch, roll, yaw), and, finally, from the point of view of filtering of the recorded signals.
3. Demonstrate that fixing the MAFM directly to the drone landing gear, at 0.5 m only from the engines, could be the most stable and safest solution for high intensity or amplitude magnetic anomalies expected.
4. Describe the acquisition, processing, and interpretation of magnetic data collected over area of geological, archaeological, and engineering interest.
5. Implement, for the first time with MFAM, a vertical gradient configuration both for UAV and ground survey, evaluating the optimal distance between the sensors for estimating the spatial gradients of the total magnetic field.

Thesis outline and original contributions

The scientific literature is rich of innovative approaches which rapidly evolve in the field of UAV-borne aeromagnetic surveying. However, this thesis provides original contributions that could play a key role in the near future. Several individual publications collected in this work were already cited and presented at main national international conferences.

In *Chapter 1,* we recall the basic principles of the magnetic method. We briefly describe its nature and how it is used for exploration in geosciences.

In *Chapter 2,* we provide a large description of the magnetometers and unmanned platforms most used for the implementation of an UAV-borne aeromagnetic system. The technical background about the main fields of interest and solutions find by other studies in the last two decades are presented. A particular focus is given on the multi-rotor UAV configurations implemented since they are the same vehicles use for our investigations.

In *Chapter 3*, we describe all the elements with which we implemented our UAV-borne aeromagnetic system. We started presenting the main specifications of the MFAM and how some of these are important for the compensation of the magnetic and electromagnetic interference due to the drone and its motors. The Chapter provides the first innovative contributions of our studies. In fact, we show custom birds built to house the magnetometer, how to choose the most appropriate configuration, and the different ways to integrate them with the UAVs.

In *Chapter 4*, through several studies, we present a final overview of the main results obtained by our UAV-borne aeromagnetic system. In the first study (Chapter 4.1), we tried an unusual flight configuration, mounting the MFAM directly to the drone landing gear, very close to the engines, for the investigation of buried metal pipelines. In most cases, this solution is avoided since the magnetometer is located in the electromagnetic interference area caused by the platform. However, the result was similar to the ones acquired with the sensors suspended 3 m below the vehicle and demonstrated a comparable sensitivity with a terrestrial magnetic dataset. We concluded that the magnetometer fixed directly to the UAV is a practical and safe solution in the case of high amplitude magnetic anomalies even if a heavy filtering is needed. The benefits of this research helped us in the second case study aimed to map an igneous dike hosted in carbonates rocks (Chapter 4.2). The hazardous ground conditions and the impossibility to plan a ground survey, give an example of how essential the implementation of a UAV-borne aeromagnetic system which become the only practicable strategy in some conditions. We performed a second geological survey by conducting a drone borne magnetic survey, as a complementary exploration method, to define the basement geometry or even the fault trace along the S. Gregorio Magno basin for the high-resolution geophysical investigation of the third segment surface rupture of the Irpinia Fault. Sections 4.4 through 4.6 are dedicated to the archaeological prospections. Usually, archaeological targets are characterized by typical weak magnetic anomalies which forced us to relocate the magnetometer out from the zone of drone interference. However, as technical original contribution, we tried the first attempt of vertical gradient measurement using the MFAM, both for UAV and ground surveys.

Although it may be difficult to imagine that a UAV-borne aeromagnetic system could replace the sensitivity of terrestrial acquisitions or provide results with similar detail, this thesis provides detailed evidence of its effectiveness and reliability.

Chapter 1 – Magnetic Method

The magnetic method is one of the oldest and most widely used techniques in geophysical exploration due to its reliable, fast, and non-invasive applicability. The surveys have the aim to map and model the subsurface magnetized sources. Magnetic anomalies are variations of the Earth’s local magnetic field resulting from the magnetic properties of underlying rocks and minerals contained in ferrous metal objects. Most minerals that compose a rock are non-magnetic; however, there are some minerals that have sufficient magnetic susceptibility to cause an increase or decrease of the local magnetic field on or near the surface of the Earth when interacting with an ambient magnetic field (Earth's).

Magnetic surveying is performed to investigate the subsurface to improve the understanding of the regional or local geological setting and history, or to identify potential economic resources. Traditional surveys are conducted on the ground or at high altitude through manned systems. However, the introduction of drones has represented a new opportunity thanks to the high sensitivity and light-weight of present-day magnetometers that are able to detect even the weakest targets.

In this chapter, we briefly describe the nature of the geomagnetic field, the concept of magnetization, and its main mathematical expressions.

1.1 Origins of the measured geomagnetic field

Due to chemical differentiation and radioactive heating, the electrically conductive fluid of the Earth’s outer iron core is in a continual state of convection. The geodynamo theory explains how the fluid motion generates and maintain a magnetic field (e.g., Ranalli, 1995). Thanks to this process, the kinetic energy of the outer core is converted to electrical and magnetic energy. This is a self-sustaining in which the fluid motion generates electric currents that cause their own magnetic fields. The Earth’s magnetic field could be well approximated to that produced by a magnetic dipole with an inclination of about 11° with respect to the Earth's rotational axis.

The magnetic data acquired by magnetometers are the sum of several contributions: 1) *main field* due to the conductive fluid motion in the outer core (mentioned above); 2) *lithospheric field* caused by the magnetized rocks of the lithosphere; 3) *external fields* generated by the electric currents in the ionosphere and in the magnetosphere. The *main field*, the largest magnetic field contribution, can undergo long-term variations called *secular variation* related to change in the Earth's interior (e.g., Lanza and Meloni, 2006). Its value is modeled by the International Geomagnetic Reference Field (IGRF) by the International Association of Geomagnetism and Aeronomy (IAGA) and updated every 5 years. The *lithospheric field* is associated to both the magnetized subsurface rocks and anthropogenic materials. This contribution includes the induced and remanent magnetizations of rocks acquired under the induction of the Earth's main magnetic field. It represents the component of interest of magnetic surveys. Finally, *external fields* are due to the solar wind interaction with the magnetosphere and with atmospheric activity and are characterized by short-time variations. These are also known as diurnal variations and are removed from the measured magnetic data.

1.2 Magnetic field and rocks magnetic properties

The magnetic field, like the gravitational one, are potential fields that follow the Laplace's equation in the mass-free space for which the sum of the field gradient variation rates in the three orthogonal directions is zero (Kearey et al., 2002).

The Laplace's equation, in Cartesian coordinates, is the following:

$$\frac{\partial^2 \varphi}{\partial x^2} + \frac{\partial^2 \varphi}{\partial y^2} + \frac{\partial^2 \varphi}{\partial z^2} = 0 \quad \textbf{(1.1)}$$

where φ is referred to the magnetic (or gravitational) field and is a function of (x,y,z).

(The following synthesis is largely taken from the Gravity and Magnetic Encyclopedic Dictionary, by S. Goussev (2022)). The natural process that occurs when rocks are exposed to an external magnetic field, such as the Earth's magnetic field, and become magnetized, producing their own magnetic fields is known as *Magnetic Induction* (**B**). It is a vector quantity that measures the strength and direction of the magnetic field resulting from rock magnetization by the externally applied, or inducing, magnetic field. **B** is represented by the vector sum of two fields: (1) the internal magnetic field (i.e. magnetic field induced into the rock material), and (2) the *magnetizing force* **H,** a vector quantity which is a measure of the strength, or intensity, of the external magnetic field that defines magnetization of rocks. **H,** defined also as *magnetizing field intensity,* is defined by gradient of magnetic potential, and is measured in units of *ampere* per meter ($A \cdot m^{-1}$) in the SI system (where $1\ A \cdot m^{-1} = 4\pi \cdot 10^{-3}$ Oe). **B** and **H** are related by the following equation in the SI system:

$$B = \mu H \quad \textbf{(1.2)}$$

where "μ" is the *magnetic permeability* of a rock and is expressed as:

$$\mu = \mu_0 (1 + k) \quad \textbf{(1.3)}$$

where "k" is magnetic susceptibility, and "μ_0" is magnetic permeability of a source-free space.

Total magnetic induction vector is defined as:

$$B = \mu_0 (H + M) \quad \textbf{(1.4)}$$

where **M** is the magnetization induced by the external magnetic field into the rock material, i.e. *induced magnetization.* The direction and magnitude of the magnetic vector at any point in the space outside the magnetic media is described by gradient of the scalar potential as following:

$$B = -\Delta V \quad \textbf{(1.5)}$$

where "Δ" is gradient operator, "V" is magnetic potential, and minus sign follows the theoretical convention. In terms of *magnetic anomaly*, magnetic induction is defined as:

$$B = B_0 + \Delta \mathrm{B} \quad \textbf{(1.6)}$$

where "B_0" is the Earth magnetic field, or ambient field, and "ΔB" is the anomalous magnetic induction component caused by source body.

The SI unit used for the magnetic field amplitude is Tesla (T) which is too large to indicate the small anomalies generated by rock and anthropogenic objects. Usually, the subunit nanoTesla (nT) is preferred and is defined as: 1 nT = 10^{-9} tesla = 10^{-9} weber·m^{-2} = 10^{-5} gauss. The geomagnetic field ranges from a minimum of 25000 nT in equatorial regions to about 70000 nT at the poles (Kearey et al., 2002). Magnetic induction is referred to with the same meaning as *magnetic field* and *magnetic flux density*.

The lithospheric field, as said above, is generated by the magnetized crustal and upper mantle rocks and varies depending on mineral composition, geographical regions, and geothermal gradients. The magnetic characteristics of a rock allow to classification of magnetic materials in 3 main classes (e.g., Reynolds, 1977):

- *Diamagnetic* materials which have a negative and weak susceptibility since the applied magnetic field produces a magnetization antiparallel to itself;

- *Paramagnetic* materials have a small, positive susceptibility. In fact, the application of a magnetic field produces a parallel and partial alignment of the magnetic moments with the consequence of a magnetization in the same direction of the applied field. However, if the magnetic field is removed, thermal effects disturb the magnetic moment and the alignment vanish. Both diamagnetic and paramagnetic materials do not contribute significatively to the geomagnetic field;

- *Ferromagnetic* materials are the class of greatest importance for the large and positive susceptibility exhibited to an external magnetic field applied and for the ability to maintain the magnetic properties if the magnetic field is removed. In these materials, neighboring moments interact with each other under the effect called exchange energy which is able to produce spontaneous magnetization many times greater than the materials listed above. The mode of alignment allows a second classification of these materials in: 1) ferromagnetic proper if all the moments are aligned parallel between them; 2) antiferromagnetic if the alignment is antiparallel nullifying each other; 3) ferrimagnetism, if the moments are antiparallel, without nullifying each other. Under the effects of an external magnetic field, materials made of ferromagnetic minerals will acquire an induced magnetization indicated with M_i that will have the same direction of the applied field **H**.

Whenever the external magnetic field will removed, ferromagnetic materials retain a permanent magnetization which is called *remanent magnetization* that we will denote with M_r. Geological history events and chemical composition determine the characteristic of the remanent magnetization.

The total magnetization M is the vector sum of the induced and remanent magnetizations, given by:

$$M = M_i + M_r \tag{1.7}$$

The *Koenigsberger ratio Q* is indicative of ratio of the remanent magnetization M_r to the induced magnetization M_i and is expressed as:

$$Q = \frac{M_r}{M_i} \tag{1.8}$$

A value of $Q > 1$ indicates that the M_r dominates, and the magnetic anomaly observed in the survey primarily reflects the rock's past magnetic history. Conversely, $Q < 1$ means that M_i dominates, implying the anomaly mainly reflects the Earth's current magnetic field.

1.3 Magnetic Gradiometry

There are different approaches to the acquisition of magnetic data in terms of magnetometer types and number of sensors (e.g., in gradiometer arrangements). Moreover, the introduction of drones allows the deployment of new magnetic sensors increasingly light and small but with high sensitivity and sampling frequency. Therefore, a large number of both vector and scalar magnetometers are now available on the market for UAV surveys, from the classical fluxgate magnetometers to the optically pumped alkali vapor-magnetometer and SQUID systems, all useful for magnetic exploration.

Beyond the choice of the magnetometer type, very relevant could be the practice to use two (or more) sensors during a magnetic survey, especially for mapping shallow magnetic targets like archaeological remains and the detection of ferrous objects such as land mines and unexploded ordnance. With this approach, two measurements of the magnetic field are acquired at the same time through a pair of magnetic sensors spaced at a certain distance, called ‘baseline’. The difference between the two measurements obtained from the sensors divided by their distance allows the computation of the magnetic gradients (e.g., Slack et al., 1967). The magnetic gradients computed in this way, are almost insensitive to the regional fields and totally insensitive to the temporal variations of magnetic fields. Thus, thanks to a gradiometer arrangement the practice to use a base station during the magnetic surveys can be avoided. When two magnetic sensors are placed in the same horizontal plane a horizontal gradient can be measured. Often the two sensors are arranged along a vertical direction, allowing the computation of an approximate vertical gradient of the magnetic field component being measured. Other advantages that made the use of the magnetic gradient are the higher sensitivity to the shallow sources than the magnetic field, since the gradient fields decay faster, and the improved resolution (the ability to distinguish the anomalies coming from nearby sources) respect to magnetic field datasets.

Usually, the choice of the baseline length for hand-held magnetometers ranges between a minimum of 0.25 m to a maximum of 1 m. It is important to maintain a baseline smaller than the distance between the sensor closer to the ground and the source depth. In the case of deep targets, or high survey altitudes, the distance between the sensors should be increased.

Other strategies to compute the vertical gradient include the use of single sensor data and the well-known filter in the wavenumber domain, deriving from the potential theory (e.g. Blakely, 1996). A second common practice using the UAVs is to obtain a vertical gradient by two sets of co-located measurements at different elevations by repeated flights (e.g., Schmidt et al., 2020). Despite in some cases these approaches can give a good result, the computed gradients may still contain the effects of diurnal variations not well compensated or of positioning errors (when using two datasets at different altitudes).

Chapter 2 – A review of magnetometer types and UAVs

In this chapter, we present a review on all the elements required for UAV-borne aeromagnetic surveying. We will discuss magnetometers that are available and suitable for drone surveys, as well as the most used platforms. We will also describe the main solutions found to improve flight systems and how the main key issues were resolved to make the use of drones a real advantage acquisition possibility. New concepts, terminologies, and uses that are very close to drone practice are introduced, and different ways to merge the potentials of UAVs with the exigencies needed by the magnetic method are presented. The aim of a UAV magnetic system is not to replace traditional acquisition strategies, but to provide a complementary strategy for the acquisition of magnetic data of good quality. In fact, we will see that in cases of areas with difficult or impossible ground access, the use of drones is not an alternative, but will be indispensable.

Moreover, this section will showcase flight strategies and configurations developed by other studies depending on the targets. This could help to understand that there isn't only one solution in this research field but several valid attempts or approaches. Drone geophysics is a field in net expansion and continually updated thanks to the introduction of new magnetometers, drones, and secondary systems that improve acquisition strategies.

2.1 History, classification, and developments of UAV Platforms

UAVs are popularly called by several synonymous terms such as un-manned aircraft systems (UASs), drones, remotely piloted aircrafts, and aerial robots. The term “UAS”, however, refers to an entire system consisting of a UAV as the platform, the payloads and the ground controlling segment.

The invention of UAVs and the advances in this technology were largely driven by military requirements and progressive means of warfare during World War I. Drones have evolved in different configurations in order to develop different flight characteristics that could be exploited for various uses.

In 1933, the first mass-produced, unmanned aircraft was proposed by the Royal Navy and Royal Air Force with the name of ‘De Havilland, DH-82B Queen Bee’ (Taylor, 1989). Several developments between the years of the main World Wars allowed the spread of these technologies through civilian populations for different purpose like the research one. Important progresses in terms of materials allowed: 1) the use of LiPo batteries which implement the flight power capability and fundamental for the deployment of new miniaturized platforms; 2) replace kerosene engines with brushless electric motors; 3) to introduce carbon fiber rather than wooden frame. However, only the diffusion of the Global Navigation Satellite System (GNSS) provided the key for the modern UAVs with the implementation of software for the planning of automated navigation path.

Nowadays, drone technologies are commonly used for numerous applications of general interest like filmmaking, surveillance, disaster monitoring, cargo transport etc., or related to warfare and terrorism scopes. Obviously, UAVs are increasingly used in the geo-science research field. Although the most common geoscientific applications of drones are associated with acquiring aerial images and processing them using photogrammetric methods to make maps, the miniaturization of geophysical sensors like magnetic, electromagnetic, infrared, radar, natural gamma ray sensors etc., has recently opened new opportunities to install them on- board drones. Modern UAVs have longer endurance than their predecessors and therefore heavier payload, like geophysical sensors, can be hung under drone.

UAVs can be classified into different categories based on their design specifications. The main parameters used for classification are size, max take-off weight, operating altitude, speed, endurance, range, and weight, which are always declared by the manufacturers. Zheng et al. (2021) list several types of UAVs available on the market for magnetic exploration. The choice between fixed-wing, helicopter, airship, and multirotor should be made based on the tasks to be resolved, but most studies opt for multirotor systems. A list of pros and cons for each platform could help make a better choice. Fixed-wing UAVs would be the best option for geophysical exploration missions of large areas (over 150–200 km^2). The gasoline or electrical engines allow for high speed, long endurance, and large payload capability. However, these drones require runways or special devices for take-off and landing operations. Unmanned Helicopters can maintain the same velocity or less than fixed-wing UAVs, but with easier take-off and landing operations, making this solution suitable for hazardous ground conditions. This is an advantage over fixed-wing UAVs. However, the short flight time of about 1 hour and the high cost needed limit the use of these platforms for magnetic acquisition over large areas. Unmanned airships are the least used, as they are influenced a lot by environmental conditions, and the few examples proposed did not make them a good survey approach (Zheng et al. 2021), despite being able to fly for a long time. They need hot air or helium gas and, for this reason, are relatively costly.

Except for flight endurance, multi-rotor UAVs try to overcome all the limitations just described. These technologies are easier to use and can automatically follow pre-programmed routes. They enable high-resolution surveys with lower velocity, if needed, over areas of difficult access and steep topography by following the terrain. Compared to other platforms, they are the most cost-effective. These are all key features that make them widely used for a large part of geoscientific applications. However, a potential disadvantage could be their limited payload capability, although miniaturized and lighter geophysical sensors are available.

In the following sections, we will discuss the most commonly used magnetometers for UAV magnetic surveys and how these platforms are developed and combined with magnetic sensors in several studies.

2.2 Magnetometers suitable for UAV applications

To understand how the magnetic surveys become a useful subsurface mapping method, we need to go back in the time. The first widespread of electronic magnetometer dates back to the Second World War, where fluxgate sensors were designed for submarine detection from overflying aircraft and the magnetometer measured only the scalar magnitude of the total geomagnetic field (Reeves, 2005). In the 1941, Vacquier (1941) proposed the first fluxgate magnetometer able to measure only one component of the magnetic field (Vacquier, 1941). This was improved two years later, when a 3-component fluxgate was developed (Vacquier, 1943). Always during the Second World War, the magnetic method started to be applied for geological targets (Campbell, 2003) thanks the United States Geological Survey (USGS).

The deployment of magnetic sensors technologies for new applications of geological interest called for the implementation of magnetometers more performing, especially in terms of number of readings per second (sampling rate). In the late 1950s, despite on-going refinement of the fluxgate instruments, these were replaced by the invention of proton precession magnetometer in routine survey operations.

A third family of instruments, known as optical pumping magnetometers, first came into airborne service in the early 1960s, without replacing proton precession magnetometers until the late 1980s (Reeves, 2005). This last generation of instruments remain the industry standard to this day. Also, the introduction of the super-conducting quantum interference device (SQUID) magnetometers, started in the early 2000s (Schmidt et al., 2004; Stolz et al., 2006) for mineral applications, have not shifted the acquisition strategy on these new sensors technologies.

The magnetometers listed above can be fitted not only for airborne surveys, but also for marine, and ground-based ones and are classified in two main categories:

1. *Vector magnetometers* represented by the fluxgate and SQUID sensors which measure the strength of any component of the Earth's field by orienting the sensor in the direction of the desired component.
2. *Scalar magnetometers (or total field magnetometers)* represented by proton precession magnetometers, Overhauser magnetometers (the same fundamental effect of

the proton precession magnetometer) and optically pumped magnetometers which, regardless of the direction, measure the magnitude of the magnetic field vector.

Today, both categories of magnetometers presented are suitable and used for magnetic prospections in different kind of applications. If the vector magnetometers, usually, suffer the high noise levels caused by sensor motion and vibration, scalar magnetometers, on the contrast, are insensitive to the vibration of the platform and orientation.

Recently, part of these instruments is updated and developed to be used with drones. Below, we describe the specifications of the main magnetometers used for UAV applications and how are combined with the platforms in several studies.

2.2.1 Fluxgate magnetometers

In fluxgate magnetometers, two cores of high susceptibility and permeability are wound by identical, but oppositely inductive coils. After the passage of an alternating electric current through the wire coils, the core will be magnetically saturated in opposite directions. If a static magnetic field is aligned in the direction of the cores, one of them will reinforce the magnetization and will be rapidly saturated respect to the second core which, due to the oppositely wound induction coil, will oppose saturation. In this way, the resulting coil voltages sum will be an alternating positive and negative voltage spikes proportional to the intensity of the magnetic field. Fluxgate magnetometers can measure the three-orthogonal axes of the magnetic field obtaining both its magnitude and direction.

These magnetometers are less precise than others, with a sensitivity of 0.1 nT at a 1 Hz sampling frequency and a frequency band between 0.1 kHz and 10 kHz (Hinze et al., 2013). However, some specifications like the small volume and weight, low cost, lack of dead zones, and high tolerance to the magnetic field gradients, made the fluxgate magnetometers largely deployed for UAV surveys.

In the 2013, the Mobile Geophysical Technologies (MGT) were the firsts to use a fixed-wing UAVs with a fluxgate magnetometer for geomagnetic survey, developing the “Fixed Wing Mag System”. The long flight endurance of a fixed-wing platform, combined with a fluxgate magnetometer, allowed to explore large area increasing safety and productivity (intended as kilometers of flight per hour) as done by Jackisch et al. (2020) for the exploration of mineral deposits.

These magnetometers were integrated also to other platforms like Unmanned Helicopters. Eck and Imbach (2011), Stoll et al. (2013) implemented a system for near surface geophysical measurements to map cars, vans, and other metal objects buried by landslides. Pei et al. (2017), Zhang et al. (2019), Xu et al. (2020), and Jiang et al. (2020) equipped, for different purposes, an Unmanned Helicopter with both a fluxgate and an optical pumped magnetometer, conducting high efficiency acquisitions, also in areas with complex conditions.

Some attempts to integrate fluxgate sensors on an Unmanned Airships were done. Petzke et al. (2013) conducted magnetic tests with a limited resolution due to some issues, mainly due to the flight path and altitude. While Wang et al. (2016) obtained a better result demonstrating that it could be a practical solution.

However, the most common applications of magnetometers, including fluxgate magnetometers, are those that are used in Multi Rotor UAVs. This is also the platform used for our studies. The great diffusion of this type of drones calls for a larger description of their applications. Stoll et al. (2013), Yoo Lee-Sun Yoo et al. (2021) and Le Maire et al. (2023) deployed a UAVs fluxgate system for Unexploded ordnance (UXO) mapping. For the same target, Poliachenko et al. (2023) used the recent Mag Drone R3, a two-sensor magnetometer produced by German SENSYS company and designed for UAV application. The same magnetometer but installed in a forward boom 2 m from the UAV, is present in the work of Lee et al. (2023). The upgrade version, the MagDrone R4, with five mounted sensors, was used by Stele et al. (2022) and, also in this case fixed to the drone landing gear. Other studies for the near-surface ferrous and man-made objects detection (i.e., pipelines, archaeological remains, etc.) like the ones of Macharet et al. (2016), Gavazzi et al. (2016), Gavazzi et al. (2019) and Lépinay et al. (2021) also provide good examples of different approaches in terms of flight system, choice of platform and sensor suspension. Among them, MGT developed several industry-specific solutions depending on the target. They propose the Single Mag System (with one sensor) ideal for archaeology and geophysical exploration and the Dual Mag System (with two sensors) better for UXO and pipelines. While Pisciotta et al. (2021) suspended a light-weight fluxgate sensor few meters below a very uncommon platform like the DJI Phantom 4 to develop a light flight solution. Le Maire et al. (2020) preferred to mount the magnetometer 0.42 m in front of the drone at the tip of a composite pipe avoiding the oscillation of a suspended way. Other common applications regard the mineral exploration like the studies of Jackisch et al. (2019), Qiao et al. et al. (2020) and Parvar (2016). In this last work, a fluxgate sensor was used also to characterize the magnetic signature of a UAVs, determining the better position to locate the magnetometer during the acquisitions. Similar research was conducted in a laboratory by Walter et al. (2021). Some geological surveys over geomagnetically abnormal area like gullies, canyons and lakes were conducted by Li et al. (2018). Luoma et al. (2020) implemented a vertical gradiometer solution suspending two fluxgate sensors, with a baseline of 1 m, a few meters below the drone.

2.2.2 Proton Precession Magnetometers

In Proton Precession magnetometers a sensor cylinder containing approximately 500 ml of a proton-rich liquid (water, kerosene, or other alcohol) is wrapped by a coil and is connected to a measuring or recording device. A magnetic field, 50 to 100 times stronger than the Earth's one, generated after the application of a current to the coil, causes the alignment of the protons in the same direction of the new magnetic field. When the current is removed, the polarized protons will then rapidly return to their original alignment by precessing. The precession frequency can be related to the external field (i.e., Earth's magnetic field) and this allows for the measurement of the Total Magnetic Intensity (TMI) to a precision of approximately ±0.1nT. However, a window of 1-3 seconds is required for the recording due to the time needed to turn the current on and off.

The Overhauser Effect is used in an enhanced variant of the latest generation of proton precession magnetometers, which allow for the continuous measurement of the total magnetic field, giving the sensor a faster sampling frequency (Hovde et al., 2013). This phenomenon is obtained adding a liquid that contains free, unpaired orbit electrons to the proton-rich fluid. Respect to the classic proton precession magnetometers, Overhauser are advantageous. They have polarization at lower power levels with decrease in power consumption of 75%, generate a signal approximately 100 times stronger than that of the electron-deficient fluid, reduce the noise levels, have higher sensitivities (0.1-0.01 nT) and sampling frequencies (up to 5 Hz).

Packard and Varian (1954) proposed the first proton precession magnetometer that, in few years, replaced the fluxgate instruments in the traditional surveys. Nowadays, proton precession magnetometers are still used for ground acquisitions for its low cost and robustness. However, the sampling frequency of only 5 Hz and high weight made these instruments not a good solution for UAVs applications respect to the large deployment on the market of new miniaturized fluxgate and optically pumped sensors.

Malehmir et al. (2017) tested the potential of rotary-wing UAV system combining it with an Overhauser magnetometer reassembled to be lifted by the drone for direct targeting of mineral deposits. Similarly, Li et al. (2018) implemented a flight configuration after the establishment of a mathematical model for the compensation of the magnetic interference of UAV rotors. Parshin et al. (2018) created a UAV-Overhauser configuration stable and able to flight in a wide range of environmental conditions (even a moderate snowfall), by also developing a software to program the flight path. Both laboratory and flight tests over iron pipes were conducted by Ge et al. (2019). Parshin et al. (2020) used a Proton Overhauser magnetometer combined with gamma-spectrometry and electromagnetic prospecting for mineral exploration.

All the listed studies preferred to suspend the magnetic sensors at a certain distance from the drones through ropes or semi-rigid mount.

In some cases, the Overhauser proton precession magnetometer is used as a base station, measuring diurnal variations during UAV-borne aeromagnetic surveys, as done by Walter et al. (2020).

2.2.3 Optically Pumped Alkali Vapour Magnetometers

In Optically Pumped Alkali Vapour Magnetometers (OPM), a glass cell contains evaporated alkali metal such as cesium, potassium, rubidium, or a noble gas. A specific wavelength of polarized radio frequency light energizes one of these vapors (Budker and Kimball, 2013) so that the atoms will have their electrons, that exist in its valence energy levels (1 and 2), “pumped” to a higher unstable energy level (3) (Hinze et al., 2013). These high valence electrons will decay back spontaneously to their original energy levels. Part of the electrons spontaneously decay to position (1) while the remainder goes in position (2) and the cycle repeats until they have all spontaneously decayed and accumulated in level (1). In this way, the energy level (1) become fully populated, but the second energy level (2) will be underpopulated. The energy difference between valence levels (1) and (2) is proportional to the external magnetic field being measured. This process is fast and, when it occurs, the specific radiofrequency is unable to be absorbed by the vapor cell and light intensity measured will be maximized. Then, a second depolarizing radiofrequency, called Larmor frequency, displaces the electrons from the level (1) to (2) and the optical pumping phenomena restart. This process is continuous and occurs at extremely high frequencies. As consequence, Optically Pumped Alkali Vapour Magnetometers measure at very high sampling rates.

A rubidium vapour magnetometer was used by Skillman and Bender, in the late 1950s, for aeromagnetic surveys, but they did not replace proton precession magnetometers before the 80s (Skillman and Bender, 1958). The main advantages of these sensors are the good resolution and gradient tolerance, the highest sampling frequency which range between 20-1000 Hz and a sensitivity 10-100 times more than the other sensors described. The latest CAE MAD system, called MAD-XR (Magnetic Anomaly Detection Extended Role), can reach a sampling rate of 1525 Hz. These specifications made the Optically Pumped Alkali Vapour Magnetometers the most suitable for magnetic surveys and below we list the main works that used them. The only two limitations of these instruments are related to dead zones and heading errors. Since we used a type of these magnetometers for our investigations, we will describe and discuss how we resolved these issues in the next Chapters.

Optically Pumped Alkali Vapour Magnetometers were combined in several studies with all the UAVs platforms already presented. Anderson and Pita (2005) launched the GeoRanger™ for petroleum and mining exploration, with an endurance over than 10 hours and a productivity of 75 km per hour. Gee et al. (2008) tried the first deployment of a fixed-wing UAVs from a marine research vessel for the measurements of magnetic field fluctuations in a remote area of the southwestern Pacific Ocean. In the same year, Barnard (2008) presented a platform for oil, gas, and mineral exploration. Glen et al. (2013) aimed to identify buried and intra-basin structures, planned a magnetic survey using a cesium magnetometer. Li et al. (2014) equipped a middle-size fixed-wing with a CS-VL cesium vapour sensor over a mine area. Stratus Aeronautics (Wood et al., 2016) developed the Venturer, a drone tested the first time in southern Alberta, Canada along 13 km of preprogrammed survey lines, with calibration maneuvers, and for 45 minutes' worth of data collection. Sterligov and Cherkasov (2016) built a nonmagnetic unmanned aerial platform (NUAP) for high-quality magnetic surveys with internal combustion engine and the sensors mounted on the wings. In 2017, the MONARCH fixed-wing was launched (GEM Systems 2017) to provide a gradiometer configuration using two potassium sensors. The CH-4UAV was an improved platform proposed by Ju et al. (2020) which provided safely flights.

Among the studies that used Unmanned Helicopters, Versteeg et al. (2007) was the first that analyzed the signature associated to platforms components introducing several UAVs for the acquisition. McKay et al. (2011), aimed to the subsurface ordnance detection, tested a Geometrics G823 A magnetometer integrated with two different platforms: the Maxi-Jocker and Mongose UAVs. Koyama et al. (2011), and Hashimoto et al. (2014) used the same UAV magnetic system for volcano aeromagnetic survey, suspending a cesium OPM 4.5 m below a RMAX-G1 platform. Finally, the contributions of Pei et al. (2017), Zhang et al. (2019), Xu et al. (2020), and Jiang et al. (2020) are already cited above since they used both the fluxgate and OPM sensors.

Also, the study by Wang et al. (2016) mentions the deployment of an airship with an OPM for mineral exploration. The study used both a fluxgate and a helium magnetometer and achieved discrete success. Kim et al., 2020 confirmed the applicability of these platforms by acquiring a magnetic dataset over a known mineralogic area of interest. The result appeared similar to that obtained from a manned airplane survey.

For the purposes of this work, a detailed overview of the OPM used for magnetic exploration, how it is mounted on a multi-rotor, and the state of the art in the processing step, allows for a better appreciation of the scientific contribution and the perspective of this thesis.

Veloski et al. (2018) used the same magnetometer employed for our research which is the Micro-Fabricated Atomic Magnetometer (MFAM) built by Geometrics, Inc. It was housed in a custom bird with an arrow shape, an early prototype then implemented by the Geometrics, Inc., suspended few meters below a DJI Matrice M600 Pro hexacopter and towed for the mapping of wells. Parvar et al. (2016) suspended a GEM Systems GSMP-35A magnetometer 3 m below a multi-rotor to detect the serpentinization of a chromite host rock. Mineral exploration for zinc deposit regards also the work of Cunningham et al. (2018) but, differently from Parvar et al. (2016), a Geometrics G-823A cesium vapour magnetometer was front-mounted on a non-magnetically susceptible boom to minimize the magnetic interference from the UAV frame on the sensor data and in the same horizontal plane to facilitate take-off and landing operations. Walter et al. (2019) used a spectral analysis to study the signal contribution due to the swinging of a GEM Systems GSMP-35U potassium vapour magnetometer suspended outside the zone of electromagnetic interference created by the UAV (3 m from the platform) through a semi-rigidly mount which allows the magnetometer payload to freely move in the pitch and roll axes, while rigidly fixing the yaw. With the same flight system, Walter et al. (2020) conducted a three-dimensional unmanned aerial vehicle aeromagnetic survey within the Shebandowan Greenstone Belt, Ontario, Canada, at approximate elevations of 35, 45 and 70 m above ground level (AGL) and then compared the result to a regional heliborne aeromagnetic survey flown at an elevation of approximately 85 m above the terrain. Nikulin and de Smet (2019) used a MFAM in the "Developted kit" version suspended few meters below a DJI Matrice 600 hexacopter for the identification of abandoned and unmarked oil and gas wells. One year later, to overcome the low battery capabilities problem, de Smet and Nikulin (2020) replaced the older platform with a UMT Cicada gas-electric hybrid hexacopter platform. The same magnetometer, but in the Geometrics Inc. MagArrow version, was used by Schmidt et al. (2021) for archaeological purpose and is attached to the UAV via 3m-long ropes. Mu et al. (2020) was one of the first that proposed a configuration with two sensors (CAS-L3 Cs magnetometer) integrated directly to the platform with a baseline of 0.30 m for near magnetic targets like UXO detection. For this reason, a specific way to eliminate the interference field generated by the drone through an improved Euler deconvolution was proposed. Cunningham et al. (2021) launched the SkyLance 6200, an updated version of the original platform described in Cunningham et al. (2018) maintaining the same mount system and investigation target. Walter et al. (2021), after the measurements of the electromagnetic interference generated by two unique multi-rotor UAVs in a controlled lab setting, used a MagArrow at 3 m from the platform engines, showing that an adequate sensors placement and pre-flight evaluation of the platform-sensor interactions provide useful mitigation strategies for the UAV magnetic interference. Dossing et al. (2021) developed a special custom bird that allows high-speed surveys, easily to transport in the field without a car and, deployable in most terrain, using QuSpin Total-Field Magnetometer (QTFM) suspended 4 m below a DJI M210 UAV. An upgraded flight system was launched in Kolster et al., 2022, where three QuSpin QTFM, spaced of 1 m, were used for UXOs detection. Respect to the common choice to maintain a standard distance of 3 m to separate the magnetic sensor from the engines, Phelps et al. (2022) opts for a 5 m sling to maximize the reduction in UAV noise. On the contrary, Cao et al. (2022) equipped a DJI M300 RTK with a horizontal carbon fiber tube and one or two atomic optical pump sensors mounted to its tip.

2.2.4 SQUID Magnetometers

SQUID is the acronym of "Superconducting Quantum Interference Device" and its deployment come after the studies of Josephson (1962) and Josephson (1974). Within the magnetometer, a loop of superconducting metal is immersed in liquid helium or nitrogen. This sensing element has one or more weak links in it (known as a Josephson junction). A current in the loop will be generated to the change in magnetic field. The resistance of the Josephson junction interrupts the current in the loop and these gaps of the current in this superconducting loop are sensitive to the magnetic flux perpendicular to it. Magnetic field change is provided by a nearby coil that monitors the circulating current and its break in the loop.

SQUID magnetometers measure only one component of the magnetic field but the use of three superconducting loops, if positioned precisely orthogonally to each other, can provide the total magnetic field though the measure of its 3 vector components (Budker and Kimball, 2013).

Respect to the most common and used magnetometers, these devices have the highest sensitivity that is approximately 1 x 10^{-5} nT with sampling frequency of up to 50 kHz. The SQUIDs peculiarities make it useful for very low magnetic field variations. Some geophysical applications could include the study of rock samples for paleomagnetism or for the detection of defects in buried pipes and steel structures. However, some factors limit their deployment like the extreme precision in the superconducting loops positioning and low cryogenic temperatures needed to supercool the loops, in addition to other logistical considerations related to the device components and costs. Therefore, many challenges must be solved before to implement a UAV SQUID system, but future research will try to find a large number of solutions to integrate these instruments with drones.

Chapter 3 – Development of a UAV-borne Aeromagnetic System

This chapter aims to provide a comprehensive overview of the materials, design solutions, and integration strategies employed in the development of our UAV magnetic system. We present the magnetometer used in all the geophysical investigations, how it was arranged and integrated with the various types of drones. This chapter provides a comprehensive introduction to the primary objective of our research: the development of a versatile UAV magnetic system that can be adjusted according to the target of interest. While the magnetic sensors remain the same across all the geological, archaeological, and engineering applications, the housing for the magnetometer - referred to as the ‘custom-bird’ - and its attachment method to the drone have been modified.

3.1 Micro-Fabricated Atomic Magnetometer (MFAM)

MFAM is the acronym that used to indicate the Micro-Fabricated Atomic Magnetometer, produced by Geometrics. It is a miniaturized scalar atomic magnetometer with two laser pumped cesium sensors. Thanks to its light weight of less than 1 kg, a small size of 15.39 cm^3 for each sensor, and a high sensitivity of 1pT/√Hz, the MFAM is ideal for UAV integration. However, the main peculiarity is the high sampling rate of 1000 Hz that allows a direct measurement of the high frequency magnetic noise associated to the mobile platforms and its engines. These disturbances, if not sampled, could go in aliasing, and compromise the data quality. A second advantage is the possibility to plan high spatial resolution surveys at fast speeds. The MFAM sensor has one polar dead zone unlike the other traditional cesium magnetometers which have a polar and an equatorial dead zone (however, this is an advantage of the MFAM). If the sensor’s optical axis is lined up within +/- 35 degrees of the Earth’s magnetic vector, little or no signal is generated. It means that the local magnetic field inclination angle (vector) is intersecting the sensor’s polar dead zone. Outside of the polar dead zone, the magnitude of the Earth’s field will be measured pretty much independent of the orientation. To get maximum signal, the Earth’s magnetic vector should be at right angles to the optical axis.

The MFAM is typically included in the MagArrow, an aerodynamic and lightweight shell produced and sold by Geometrics. However, this system does not allow for the modification of sensor positions. For our investigations, we used the “Development Kit” version of the MFAM. This version allows the two sensors of the module to be used either independently or as an intrinsic gradiometer.

Therefore, several custom birds to house the magnetometer were implemented depending on the target. First tests were conducted using a plastic case, as shown in Figure 3.1 a. In this configuration, the MFAM module and the Development board (protected by an aluminum enclosure) were contained in a rigid box (Figure 3.1 b) with an Adafruit GPS Antenna and an external power supply. The flex cables were passed through a HDPE (high-density polyethylene) tube and connected the sensing module to the sensors which are also housed in a smaller plastic box. Figure 3.1 c show how the sensors were held thanks to an expanded polyethylene structure and juxtaposed with a distance between their centers of about 2.5 cm. However, this configuration was considered too heavy, and a lot of aerodynamic problems were found during the first flight tests.

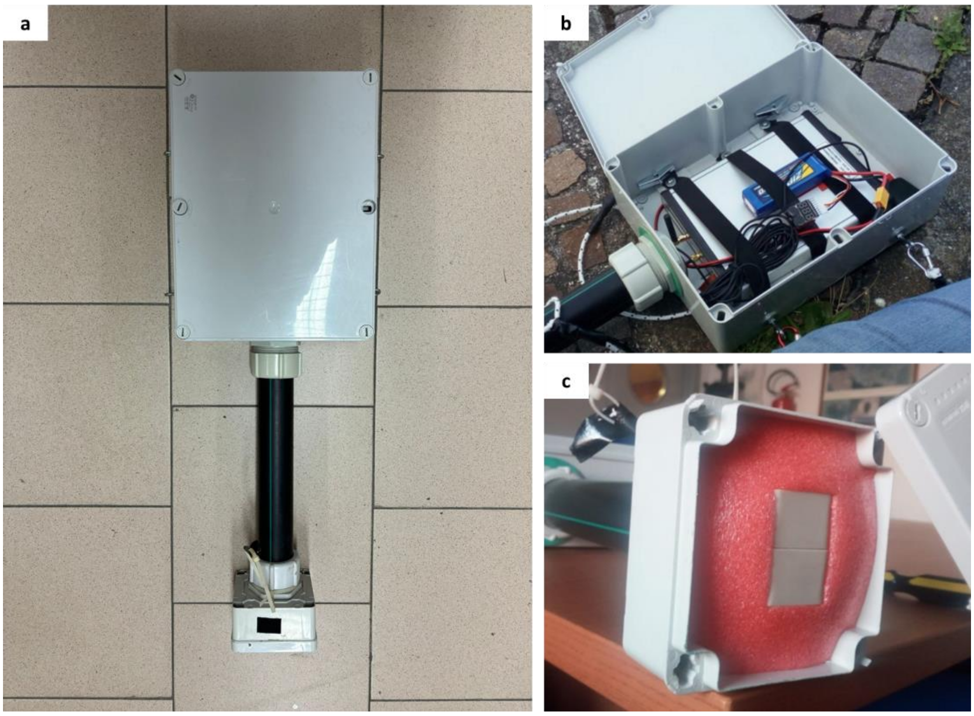

Figure 3.1. First custom bird implemented to house the MFAM. **a)** Photo of the entire plastic case; **b)** Location of the Adafruit GPS, external battery and aluminum enclosure which contains MFAM Sensing Module with the Development board; **c)** Positioning of the two sensors.

To overcome these limits, a second custom bird was designed. The MFAM was placed on a thin and rigid base made of a Nomex honeycomb sandwich panel with a cover in polystyrene. This configuration is a nonmagnetic, aerodynamic, and light solution considering the total payload weight less than 2.0 kg. All the cables which connect the GPS antenna and the battery with the Development board are placed forward the magnetometer, in the tip of the bird (Figure 3.2 a). Thanks to the Development kit version, we have the possibility to freely change the sensors positioning. Therefore, we implemented a vertical gradiometer by adding several polystyrene frames to distance the sensors of 0.25 m (Figure 3.2 a) or 1 m (Figure 3.2 a).

All the configurations of Figure 3.2 were used for our investigations, which will be presented in the following Chapters. We decided to opt for the vertical gradient set-up only for the archaeological prospections where we had to increase the resolution of shallow and weak sources.

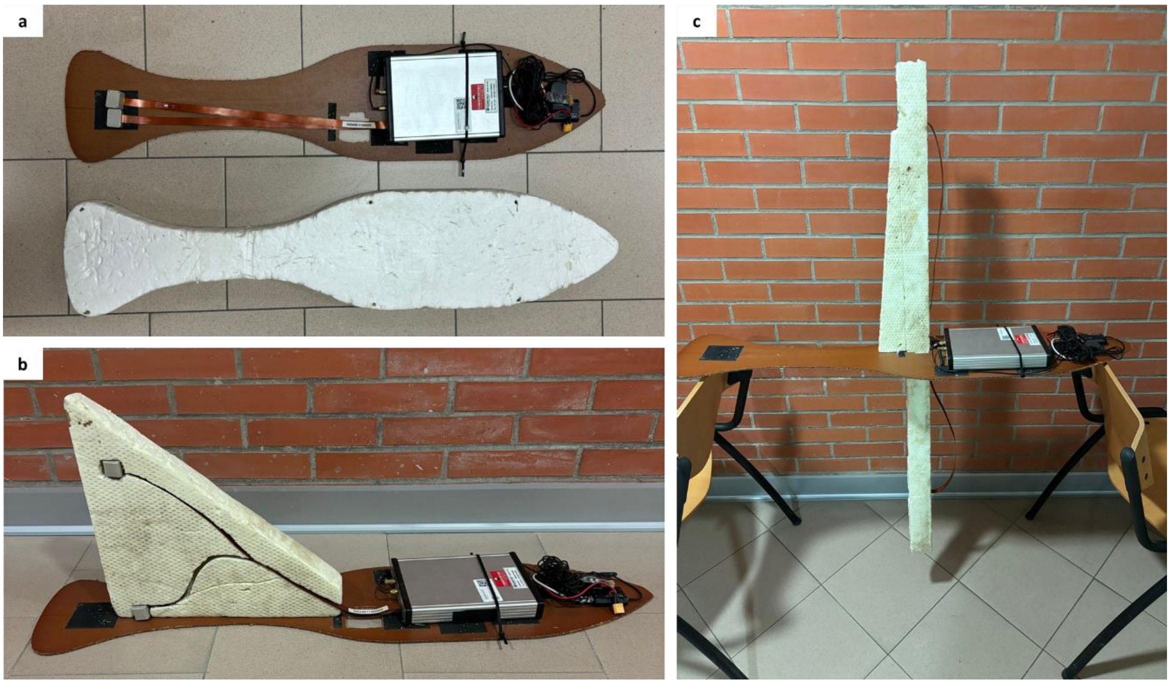

Figure 3.2. MFAM custom bird solutions. **a)** Configuration with sensors maintained on the same horizontal plane; **b)** Vertical gradient arrangement, with baseline of 0.25 m; **c)** Vertical gradient arrangement, with baseline of 1 m.

Chapter 3.2 and 3.3 have been omitted from the text as they are in submission phase.

Chapter 4 – UAV magnetic applications

This chapter presents the original contributions of our research from both a technical and data processing standpoint. Part of the work collected within the main body of this section is referenced in some individual publications and was foundational for the rapid deployment of UAV magnetic systems. Our study includes the main challenges discussed in the chapters above and outlines the practical solutions found through several applications of geological, engineering, and archaeological interest. The main goal of this research is to develop a versatile UAV-borne aeromagnetic system that can be used and adjusted depending on the target, as well as an editable data processing workflow. The case studies presented in this chapter demonstrate the applicability of UAV-borne aeromagnetic systems as a viable geophysical acquisition solution for a wide variety of targets.

The first study presented (Chapter 4.1) is extracted from the following publication:

Accomando, F.; Vitale, A.; Bonfante, A.; Buonanno, M.; Florio, G. Performance of Two Different Flight Configurations for Drone-Borne Magnetic Data. Sensors 2021, 21, 5736.

In this study, we tested two magnetic flight configurations favoring the stability of the system during flight or the minimization of mobile platform noise. First, we attached the magnetometer directly to the drone landing gear, and then we suspended the sensors 3 m below the platform. We analyzed the spectral contribution of the aerial data by comparing them with a ground dataset that represents our benchmark. The acquisition targets were buried metal pipes, of which we also estimated and compared the depths. The results obtained from the study demonstrate that careful processing gives high-quality data using both flight configurations. Therefore, a flight solution with the magnetometer fixed to the drone landing gear, very close to the platform engines, could be a practical flight solution, at least for high magnetic anomalies like the ones produced by metal objects.

The second study presented (Chapter 4.2) is extracted from the following publication:

Accomando, F., Bonfante, A., Buonanno, M., Natale, J., Vitale, S., & Florio, G. The drone-borne magnetic survey as the optimal strategy for high-resolution investigations in presence of extremely rough terrains: The case study of the Taverna San Felice quarry dike. Journal of Applied Geophysics, 2023, 217, 105186.

The study aimed to map the areal extension of a dike that emerges along the wall of an active limestone quarry. Considering the high susceptibility contrast expected from an igneous dike intruded in sedimentary rocks, we took advantage of the main conclusions of Accomando et al. (2021) by attaching the magnetometer directly to the drone landing gear. The extremely rugged terrain conditions made the use of the drone the only possibility to acquire a magnetic dataset in the area. The results allowed us to map the subvolcanic body outside the quarry area, identifying several vents fed by the dike. We then used forward modeling to estimate the source parameters in terms of magnetizations and depths.

The third study presented is a second geological application. We planned a UAV magnetic survey to characterize the fault system within the Pantano di San Gregorio Magno, in Southern Italy, mainly represented by the Irpinia Fault that caused the 1980 Ms 6.9 earthquake. The aim of this survey was to define the basement geometry or even the fault trace. The magnetic investigation was a complementary approach and part of a multidisciplinary high-resolution geophysical study of the area.

The following sub-sections are dedicated to the acquisition strategies implemented for archaeological purposes. Magnetic anomalies are sensitive not only to the physical properties of natural sources (i.e., soils and rocks) but also to man-made objects that show a susceptibility contrast with the surrounding, as in the case of archaeological targets. Usually, the magnetic anomalies generated by archaeological targets are weak, small and strongly interfering. Their detection requires high-resolution magnetic measurements collected close to the terrain and with a small survey line separation distance. The investigation area should be large to consider the resulting anomaly significant, especially in the case of regular and elongated shapes of remains from buried buildings or roads. A common survey choice, especially in archaeological applications, is the implementation of a magnetic gradiometer. The reasons for this practice are better explained in

Section 1.4. Nowadays, the use of an accurate DEM or of a laser/radar altimeter allows a UAV magnetic survey to follow the terrain, potentially giving a similar resolution as traditional ground surveys. We will present three archaeological studies:

- In the archaeological site of Metaponto, we implemented the first attempt of vertical gradiometer configuration with the MFAM, conducting both a ground and a UAV survey.
- The case of Norwegian Iron Age settlements, in a combined work with SINTEF (Stiftelsen for industriell og teknisk forskning, “The Foundation for Industrial and Technical Research”).
- Finally, we show some tests on the vertical gradient arrangements, comparing different sensor distances.

4.1 Performance of two different flight configurations for Drone-Borne magnetic data

4.1.1 Introduction

A large number of studies deal one of the main problems related to magnetic data acquired from a plane, helicopter, or drone which is the best way to compensate the interferences produced by the mobile platform through the use of flight practice combined with filtering techniques. The traditional solutions deployed for high-altitude aeromagnetic surveys based on the attitude information are not generally practicable for UAV magnetic system. Tuck et al. (2019) propose flight test in an area of nearly constant external magnetic field with condition achievable only at a high altitude. The solution most used for UAV magnetic survey is to suspend the magnetometer away from the platform (Mu et al., 2020). A good magnetometer–UAV distance to avoid the electromagnetic noise is estimated between 3 m and 5 m depending on the type of drone and payload. However, the solution to suspend the magnetometer up to the distance of 3 m from the platform with ropes can create the inevitable system oscillations which could compromise both the stability of the flight and the data quality.

The focus of this work was to compare two different ways to attach the magnetometer to the drone using different distances between the UAV and the magnetometer sensors. The need to implement a safe and stable system with the magnetometer fixed to the drone landing gear is compared with a solution where the sensors, far from the platform, are outside the UAV interference area. To evaluate the quality of the magnetic response, both flight datasets were compared to a ground one acquired in the same area. First, we characterized and assessed the noise of drone-borne data using a spectral analysis, then we compared the sources depth estimations.

4.1.2 Measurements and Survey design

The drone-borne magnetic and the ground magnetic surveys were conducted on 1 October 2020 at Verteglia Plain, a small tectonic-karst basin, located in the Picentini Mts. (southern Apennines, Italy). The Terminio-Tuoro massif is characterized by a carbonate succession in platform facies, with Jurassic and Cretaceous limestones covered by quaternary deposits, represented by discordant accumulations of pyroclastic products of Somma–Vesuvius activity and lacustrine deposits. The surveys were performed during the “SEG Geophysical Field Camp in Southern Italy 2020” (for more information, see https://seg.org/fieldcamps accessed on 22 August 2021.) activities, organized by the SEG Student Chapter of the University of Naples Federico II and partially funded by the SEG Foundation. The investigated area is rather flat and devoid of dense vegetation.

UAV and ground surveys were conducted over an area where the presence of buried steel pipes was ascertained but the precise location, shape, and number of sources were unknown.

For both aerial and ground surveys, we used a Geometrics Micro-Fabricated Atomic Magnetometer (MFAM) in the “Development kit” version. The magnetometer specifications are well presented in the Chapter 3. The very high sampling rate of this magnetometer (1000 Hz) allows obtaining a unaliased measurement of 50 Hz fields as well as the correct identification of the high-frequency magnetic noise caused by the rotary aircraft used. In configuration choose for this survey, the MFAM was housed in a light, aerodynamic, and nonmagnetic custom bird made of polystyrene with a thin and rigid base made of a Nomex honeycomb sandwich panel (Figure 4.1.1 a). The platform used for the aerial survey was an electric-powered DJI Matrice 600 pro hexacopter. The total payload weight was about 2.0 kg. During the first flight configuration, the magnetometer was fixed to the UAV landing sled, with the MFAM sensors at a distance from the rotors of only 0.5 m (Figure 4.1.1b). During the second flight configuration, the MFAM was suspended 3 m below the hexacopter rotors by using thin nylon ropes (Figure 4.1.1c). For simplicity, from now on the flight configurations and the datasets relative to a magnetometer–UAV distance of 0.5 m and 3 m will be referred to as F0.5 and F3.0, respectively. To maximize the magnetic data quality and avoid falling in the sensor’s dead zone, in each survey the lines were oriented along a direction approximately North–South.

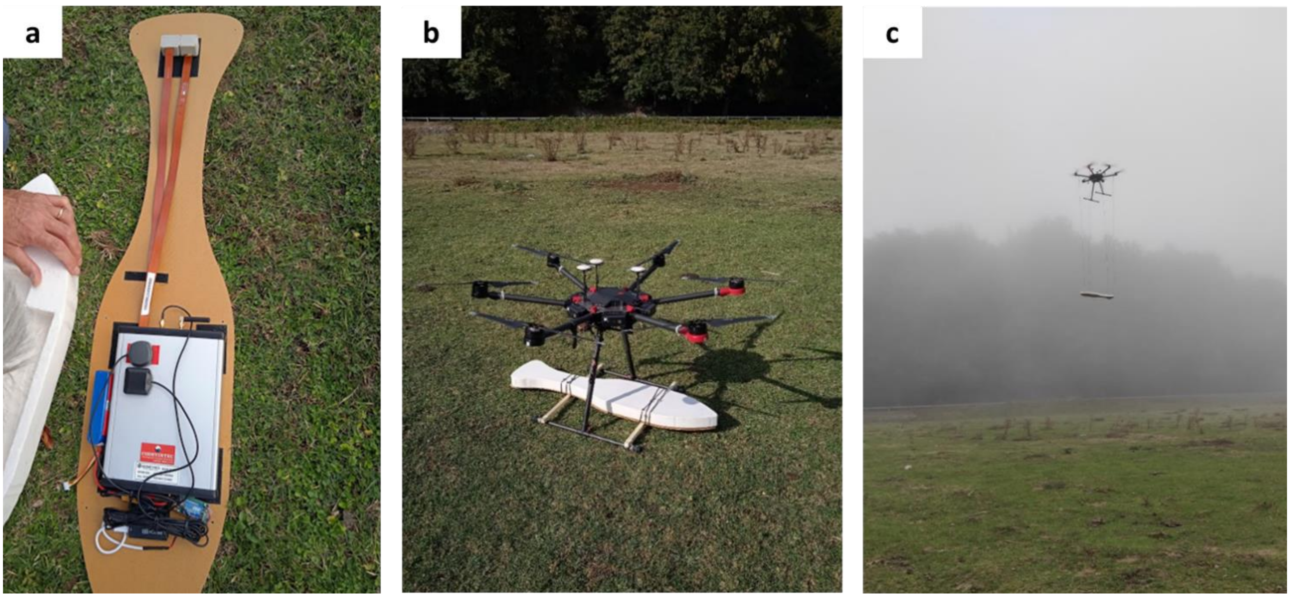

Figure 4.1.1 (a) Arrangement of the GEOMETRICS MFAM "Development kit" magnetometer inside the bird; **(b)** first flight configuration (F0.5), with the magnetometer fixed to the UAV landing sled, 0.5 below the platform; **(c)** second flight configuration (F3.0), with the magnetometer suspended 3 m below the UAV.

The two pre-programmed flights were conducted on the same 105 m x 24 m area, at a speed of 2 m/s, and at different elevations such as the magnetometer sensors being at about 8 mabove ground level (AGL) in both flight configurations. Seven parallel survey lines, oriented in the North–South direction, were flown with an approximated 4 m line's separation. With MFAM operating at 1000 Hz and a flight speed of about 2 m/s, the sampling step of the magnetic data along the survey lines was as small as about 2 mm. The geomagnetic field in this area had a declination of 4° and an inclination of 57°.

The ground survey was conducted in a 90 m 38 m area, partially overlapping with that covered by UAV surveys, along bidirectional lines spaced 2 m apart, oriented in a North–Northeast to South–Southwest direction (Figure 4.1.2). To minimize heading errors, the magnetometer was not rotated when starting a new line. The ground magnetic data were positioned with respect to a local reference system by introducing markers in the data stream at pre-defined positions along the profile (in our case, at the ends and at the center of each survey line).

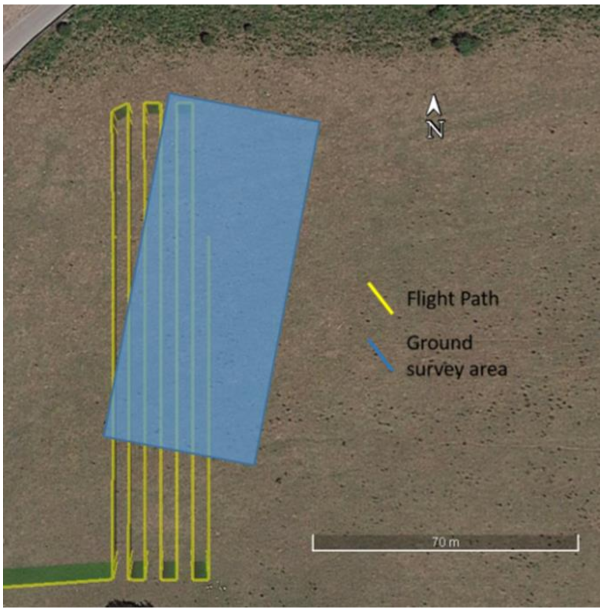

Figure 4.1.2. Planning of UAV and ground surveys.

The magnetic ground survey lasted approximately 2 h and was conducted by the participants to the SEG Geophysical Field Camp under the supervision of expert tutors; each of the two flights lasted approximately 10 min. During the time interval in which the drone-borne ground magnetic surveys were completed, the total magnetic field was monitored at a point in the same survey area. The total field variations were negligible, so that no temporal correction was applied to the three datasets.

4.1.3 Results

UAV Surveys Magnetic Data

The analysis of the data obtained by the MFAM magnetometer during flights included at its very first step the removal of all the values relative to the UAV turns between the survey lines and the subtraction of the IGRF. The resulting unfiltered total-field anomaly data of the two flights collected along the seven profiles are displayed in Figure 4.1.3. Here the data are shown sequentially, without using the position information. The difference between the data recorded in the two flight configurations is evident. Although the two datasets look very similar in the anomaly shapes and amplitudes, when the magnetometer was very near to the drone (F0.5; Figure 4.1.3a) a high-frequency and high-amplitude noise (maximum amplitude of about 10 nT) was present during all the flight duration.

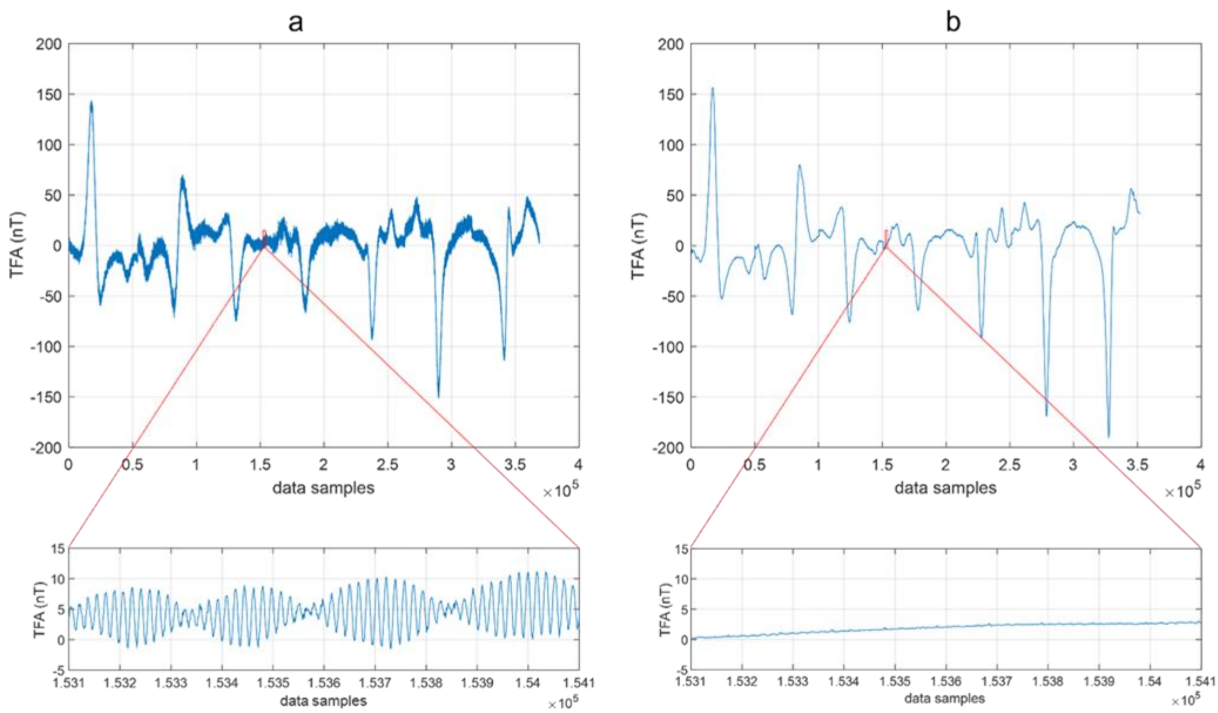

Figure 4.1.3. Total-field anomaly acquired using different flight configurations. (**a**) Data acquired with a magnetometer–UAV distance of 0.5 m (F0.5 dataset); (**b**) data acquired with a magnetometer–UAV distance of 3 m (F3.0 dataset). “TFA” stands for “total-field anomaly.”

Thus, we can reasonably associate this disturbance to the magnetic and electromagnetic interference fields generated by the UAV platform. As Walter et al. (2021) showed, the UAV presents sources of magnetic and electromagnetic interference signals, with the last proportional to the rotation frequency of the electromagnetic motor. However, at an offset distance of 3 m, as in the

F3.0 configuration, the magnetic field produced by a DJI M600 hexacopter appears sufficiently attenuated (Figure 4.1.3b), which is consistent with the results of the already mentioned previous studies about the optimal magnetometer–UAV distance.

A spectral analysis of data acquired during both flight configurations can provide insights into the differences in the signal components in the two cases. The analysis of aeromagnetic data with wavelets is often an advantageous approach, due to the ability to explore the variations of the frequency content of the data through time or space. The discrete wavelet transform can be used to perform a localized filtering of the data, while in our case we used the continuous wavelet transform (CWT) to obtain a scalogram of the datasets in the time domain. This analysis helped us to identify the noise and signal components of the data. We used a “morse” wavelet, and we present the modulus of the complex set of CWT coefficients for the drone-borne datasets in Figure 4.1.4.

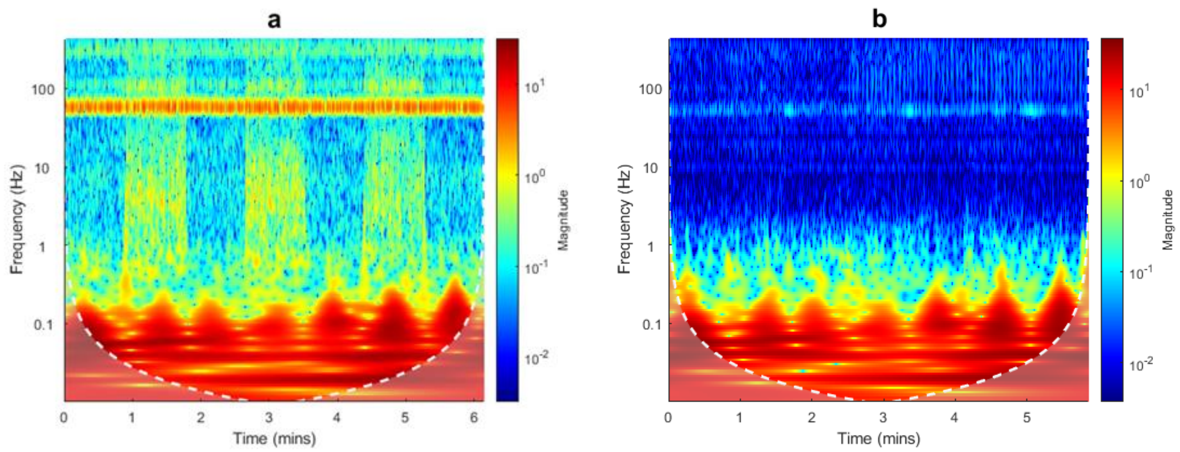

Figure 4.1.4. Spectral analysis of UAV data. **(a)** Scalogram of F0.5 dataset; **(b)** scalogram of F3.0 dataset. Edge effects in the computation of the spectra may be significant in the dimmed area below the dashed white line.

First, we noticed that the scalogram relative to the F0.5 configuration (Figure 4.1.4a) highlights, between 0.2 and 100 Hz, alternating amplitudes related to different survey lines. These different amplitudes can be associated with a strong heading error: the data acquired from South to North have a lower average value and noise amplitude than those acquired from North to South. The heading error is an intrinsic instrumental characteristic due to the orientation of the sensors. Its amplitude depends on the fact that the sensors are placed in the volume with the strong magnetic effect of the UAV. In fact, the UAV has its own magnetic effect, and the position of the magnetometer sensors with respect to this UAV-related magnetic effect may change with the flight direction, altering the average value and the noise amplitude of the recorded data from line to line. During the first flight, the sensors were very near to the UAV so that the heading error results were strongly amplified with respect to the F3.0 configuration, when the sensors were at 3 m from the UAV rotors.

For frequencies above 0.5 Hz, the F0.5 signal always has a higher magnitude than that of F3.0, with an evident peak around 50 Hz. This feature, highlighted by the scalogram analysis, can be interpreted by the presence of a significant platform-induced magnetic and electromagnetic interference sensed by the magnetometer. Walter et al. (2021) shows that most of the electromagnetic interference caused by the drone engines has a main power spectral density peak at about 50 Hz. The data acquired with the F3.0 configuration was clearly less affected by magnetic interference from the UAV. However, the scalogram shows again a peak in the power spectral density around 50 Hz and, with much lesser amplitude, at 10, 20, and 30 Hz. To compare easily the two datasets for each flight, we computed the sum of the scalogram magnitudes at each frequency (Figure 4.1.5). It resulted that the scalograms of the two datasets were very similar for frequencies lower than 0.5 Hz.

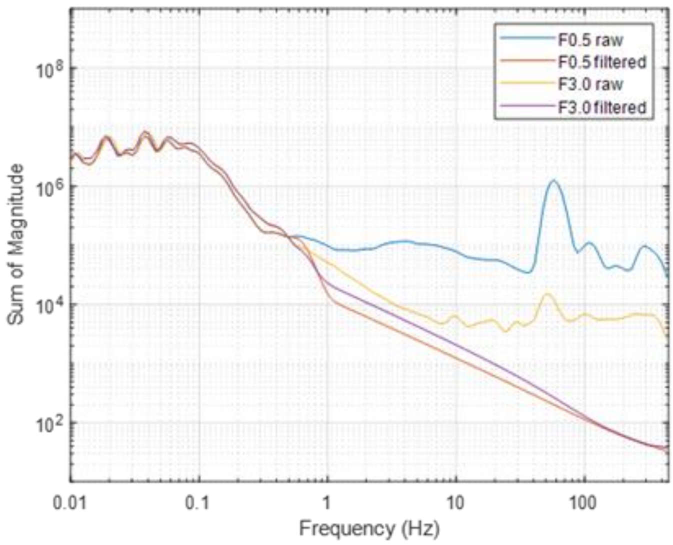

Figure 4.1.5. Sum of power of the scalograms for each frequency of both raw and filtered data flights.

To estimate, in the time-frequency scalograms (Figure 4.1.4), the frequency band associated to the target signal, we can evaluate the ratio of the UAV speed (2 m/s) and the anomaly horizontal extent (representing a half-wavelength of the signal) multiplied by two. The analysis of the data profiles shows an anomaly half-wavelength of 15–25 m, so that we can estimate a target signal frequency band between 0.06 and 0.04 Hz. In fact, we can see that these are the frequencies where most of the power of the scalograms is concentrated (Figure 4.1.4).

The above analysis guided us in the design of a time-domain Hanning-window low-pass filter with a cut-off frequency of 0.5 Hz, aimed at removing the noise and preserving the lowest frequency signals, associated with buried sources. This filter was applied to both the drone-borne datasets (Figure 4.1.5), as the overall characteristics of the scalogram are very similar in the two cases, differing mainly in the power of the frequencies higher than about 0.5 Hz. An example of application of the low-pass filter along two profiles of both UAV datasets is presented in Figure 4.1.6.

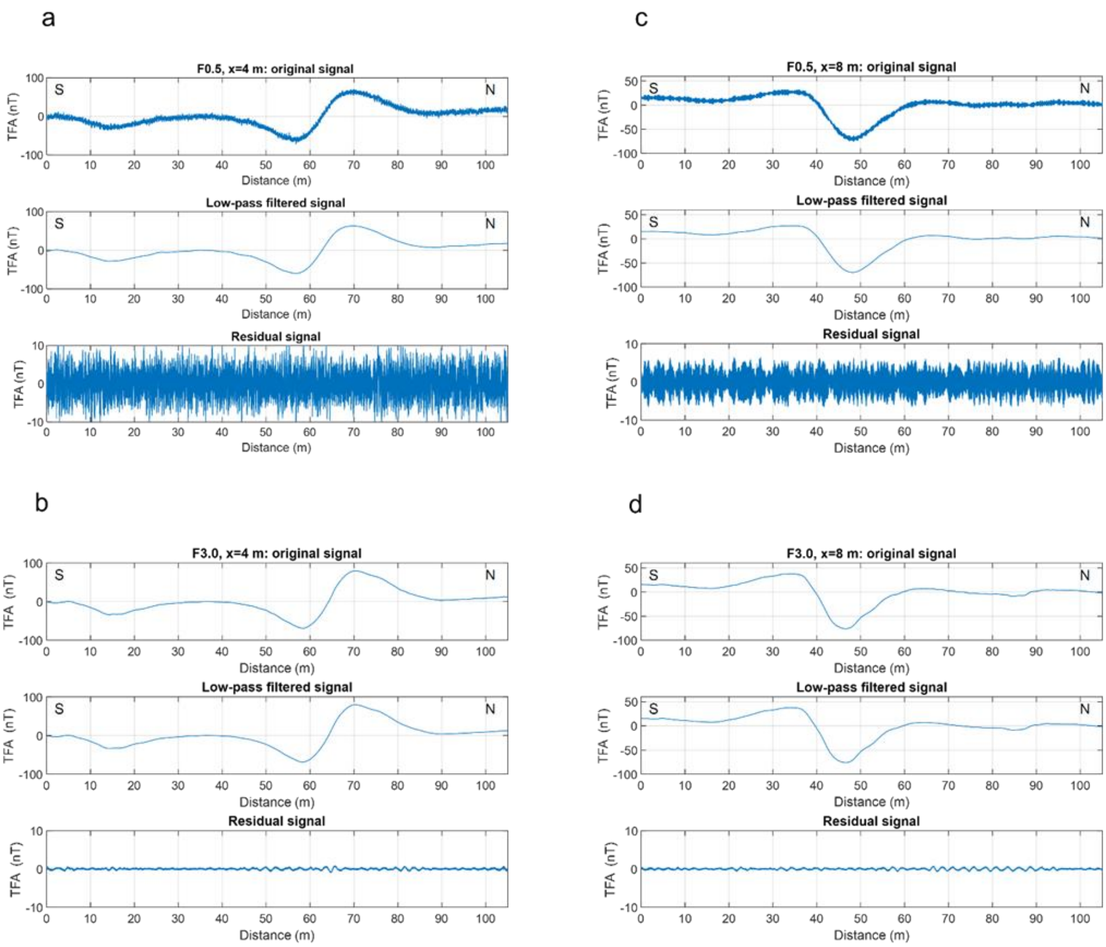

Figure 4.1.6. Application of a 0.5 Hz Hanning-window low-pass filter along two profiles for F0.5 and F3.0 datasets. The three plots in each panel show the raw data, the filtered data, and their difference (the residual signal). (**a**) Profile at x = 4 m; the magnetometer–UAV distance was 0.5 m; (**b**) profile at x = 4 m; the magnetometer–UAV distance was 3 m; (**c**) profile at x = 8 m; the magnetometer–UAV distance was 0.5 m; (**d**) profile at x = 8 m; the magnetometer–UAV distance was 3 m. The difference in amplitude between the residual signal in (**a**) and (**c**) demonstrates the heading error, as the two profiles were acquired while flying in opposite directions. "TFA" stands for "total-field anomaly."

A commonly used method to evaluate the high-frequency noise level in aeromagnetic data is the computation of the amplitude of the "fourth difference," a numerical approximation to the fourth derivative of measured data (Hood,P.J. et al. 1989, Teskey, D.J. et al., 1991). At the point where a central value ΔT_0 is measured, the fourth difference (FDIFF) is evaluated as:

$$FDIFF = -\frac{\Delta T_{-2} - 4\Delta T_{-1} + 6\Delta T_0 - 4\Delta T_{+1} + \Delta T_{+2}}{16} \quad \textbf{(4.1)}$$

where ΔT_{-2}, ΔT_{-1}, ΔT_{+1}, and ΔT_{+2} are the four values measured at locations symmetric with respect to the central value. Generally, the accepted level for the noise envelope, as evaluated by the fourth difference, should be less than ± 0.05 nT for data sampled at 10 Hz (Coyle, M.; Dumont et al., 2014). The F0.5 and F3.0 datasets were resampled at 10 Hz, and the fourth difference was evaluated (Figure 4.1.7). The unfiltered F0.5 data shows a strong noise, with an FDIFF ranging from −4 nT to 4 nT. However, after the filtering, the fourth difference values were well inside the ± 0.05 nT range. In the case of the F3.0 dataset, the unfiltered data were practically already inside the ± 0.05 nT range.

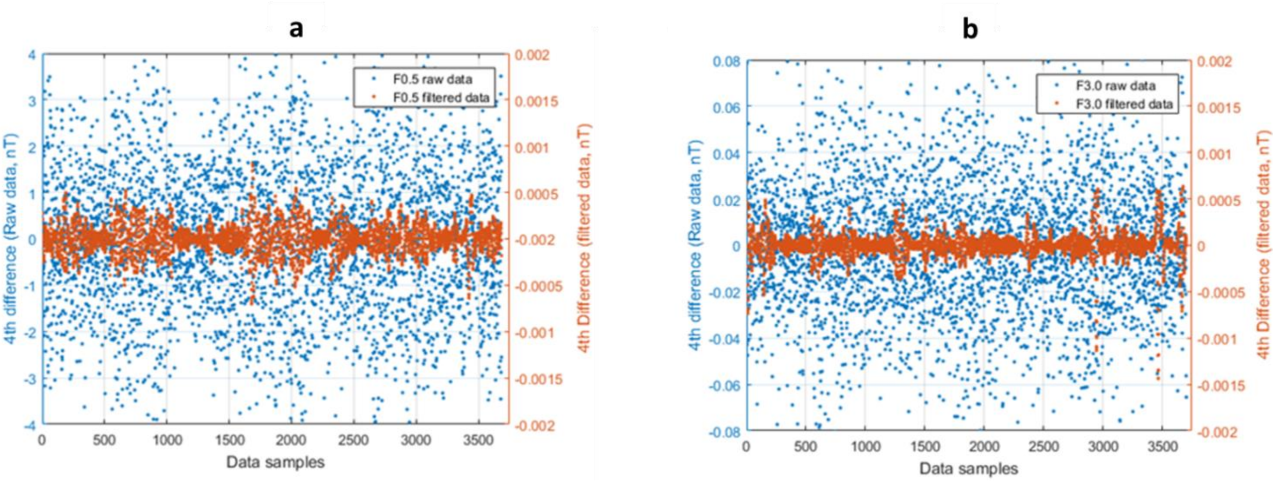

Figure 4.1.7. The calculated fourth difference of F0.5 (**a**) and F3.0 (**b**) datasets. Blue points refer to the raw data (amplitudes on the left *y*-axis), and red points refer to the filtered data (amplitudes on the right *y*-axis).

As a standard processing step, we interpolated the data recorded along the seven profiles for the two drone-borne datasets to have a map of the magnetic anomalies in the area, using a gridding cell of 1 × 1 m^2. The position, amplitude, and shape of the anomalies shown in the maps of the raw (Figure 4.1.8 a,b) and filtered data (Figure 4.1.8 c,d) were similar. The two total field maps showed a maximum amplitude variation of about 280 nT, ranging from about −150 to 130 nT, and we identified two main groups of anomalies, one trending NE–SW and located in the central sector, displaying the greatest amplitudes, and the other in the northern sector approximately trending in an E–W direction. Small amplitude differences between the two maps can be attributed to the different noise levels, to the inaccuracy of the flight altitude, which was set by GPS, and which may have slightly differed between the two surveys, and to the inaccuracy of the GPS horizontal positioning in areas with strong magnetic gradients.

Based on previous information and on the magnetic anomalies' shapes, we can infer that the sources of the anomalies were probably buried pipes and, perhaps, cables. In fact, the magnetic anomalies display the typical alternating magnetic highs and lows that can be measured above a metal pipe (Sowerbutts, W.T.C. 1998). The individual sections of metal pipes acquire a permanent magnetization during manufacture, forming single magnetic dipoles. The direction of the magnetization varies from one pipe section to another depending on the orientation of the pipe, and this reflects in the systematic variation of the anomaly amplitudes, and/or sign, above a pipeline (Sowerbutts, W.T.C. 1998).

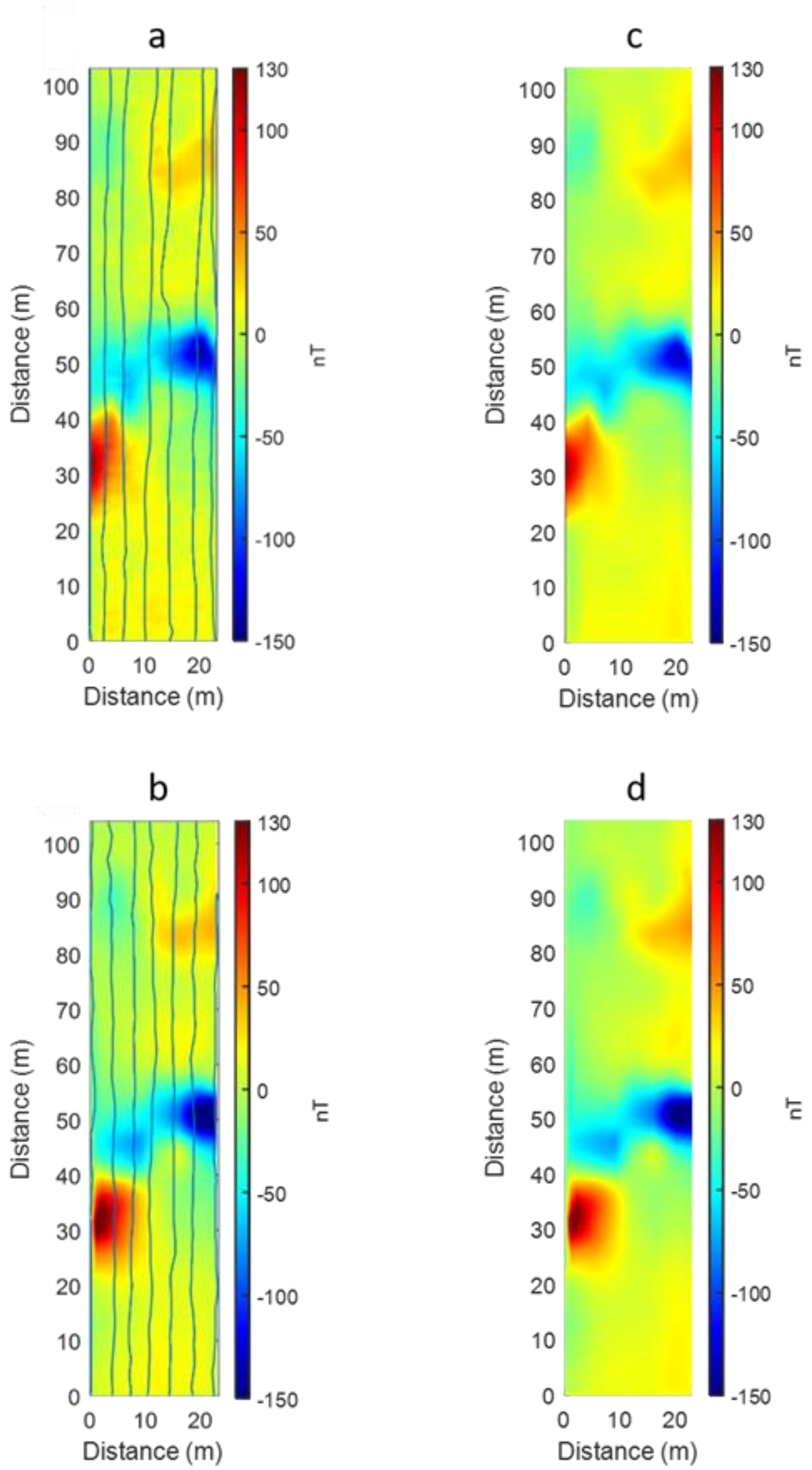

Figure 4.1.8. Magnetic anomaly maps. (**a**) F0.5 survey, raw data; (**b**) F0.5 survey, filtered data; (**c**) F3.0 survey, raw data; (**d**) F3.0 survey, filtered data. The blue lines in (**a**) and (**c**) represent the true flight paths during the two surveys.

To better locate the buried sources of the magnetic anomalies in the area, we computed the total gradient, also known as the amplitude of the analytic signal (Roest, W.R. et al., 1992). In the total gradient maps (Figure 4.1.9), the anomaly sources should be located in correspondence to the maxima, except for possible small offsets that theoretically should not be present when computing the total gradient due to 2D sources along a data profile. The maps of Figure 4.1.9 clearly show the source position in the central sector, while in the northern zone the number and location of the sources appears more uncertain. The analysis of the total gradient computed along the data profiles (Figure 4.1.9c) can help to better distinguish all the sources present, because of the very high spatial detail (the sampling step is only 2 mm). From the analysis of all the data profiles the probable presence of linear anomalies elongated in the NE–SW direction can be recognized, with two of them in the northern area (80 m < y < 95 m) and one in the central area (20 m < y < 60 m). The intense anomaly in the central area may also be the result of the coalescence of the magnetic effects of two nearby linear structures.

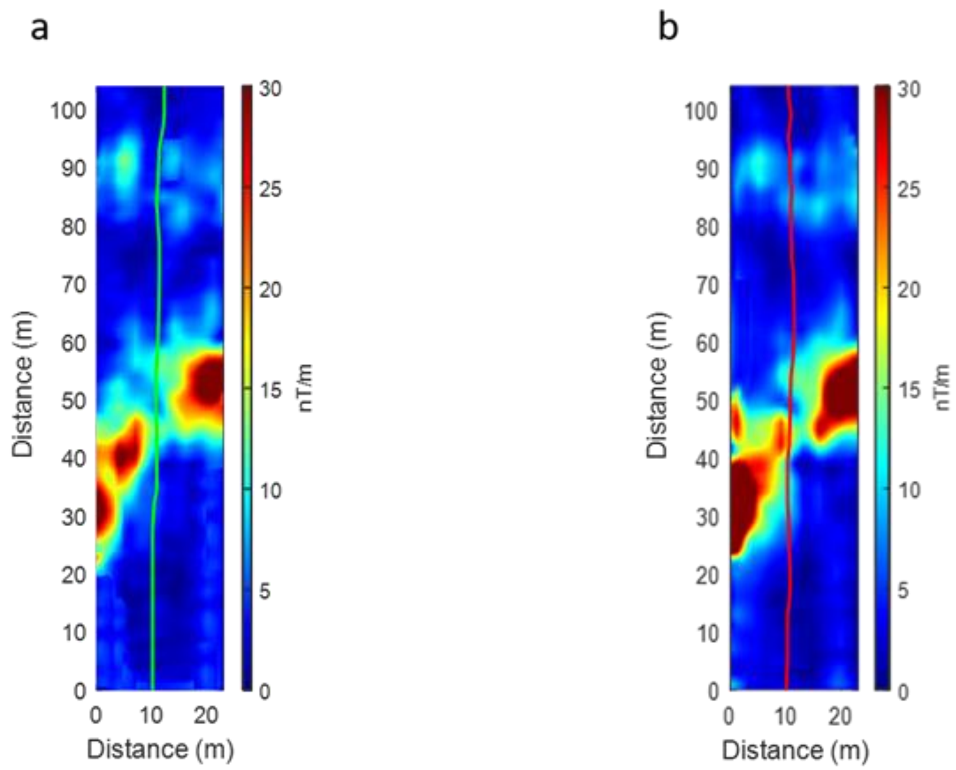

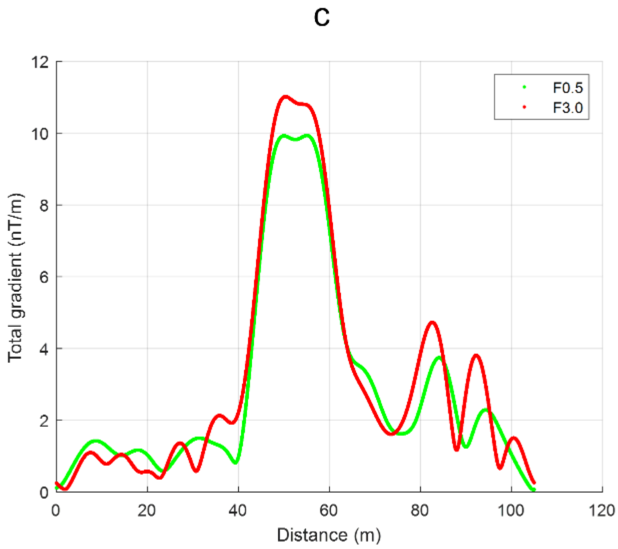

Figure 4.1.9. Total gradient maps relative to filtered F0.5 (**a**) and F3.0 (**a**) UAV datasets; (**c**) total gradient computed along a filtered profile (located by green and red lines in (**a**) and (**b**)). The green line refers to the F0.5 dataset, and the red line refers to the F3.0 dataset.

Ground Survey Magnetic Data

The magnetic data of the ground survey were analyzed with the same procedures used for the UAV data. Interestingly, the scalogram of the ground data (Figure 4.1.10) appeared very similar to the scalogram of the F3.0 drone-borne dataset, relative to a magnetometer–UAV distance of 3 m (Figure 4.1.4b). In the ground-data scalogram, the frequency band relative to the target signal results was similar to that of the drone-borne data (compare Figures 4.1.10 and 4.1.4) because the speed was then only about 1 m/s, while the half-wavelength of the anomalies of interest was reduced to about 10 m, implying again a frequency of about 0.05 Hz. In the ground data case, the peak at 50 Hz can be ascribed entirely to the power electrical lines present in the area. However, the same 50 Hz peak was also visible in the UAV data, with a magnitude very similar when the distance between the magnetometer and UAV rotors was set to 3 m. This similarity between the 50 Hz peak amplitude between ground data and F3.0 data suggests that magnetic data are relatively free of UAV-generated noise when the magnetometer sensors are at a distance of at least 3 m from the UAV. Other minor peaks appeared at different frequencies in the ground and UAV scalograms. These peaks cannot be related to oscillations of the magnetometer during the data acquisitions, as the spectral content of the attitude data (not shown) showed peaks at higher frequencies, associated to a very low power.

As the power of the target signal was concentrated at frequencies similar than in the UAV case, to remove the power related to the noise and preserve the useful signal at lower frequencies, we applied to the ground data along each profile the same low-pass filter designed for the UAV data (cut-off frequency of 0.5 Hz, using a Hanning window). The result of the filtering and the comparison with the original data is presented in Figure 4.1.10b as the sum of power of the scalogram for each frequency.

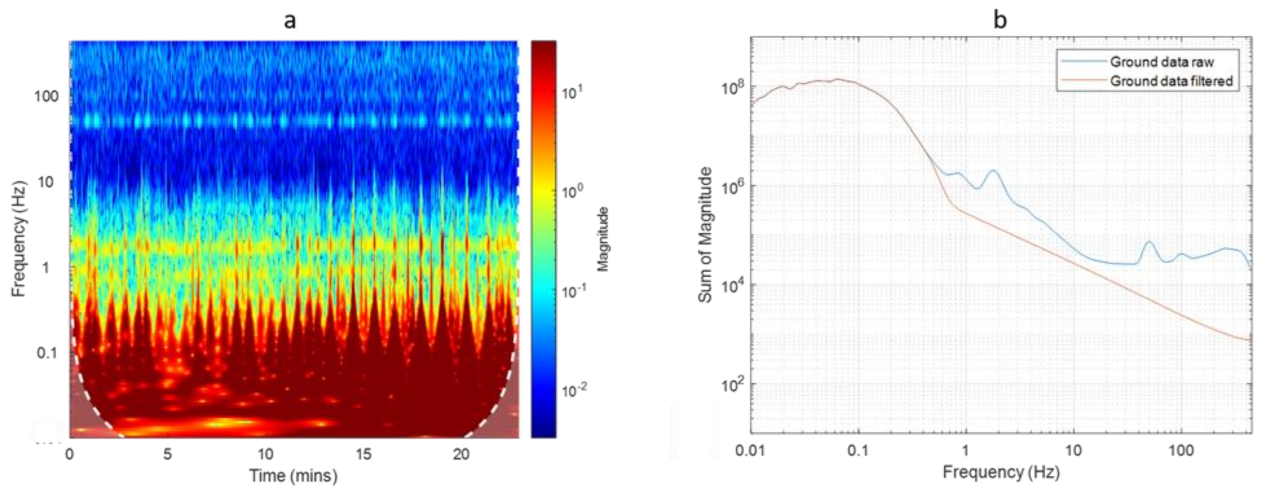

Figure 4.1.10. Spectral analysis of ground data. (**a**) Scalogram of ground data. Edge effects in the computation of the spectrum may be significant in the dimmed area below the dashed white line; (**b**) sum of power of the scalogram for each frequency.

The ground total-field anomaly data were interpolated on the survey area using a gridding cell of 0.5 × 0.5 m^2, and the total gradient was also computed to allow for an easier horizontal location of the sources (Figure 4.1.11). The main features of the magnetic anomaly map are the presence of the typical alternating magnetic highs and lows that can be measured above a metal pipe (Sowerbutts, W.T.C. 1998) and already described for the UAV data (Figure 4.1.8). Here the magnetic anomalies are sampled at a higher resolution and clearly show the presence of two NE–SW linear sources in the northern area (55 m< y< 85 m), about 10 m apart from each other, and probably just one linear source in the central area (0 m < y < 50 m), although the presence of another source located north of the main one cannot be completely excluded (Figure 4.1.11b,c).

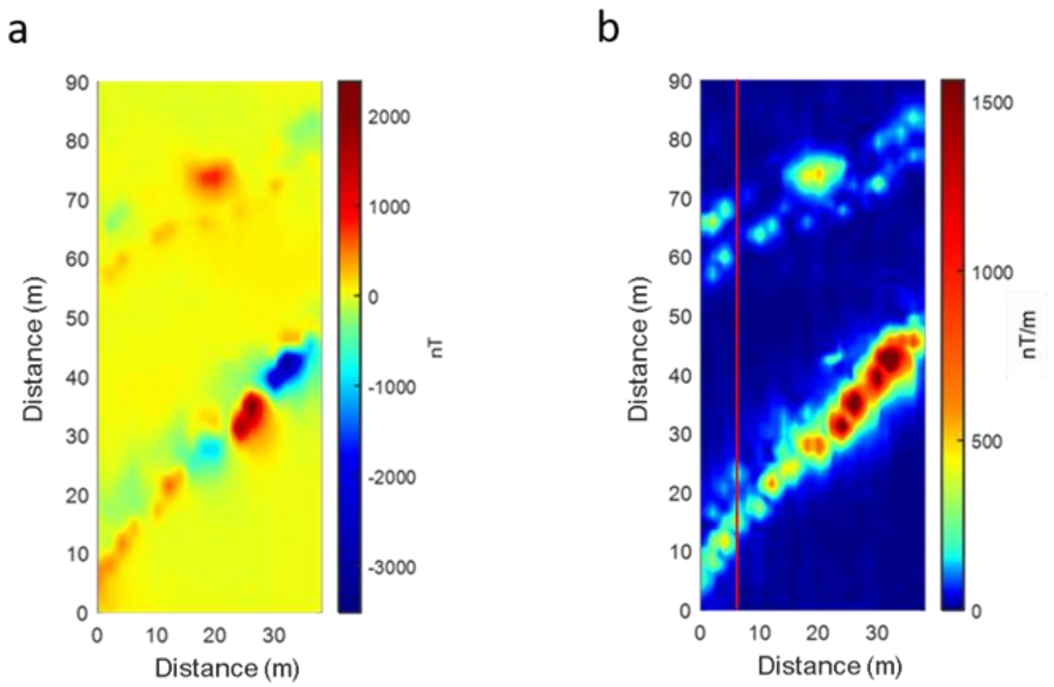

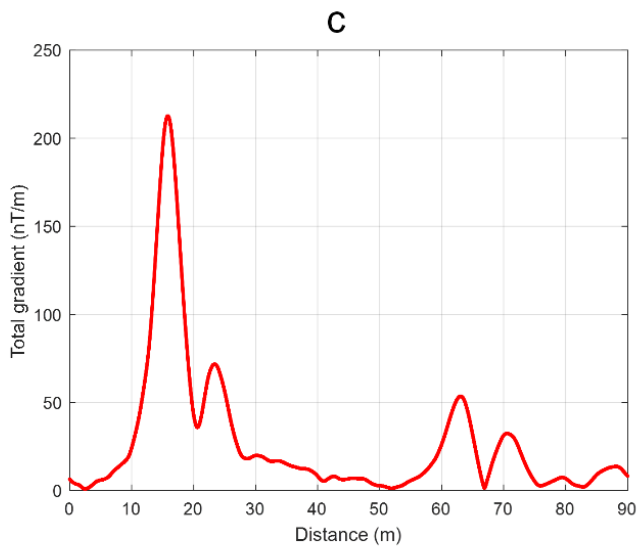

Figure 4.1.11. Ground survey dataset. (**a**) Total field anomaly map; (**b**) total gradient map; (**c**) total gradient of the profile data at x = 6 m (red line in Figure 11b). The secondary total gradient peak (at x = 25 m in this data profile) is sometimes visible on other profiles and could be related to another linear source.

Source Depth Estimation

The estimate of the source depth from drone-borne data can represent a quantitative quality control when compared to depths obtained from ground data, which we can consider as a reference for clean and valid data. With this modelling, we wanted to check if the different conditions in which the magnetic field was measured during the flights with the magnetometer at 0.5 m and 3 m from the drone and the successive data filtering might have distorted the signal or, conversely, if the integrity of the target signal was preserved (Florio et al., 2014).

Euler deconvolution is a semi-automated method to estimate the source depth from potential field data, which is based on the Euler homogeneity of the magnetic field generated by simple sources (Thompson 1982, Reid et al., 1990). In its standard version, the method assigned an integer "structural index" value, associated with simple sources (dipole, line, sheet, half-space). In the case in study, consistently with the presence of linear sources (Figures 4.1.8 and 4.1.11), we could safely assume a structural index value equal to 2, characterizing a horizontal line of dipoles. We applied this technique to the profile data acquired during both UAV and ground surveys, as they were characterized by a very small spatial sampling step (Figure 4.1.12). This should imply an advantage in terms of results accuracy with respect to the analysis of the maps, as they are obtained by interpolation using a much larger grid step size. However, the surveyed profiles do not cross perpendicularly these two-dimensional sources, so that a correction factor was applied to the estimated depths, equal to the cosine of the angle between the profile direction and a line perpendicular to the source (Milsom, 2003). Consistently with the model of horizontal line of dipoles, the estimated depths can be considered as relative to the center of the buried pipes. The Euler deconvolution analyzes the data profiles with a moving-window approach, producing many solutions. In our case, the window size chosen was of 2.5 m (501 points). The selection of best solutions was based on the error associated to the depth estimate obtained by the least squares solution to the overdetermined linear system of equations (Reid et al., 1990).

As already pointed out, the number of sources clearly visible along the data profiles varied from UAV and ground datasets, probably because of coalescence effects at the flight altitude. Thus, we obtained two groups of Euler solutions for UAV data (S1 and S2, relative to anomalies located in the central and northern sectors, respectively) and three groups from ground data (L1 in the central sector and L2 and L3 in the northern one).

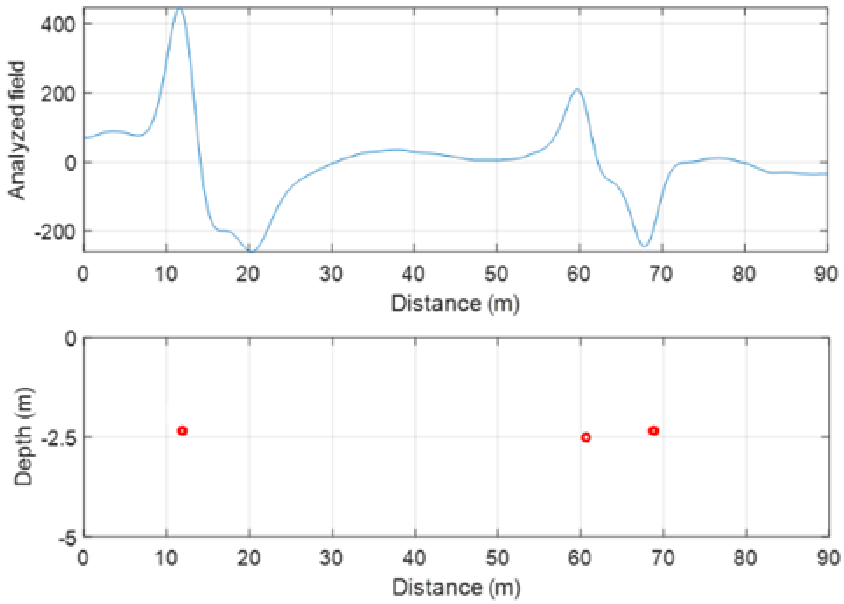

Figure 4.1.12. Example of the Euler deconvolution application to profile data. (**a**) Ground survey total field profile at x = 4 m; (**b**) Euler deconvolution solutions (red dots), localized at the position of the center of the sources of the magnetic anomalies.

The estimated depths were significantly consistent for the three different datasets, so that the results are very satisfying (Tables 4.4.1 and 4.1.2). In detail, the data acquired in the F0.5 configuration provided average depths of 1.76 m for the source of anomaly S1, which was 7% less that the average depth (1.9 m) obtained from the F3.0 configuration and ground datasets. In the northern sector, UAV data individuate a single anomaly, and in this case the depth estimated from two aerial datasets were consistent (average depth of 1.76 m). On the other hand, the ground survey had a sufficient resolution to separate the effects of two linear sources at average depths of 1.7 and 1.8 m, showing a very good agreement with the depth estimated from drone-borne magnetic data.

Table 4.1.1. Estimated depths along the profiles acquired with F0.5 and F3.0 configuration.

	F0.5 configuration		F3.0 configuration	
	S1 anomaly	S2 anomaly	S1 anomaly	S2 anomaly
Profile 1	1.8 m	1.8 m	2.0 m	1.5 m
Profile 2	1.6 m	1.8 m	2.0 m	1.8 m
Profile 3	1.6 m	1.8 m	1.8 m	1.8 m
Profile 4	1.8 m	1.8 m	2.0 m	1.8 m
Profile 5	1.8 m	1.5 m	1.8 m	1.8 m
Profile 6	1.8 m	1.8 m	1.8 m	1.8 m
Profile 7	1.8 m	1.8 m	1.8 m	1.8 m
Mean Value	1.74 m	1.76 m	1.9 m	1.76 m
Standard deviation	0.10 m	0.11 m	0.11 m	0.11 m

Table 4.4.2. Estimated depths along the profiles acquired with F0.5 and F3.0 configuration.

	Ground Survey		
	L1 anomaly	L2 anomaly	L3 anomaly
Profile 1	1.9 m	1.5 m	1.9 m
Profile 2	1.5 m	1.9 m	1.5 m
Profile 3	1.9 m	1.9 m	1.9 m
Profile 4	1.9 m	1.9 m	1.9 m
Profile 5	1.9 m	1.9 m	1.9 m
Profile 6	1.9 m	1.5 m	1.9 m
Profile 7	1.9 m	1.9 m	1.9 m
Profile 8	1.9 m		1.5 m
Profile 9	1.9 m		1.9 m
Profile 10	1.9 m	1.5 m	1.9 m
Profile 11	1.9 m		1.9 m
Profile 12	1.9 m	1.9 m	1.9 m
Profile 13	1.9 m	1.5 m	1.5 m
Profile 14	1.9 m	1.5 m	1.9 m
Profile 15	1.9 m		1.9 m
Profile 16	1.9 m	1.9 m	1.9 m
Profile 17	1.9 m	1.9 m	1.9 m
Profile 18	1.9 m	1.5 m	1.5 m
Profile 19	2.0 m	2.0 m	2.0 m
Profile 20	2.0 m	2.0 m	2.0 m
Mean value	1.89 m	1.7 m	1.81 m
Standard deviation	0.10 m	0.21 m	0.19 m

4.1.4 Discussion

In this study, we tested the quality of drone-borne magnetic data acquired using two different flight configurations. In the first configuration, the magnetometer was fixed to the landing sled at a distance of 0.5 m to the rotors, while in the second configuration the magnetometer was suspended 3 m below the UAV. The two configurations illustrate the possible solutions to obtain, on the one hand, the stability of the UAV-magnetometer system during flight and, on the other hand, the minimization of the magnetic and electromagnetic noise generated by the mobile platform. As was well shown by (Walter et al., 2019), the periodic swinging of the magnetometer during flight, when the magnetometer is suspended to the drone, may induce a noise at a characteristic frequency, which depends on the magnetometer–UAV distance, while the magnetic and electromagnetic noise related to the drone is concentrated at high frequencies, with a main peak at around 50 Hz. It is clear that the need to stabilize the magnetometer during flight and to minimize the UAV-related noise solicit the implementation of contrasting strategies, so that the solutions tested in this study can be considered as end-members of possible flight configurations for a magnetometer-UAV system.

We compared the power spectral densities of the datasets collected during the UAV flights and the ground survey. This comparison allowed us to distinguish the frequency contribution due to the target signal from that due to the magnetostatic and electromagnetic interference of the mobile platform. Walter et al. (2021) carefully studied the magnetic and electromagnetic interference components generated by the DJI M600 hexacopter and as recorded by a Geometrics 1000 Hz MFAM sensor, which is the same drone-magnetometer system used in the present study. They distinguished four sources of interference signals, namely, (a) the mechanical rotation of the motors, (b) the permanent magnets in the motors, (c) the electrical commutation due to the passage of an AC current in the solenoids of the motor, and (d) the induced magnetic field generated by the ferromagnetic cores of the motor's armatures. During flight, these interference components are characterized by a main peak frequency at 50 Hz, with part of the power centered at higher frequencies (Walter et al., 2021). Some of these components may even be aliased in the 1000 Hz sampled magnetic field (Walter. et al., 2021). What was observed in the scalograms relative to both the drone-borne datasets (Figure 4.4) was consistent with these findings.

The free periodic swinging of a 3-m suspended magnetometer should induce an interference signal with a central peak at about 0.38 Hz (Walter et al., 2021). The amplitude of this interference component was influenced by (a) the UAV speed and (b) the magnitude of the horizontal and vertical gradients of the magnetic field in the volume of the oscillations. This peak was not clearly visible in our data (Figure 4.5) because it had a relatively high power only in the data acquired during UAV turns between the survey lines, but these low-quality data were removed in a preliminary processing step. In fact, we processed the data relative to the turns of the drone between adjacent lines (including the first samples along each line) and could verify, by the computation of the CWT scalogram, the presence of a magnitude peak at the expected frequency of 0.38 Hz, as predicted by (Walter et al., 2019) for a F3.0 flight configuration.

The main difference between the scalograms shown in Figure 4.1.4, relative to the F0.5 and the F3.0 configurations (UAV rotors–magnetometer sensors distance of 0.5 m and 3 m, respectively), was relative to frequencies higher than 0.5 Hz. In fact, when the magnetometer sensor was very near to the UAV, the power associated with frequencies higher than about 2 Hz increased to about one order of magnitude with respect to the F3.0 flight configuration. In the case studied in this article, the combination of the wavelength of the target signal and the survey speed assured a clear spectral separation between the primary target frequencies (<0.5 Hz) and the primary platform interference frequency (50 Hz) observed. This allowed a clean separation of these contributions using a low-pass filter with a cutoff frequency of 0.5 Hz. This cutoff frequency was higher than that used in other studies (e.g., Walter al., 2019 used a 0.2 Hz cutoff frequency), thus better preserving the integrity of the target signal. It is important here to highlight the role of the UAV speed on the time-domain spectral frequency of the target signal. In the case studied in this article, a speed of 5 m/s would have increased the target signal frequency to 0.125 Hz, implying a possible overlap with noise components.

Another difference between the F0.5 and F3.0 datasets regards the amplitude of the heading error, associated with opposite flight directions during the survey. To quantify the heading error from our dataset is not an easy task, as we did not acquire data along the same profile in opposite directions. However, we tried to obtain some insights by comparing the residual signal after filtering along adjacent profiles, as shown for two of them in Figure 4.1.6. The different amplitude of the removed signal was attributable to the different heading error when flying in opposite directions. We could estimate a static offset of +/−7 nT between opposite flight lines in the F0.5 configuration and of +/−0.15 nT between opposite flight lines in the F3.0 configuration. These values were related to the drone-magnetometer configuration used in this study and should be re-evaluated for other systems. However, they highlight the difference in amplitude of this effect for the two flight configurations used.

As already mentioned, the spectral content of ground data was very similar to that of the aerial dataset when the magnetometer was far from the drone, demonstrating that a distance of 3 m is sufficient to effectively attenuate most of the electromagnetic noise for this specific UAV-magnetometer system.

Finally, the very similar depth to source obtained from modelling the low-pass filtered drone-borne magnetic data and ground data demonstrate the soundness of the post-processing strategies.

4.1.5 Conclusion

In conclusion, our final recommendations are the following:

• The magnetometer could be placed even very near to the UAV in all the cases when it is necessary, increasing flight security and stability (for example, in case of rugged terrain, in the presence of vegetation near the programmed flight altitude, or in case of non-optimal weather conditions);

• In general, the flight speed should be sufficiently slow to favor a good spectral separation between noise and signal, and this is especially important if the UAV–magnetometer distance is small;

• if positioned very near to the drone, a good practice should be to program the flight without performing the 180° turn at the end of each line, thereby avoiding strong heading errors—this procedure is simply implemented using flight programming software;

• the use of a magnetometer operating at a fast acquisition rate (in our case, 1000 Hz) is strongly advised to adequately sample the high frequencies (50 Hz or more) typically associated to UAV electromagnetic noise. This noise, if in aliasing, can contaminate the frequency band associated to the useful signal.

The results presented in our study regard the survey over intense magnetic anomalies, such as those generated by near-surface metallic objects. In case of weaker magnetic effects (e.g., in archaeological areas or for some mining applications), a very short UAV–magnetometer distance, similar to the first used in the present study, may not produce satisfying results, and further research is needed to assess the optimal flight configuration. In these cases, the amplitude of the target signal and that of the noise floor may be similar, and a simple filtering, as described in this article, might not be sufficient to obtain a clean signal.

4.2 The drone-borne magnetic survey as the optimal strategy for high-resolution investigations in presence of extremely rough terrains: The case study of the Taverna San Felice quarry dike.

4.2.1 Introduction

The advantages achieved with the introduction of drones make UAV magnetic surveys a practical and often preferable alternative to the traditional ground and airborne surveys. This choice reduces costs, time, and risks compared to other acquisition techniques and allows the realization of surveys with a very high resolution and uniform aerial coverage. However, in difficult ground conditions, the UAV magnetic survey could be complex, but at the same time, the only alternative for data acquisition. These ground conditions include the presence of dense vegetation, cultivated areas, swamps, glaciers, lakes, foreshore areas or steep mountain slopes. In these cases, standard approaches to ground surveys may not be feasible, and high-altitude airborne prospections may not provide the requested spatial resolution.

In literature, several authors have demonstrated the efficacy of UAV aeromagnetic data collection and proposed different flight configurations, highlighting that the main problem related to UAV magnetic surveys is the magnetic and electromagnetic disturbance due to the UAV platforms

(Malehmir et al., 2017; Parvar et al., 2018; Walter et al., 2020; Nikulin et al., 2020; De Smet et al., 2021; Parshin et al., 2018; Walter et al., 2019a; Walter et al., 2019b; Walter et al., 2021; Li et al., 2018; Phelps et al., 2022). The proposed solutions consist in suspending the magnetometer sensors 2–5 m away from the drone motors or by attempting some post-acquisition filtering of the data (Mu et al., 2020). However, hanging the magnetometer sensor to the drone with long ropes can create unwanted periodic variations in the acquired magnetic data, generated by the oscillations of the magnetometer sensor. Moreover, the suspended weight may cause flight instabilities and can increase the flight-related hazard, for instance in presence of vegetation near the programmed flight altitude or in case of non-optimal weather conditions. In fact, when it is necessary to increase flight security and stability, at least in the case of surveys over intense magnetic anomalies, a practical solution for carrying the magnetometer may be to rigidly attach it to the drone's landing gear (at only about 0.50 m from the engines; Accomando et al., 2021). Other authors propose safer solutions using shorter suspension distances (about 1 m; Veloski et al., 2018; Kaub et al., 2021) or avoiding suspending the magnetometer by mounting the magnetometer at the end of a fixed large arm (Cunningham, 2018; Tuck et al., 2019).

In this study, we present the results of a drone-borne magnetic survey aimed at mapping an igneous dike intruded in sedimentary rocks, which was exposed by excavation activities in an active quarry. We chose to attach the magnetometer to the landing gear of a drone as the best option to overcome the limitations to ground data acquisition posed by the complex terrain geometry, the steepness of the slope, the presence of bush vegetation, and ongoing extraction activities.

In the following, the geologic setting will be briefly described, then the magnetic survey will be presented with detail, along with the processing and the modelling of the data and the final geologic conclusions.

4.2.2 Geological setting

The study area (41.364580° N, 14.033225° E - 41.364333° N, 14.039127° E) is an active quarry for limestone extraction, at Taverna San Felice, near the town of Presenzano (Campania Region, southern Italy), on the southwestern slope of the Mt. Cesima ridge, northeast of Roccamonfina volcano (Figure 4.2.1a). This part of the southern Apennines is characterized by a Pleistocene structural depression (Garigliano Graben, Figure 4.2.1a) hosting the Roccamonfina volcano, whose activity ranged between 630 and 50 ka (e.g., Conticelli et al., 2009), mainly emplacing lavas and scoriae from scattered vents, and ignimbrites from the summit area (e.g., De Rita and Giordano, 1996).

Since the late 1980s, excavation activities in the Taverna San Felice quarry have progressively exposed a magmatic dike embedded in a dominant calcareous succession formed by well-bedded Lower Cretaceous limestones (Calcari a Requenie Fm.), covered by Upper Cretaceous-Paleocene breccias (Calcari Cristallini Fm.), and Lower Pleistocene breccias (Vitale and Ciarcia, 2018). At the base of the quarry, the magmatic dike is broadly oriented E-W and moderately dipping northward, switching to sub-vertical and NE-SW oriented moving upward (Figure 4.2.1b, c; Natale et al., 2023). The dike is composed of a main sheet, over 250 m long and with thickness varying in the range of 5–25 m and several minor apophysis, a few meters long. The contact between the dike and the host rock is sharp and regular at the base, while it is more irregular towards the top of the quarry (Natale et al., 2023). The dike fed a fissure eruption that emplaced up to 10–15 m thick Strombolian deposits, which mainly crops out in the upper part of the quarry and reworked at the base of the slope. These deposits overlay a series of altered pyroclastic deposits ascribed to Roccamonfina volcano (Natale et al., 2023; Figure 4.2.1d). The dike and its tephra pertain to tephrites-phonotephrites compositions (Natale et al., 2023), overlapping with the compositions reported in Di Girolamo et al. (1991). In the upper part of the quarry, welded spatter ramparts occur, representing the preserved record of the vent system (Natale et al., 2023). The dike outcrops are scattered among the several 5 m high vertical steps of the quarry, whereas outside the excavated area the steep slope covered by a dense bush vegetation make direct inspection and geological mapping a challenging task. To better understand the aerial extension of the dike and the related volcanic products and to define its direction and its relationship with tectonic lines over an area larger than the quarry, a magnetic survey was planned. Given the above-mentioned ground conditions, a UAV-based magnetic survey was the preferred acquisition strategy.

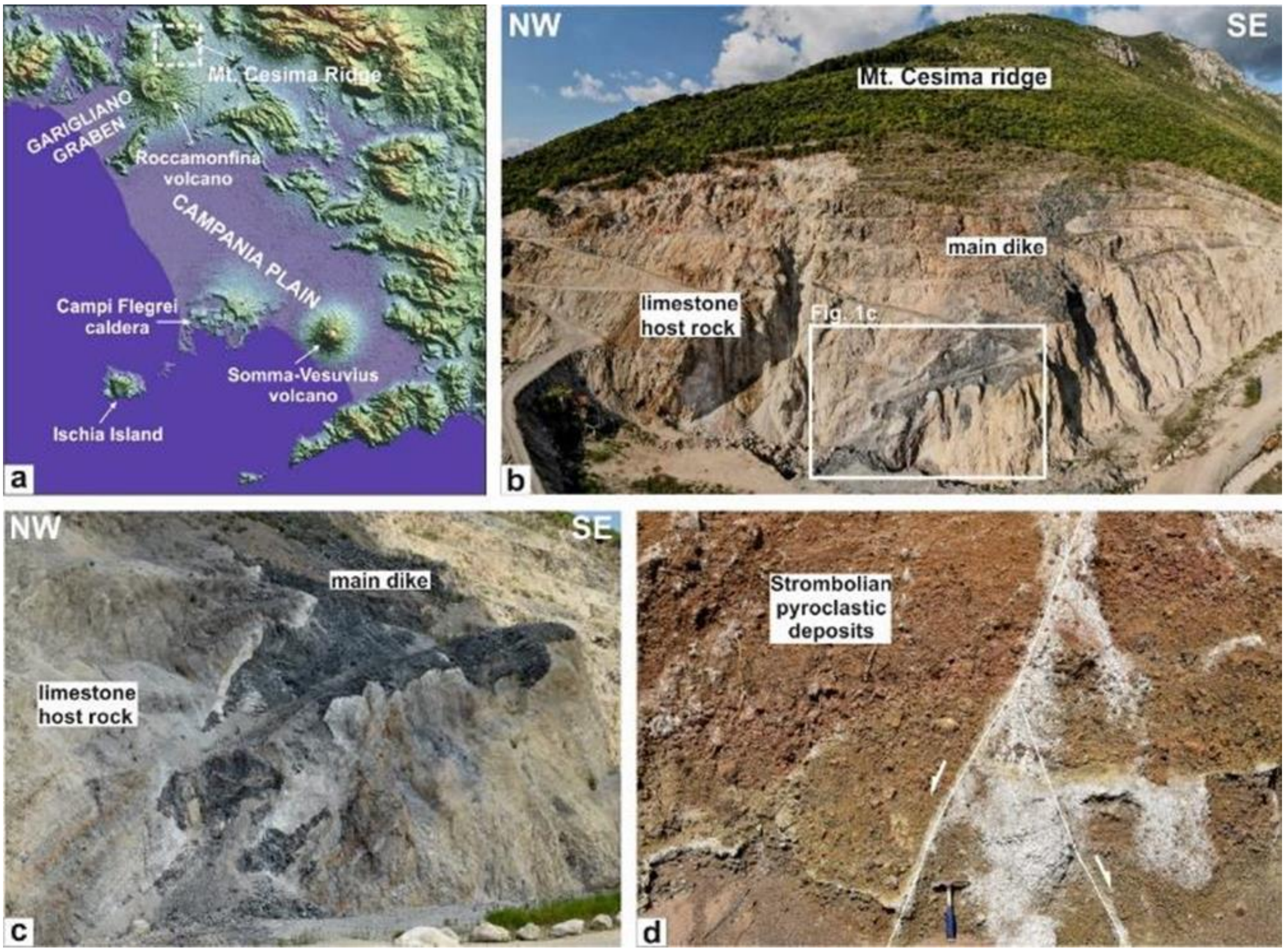

Figure 4.2.1. (a) Location of the study area with respect to the main volcanic centres of Campania Plain (southern Italy). **(b)** Wide-angle UAV picture of the Taverna San Felice quarry excavation front. Location of Figure 1c is marked by the white box. **(c)** Detail of the contact between the magmatic dike and the carbonatic host rock at the base of the quarry excavation front. **(d)** Example of the Strombolian pyroclastic succession exposed in the upper part of the quarry.

4.2.3 Measurements and survey design

The drone-borne magnetic survey was conducted during April and May 2022. The UAV used for this acquisition is a DJI Matrice 600 Pro hexacopter (hereafter M600P), which can fly for 32 min without payload and a maximum of 22 min with a payload of 2 kg according to atmospheric conditions (e.g., wind speed). UAV magnetic data were collected using the Geometrics Micro-Fabricated Atomic Magnetometer (MFAM) in the “Development kit” version (hereafter MFAM-DK), which includes a laser-pumped atomic magnetometer with two cesium alkali-vapor sensors and a development board with an onboard GPS module. The high sampling rate of 1000 Hz allows obtaining an unaliased measurement of 50 Hz fields relative to power lines and the correct identification of the high-frequency magnetic noise caused by the propellers (Walter et al., 2021). This specification, in addition to the small weight (about 1 kg) and the high sensitivity, make this magnetometer ideal to be integrated in a UAV system.

The MFAM-DK was housed inside a light, aerodynamic and nonmagnetic custom bird, made of polystyrene, having a thin and rigid base (a Nomex honeycomb sandwich panel). The total payload weight was < 2.0 kg (Figure 4.4.2a).

One of the main choices affecting the data quality and the operativity of the UAV system regards the way the magnetometer is attached to the drone. To overcome the difficulty of flying along irregular and steep terrain (slope > 60%; Figure 4.4.2c), and to improve flight safety, we chose to attach the magnetometer to the drone’s landing gear, at only 0.50 m from the engines (Figure 4.2.2b). Moreover, this choice prevents the generation of noise in the data due to magnetometer swinging when it is attached to the UAV with long ropes**.**

In such configuration, the data are contaminated by an intense high-frequency noise generated by static and time-varying magnetic fields. However, these effects are confined to the high-frequency part of the spectrum with a major peak at 50 Hz. Thanks to the very high sampling step of the MFAM magnetometer they can be correctly sampled, easily identified in the spectrum, and removed with a low pass filtering. The high amplitude of this noise (more of 20 nT in this survey) implies that such a configuration could be used only when strong magnetic anomalies are expected (Accomando et al., 2021). This is the case of a shallow magmatic intrusion surveyed at a few meters’ altitude, where simple forward models show total field anomalies with an amplitude few hundreds of nT.

Nine individual flight surveys were needed to cover the study area at an elevation of 20 m AGL (above ground level), and 81 parallel survey lines were flown with a 10 m horizontal line separation. To ensure flight safety and constant height above terrain, flight missions were planned using a high-resolution DSM (1 m × 1 m) generated with photogram metric data surveyed just before the magnetic acquisitions.

Surveys profiles were oriented along a direction approximately North–South to maximize the magnetometer performance and avoid falling into the sensors dead zone. To prevent the magnetic heading error, the flights were performed avoiding the 180 ◦ turn at the end of each survey line, as suggested by (Accomando et al., 2021). Overall, the duration of each flight was approximately 15 min long and a total of over 16 km in a linear distance of magnetic data were acquired. The geomagnetic field in this area had a declination of 4° and an inclination of 57°.

With MFAM-DK operating at 1000 Hz and with a flight speed of about 2 m/s, the sampling step of the magnetic data along the survey lines was as small as about 2 mm. Since the built-in GPS receiver of the MFAM-DK did not produce satisfactory results, the positional data recorded by the UAV's GPS were used instead (declared horizontal ac curacy ±1.5 m). Magnetic data were synchronized with UAV positional data by means of the GPS time simultaneously recorded by both the MFAM-DK and M600P GPS receivers. As the magnetic sensor is rigidly fixed to the drone landing gear, as explained later, there is no horizontal offset between the magnetometer and the UAV so that we geo-localized the magnetic data using directly the coordinates recorded by the internal GNSS receiver of the drone.

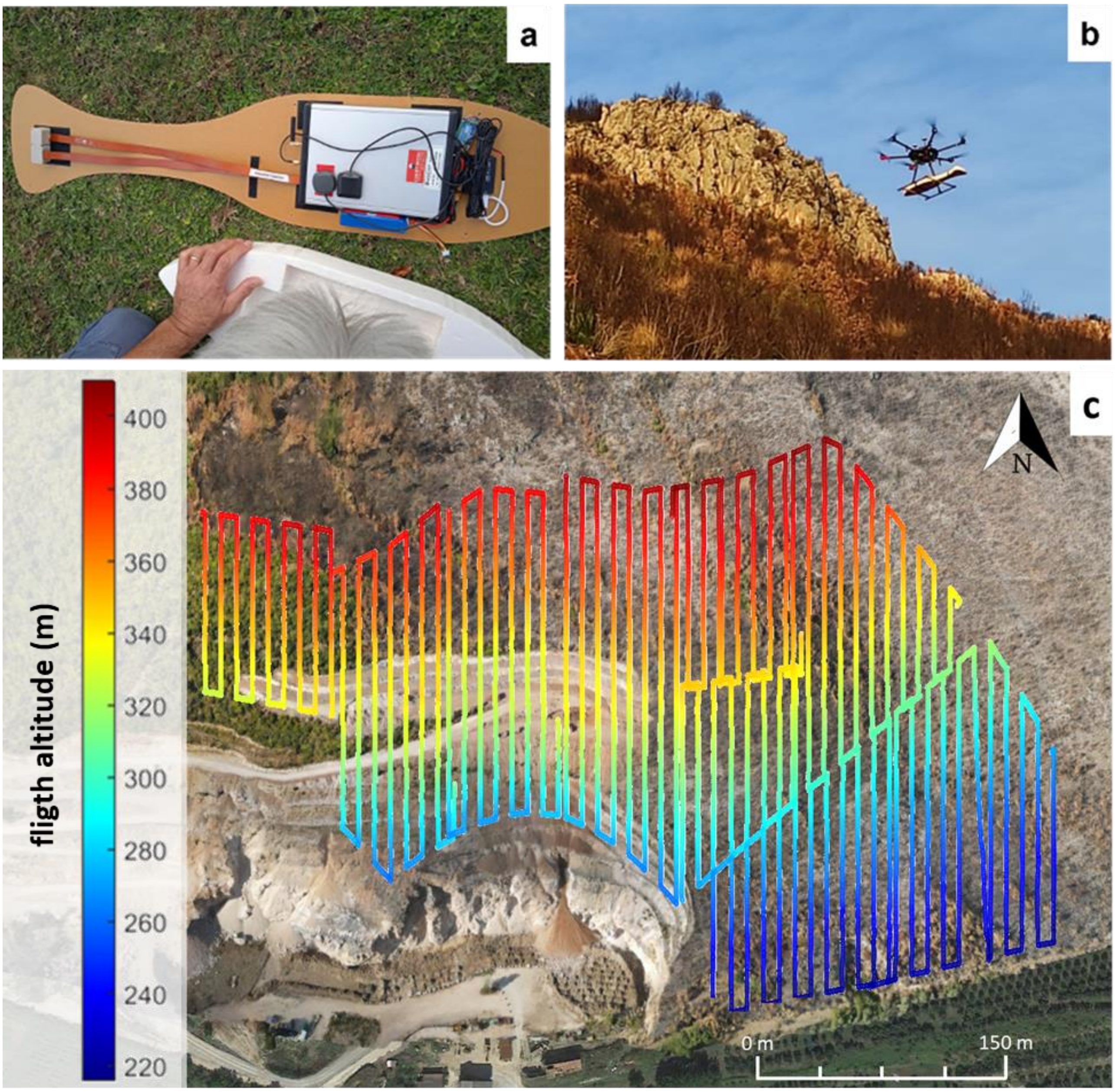

Figure 4.2.2. (a) Arrangement of the Geometrics MFAM “Development kit” magnetometer inside the prototype bird; **(b)** Field photograph showing the flight configuration with the magnetometer fixed to the platform landing sled, 0.5 m below the UAV; **(c)** Flight paths and altitude variation along the surveyed lines.

4.2.4 Results

Total field magnetic anomalies

The data analysis included the removal of the magnetic data recorded during the drone turns at the end of each profile, as they may have a reduced accuracy. As the surveyed area has a limited extension (Magnetic Declination: +4° 10'; Inclination: 57° 15'), the International Geomagnetic Reference Field (IGRF) was approximated by a single constant value (46,548.5 nT) that was subtracted to all the datasets. The diurnal variation of the magnetic field, monitored by a GEM Overhauser magnetometer at a station near the survey area, was negligible in the time span of a single flight, so no temporal correction was applied to the nine datasets, also considering the strong amplitude of the measured anomalies. A constant level adjustment of a few nT among the data collected in the various flights, done in the same day or in different days, was instead necessary. The resulting unfiltered Total- Field Anomaly (TFA), as displayed in the example profile of Figure 4.2.3, shows a high-frequency noise with a peak-to-peak amplitude of about 25 nT that characterizes the signal during all the flight duration. This disturbance is associated to the magnetic and electromagnetic interference fields generated by the UAV platform, and its high amplitude is due to the small distance between the drone engines and magnetic sensors (0.5 m).

Spectral analysis in the wavelet time-scale domain guided us in exploring the variation of the frequency content of the data through time, distinguishing the noise and signal components of the data. Here, through the continuous wavelet transform (CWT) we obtained a scalogram of the datasets in the time domain using a “Morse wavelet” and we present the modulus of the complex set of CWT coefficient for the drone-borne datasets (Figure 4.2.4a). The sum of the scalogram at each frequency (Figure 4.2.4b) summarizes the spectral content of the data. The prominent peak around 50 Hz can be interpreted by the presence of a significant platform-induced magnetic and electromagnetic interference sensed by the magnetometer and to, a lesser extent, also the electrical power lines present in the area.

By this analysis, we could highlight the ability of MFAM-DK to correctly sample high-frequency magnetic noise as well as other peaks at smaller frequencies, not associable with geological sources. In fact, to estimate the frequency band associated with the target signal, we can evaluate the ratio of the UAV speed and the horizontal anomaly extent (representing a half-wavelength of the signal) multiplied by two (Walter et al., 2021). In our case, the data analysis along each flight profile shows that the geological sources should have an anomaly half- wavelength of about 40–80 m (Figure 4.23a). Considering the UAV speed of 2 m/s, we estimate a target signal frequency band between 0.0125 Hz and 0.025 Hz. Thus, we designed a Hanning-window low-pass filter in the time-domain with a cut-off frequency of 1 Hz, which removes the noise and preserves the lower frequency signal associated to the geological sources.

The filtered data collected along the 81 profiles were interpolated on a 2.5 m × 2.5 m grid to have a map of the magnetic anomalies in the area. Figure 4.2.5 shows the total field magnetic anomalies detected in the study area, presenting a maximum amplitude variation of about 1600 nT, ranging from about 400 to 1200 nT. The magnetic effect of the dike can be identified as a linear magnetic high trending WSW-ENE, from the quarry area, where it is outcropping, to the mountain slope. There, the magnetic high assumes a nearly elliptical shape, slightly elongated in a NW-SE direction. The variation of the amplitude of the linear anomaly can be easily correlated with its depth to the top, with the highest values related to the outcropping part. South of the circular feature it can be noticed the presence of an isolated smaller anomaly. It is interesting to notice how these very intense main anomalies identify a well delimited area with the magnetic field decreasing abruptly outside it. This evidence can be ascribed to the presence of very shallow, or even outcropping, magnetized rocks. Other minor anomalies north of the linear anomaly are instead unrelated to the volcanic products and being generated by trucks and excavators present there during the survey.

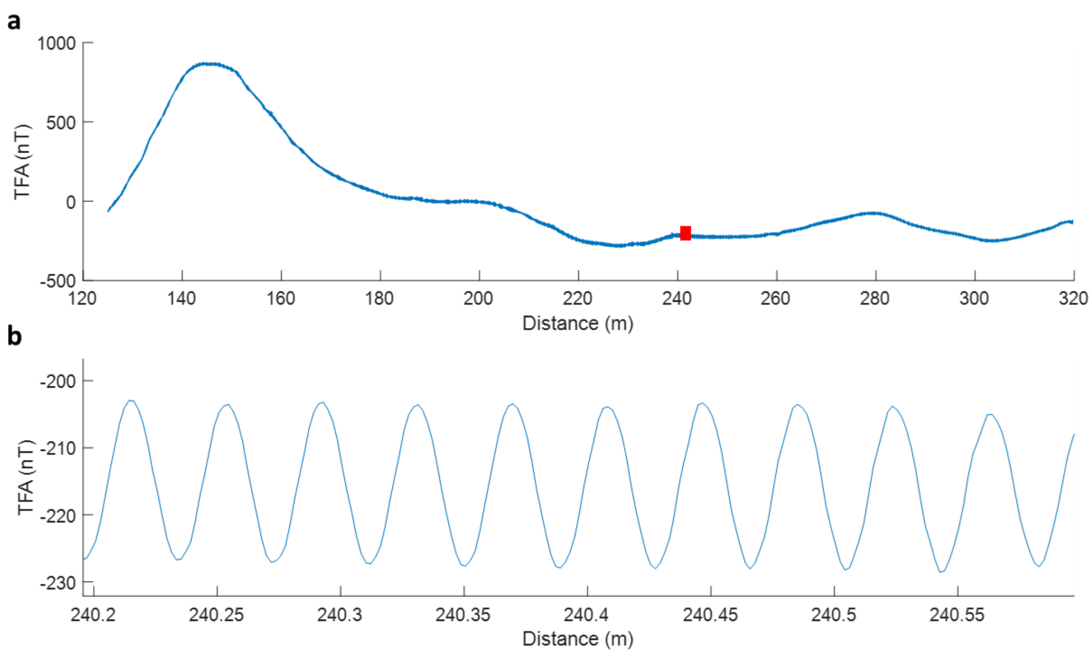

Figure 4.2.3. Unfiltered Total-Field Anomaly (TFA) acquired along the profile n. 31; **b)** the unfiltered data enclosed in the red rectangle in Figure 3**a**. (For interpretation of the references to colour in this figure legend, the reader is referred to the web version of this article).

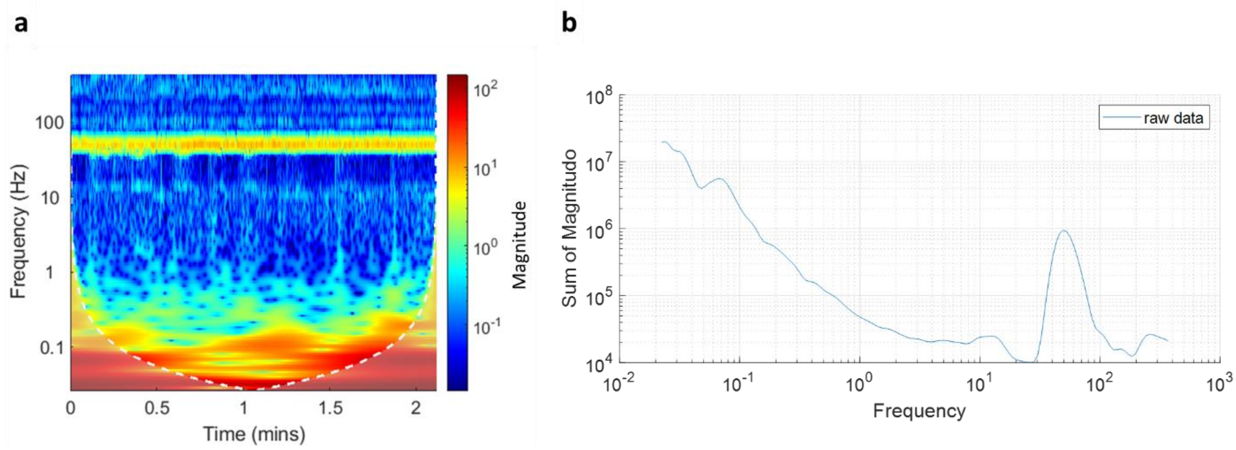

Figure 4.2.4. Continuous wavelet transform (CWT) analysis of the magnetic dataset. **a)** Time-domain scalogram of the unfiltered TFA acquired along the profile n. 31, computed using a "Morse" wavelet; **b)** Sum of the scalogram magnitude at each frequency.

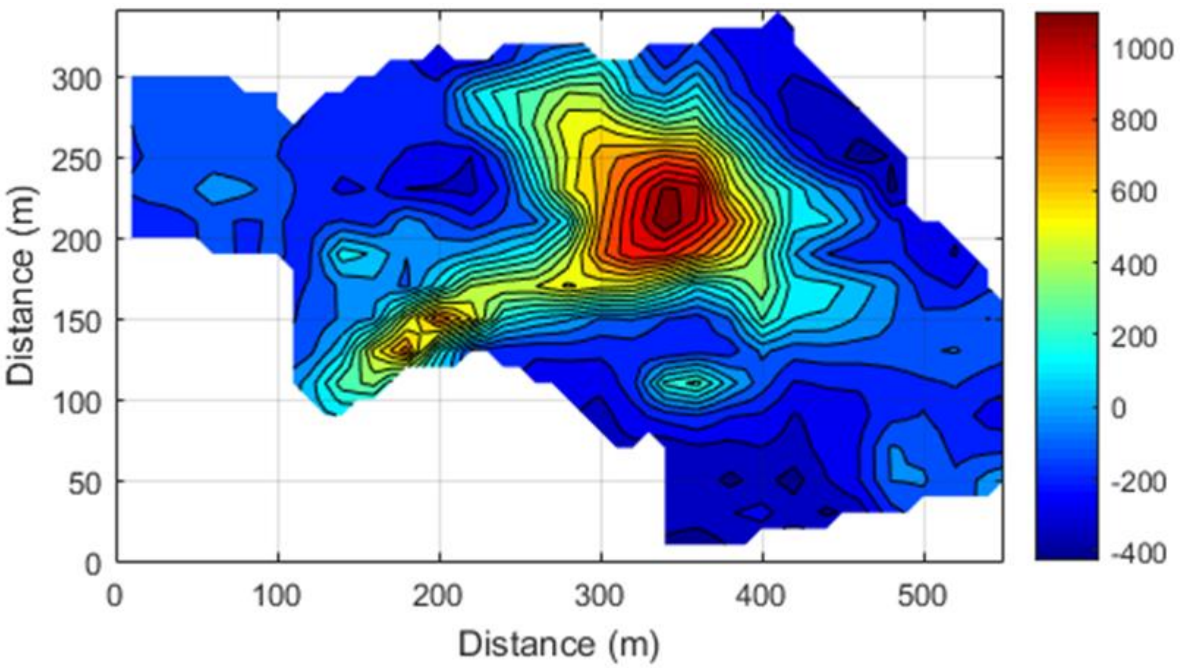

Figure 4.2.5. Total field anomaly map obtained from filtered data.

Forward modelling

A subsurface model can provide important information for geological interpretation. For example, it can suggest a probable propagation mechanism of the intrusion, and its thicknesses, providing a useful information for the reconstruction of the stress field at the time of the intrusion or for studying the influence of pre-existing faults that could have influenced its direction. Therefore, we performed a 2.5D forward modelling along three different sections (Figure 4.2.7a) to reconstruct a model, giving some geological insights. The modelling was performed by commercial software based on the method described by Talwani and Heirtzler 1964 and Won and Bevis 1987. As the magnetic models suffer nonuniqueness, they must be constrained by independent information. We performed a field experiment concerning the estimate of the intensity of the total magnetization (induced plus remanent) of the dike rocks, according to the method outlined by Breiner 1973. This method is based on the identification of the maximum value of the total field recorded by a total field magnetometer while a rock sample is rotated at a certain distance from the sensor along the local direction of the magnetic field. The method assumes that the rock sample can be considered as a dipolar source. In our case, we used two rock samples having a roughly spherical shape. The volume of the samples was 331 cm^3 (sample #1) and 1495 cm^3 (sample #2). The test was repeated three times for each sample and the maximum total field value recorded was retained and used for the magnetization estimate (Figure 4.2.6). Although the method is expected to provide only a rough estimate of the total magnetization, in our case the results were satisfying in that the estimated value is very similar for the two samples (16.5 A/m and 16.1 A/m). Thus, we considered the estimated values as representative of the total magnetization, and the average value of 16.3 A/m was used as a constraint for our forward modelling.

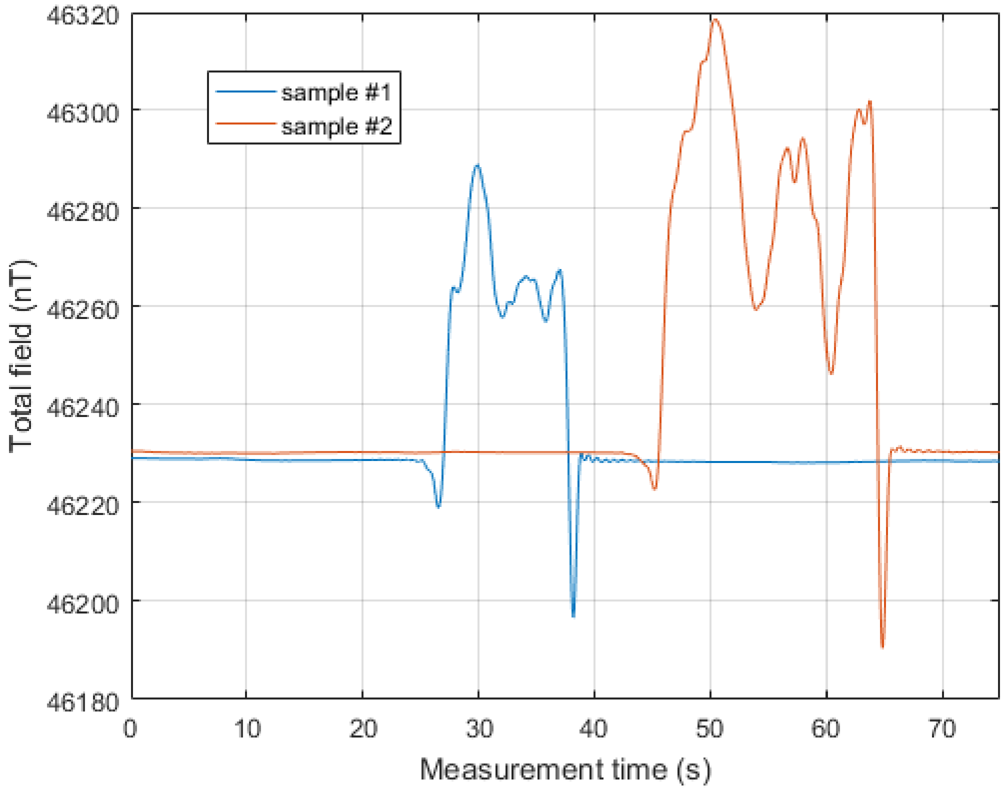

Figure 4.2.6. Total magnetization estimations by the Breiner 1973 method. The two curves represent the total field variation caused by the presence of rotating igneous rock samples. The flat parts of the curves are relative to the background magnetic field in the absence of the rock samples. The rotation of the samples may cause the alignment of the induced and remanent magnetization vectors, resulting in the maximum total field value recorded. According to the Breiner 1973 method, the maximum value is combined with the sample volume and the distance separating the rock sample and the magnetometer sensor to estimate the total magnetization.

The first profile (section A-A', in Figure 4.2.7a) orthogonally crosses the part of the dike outcropping along the quarry wall. Thus, in this case, we could model the source of the magnetic field using two solid constraints, namely the depth to source's top (0 m) and its magnetization (16.3 A/m). We could fit the total field anomaly satisfactorily by assuming a dike thickness of 8.5 m and if the dike steeply dips northward with an angle of about 80°. The observed data show northwest of the dike anomaly another magnetic anomaly related to the presence of trucks and excavators during the survey, which was not considered in the modelling. To account for the limited extension of the dike in the W direction, the 2.5D model has a length of 50 m in the westerly strike direction. The misfit between the observed and predicted data may be evaluated by the relative error, defined as:

$$\frac{||obs-pred||}{||obs||} \; x \; 100 \qquad \textbf{(4.2)}$$

where *obs* stands for the observed total field anomaly, *pred* stands for the magnetic data predicted by the model and ‖•‖ stands for the L2 norm. In the case of profile A-A', the relative error was 6.35% when considering only the South-Eastern part of the profile, relative to the dike anomaly.

The second profile (B-B ' in Figure 4.2.7a) crosses the dike anomaly in an area, east of the previous profile, where it is not outcropping. In this case, we constrained the model using the estimated total magnetization, and the same thickness and dip as estimated in the modelling of the A-A' profile, and we could constrain the depth to the top of the buried body, which resulted to be about 7–8 m (Figure 4.2.7c). This profile crosses the dike anomaly at its approximate center, so that a 2D model is reasonable in this case. To the north of the dike anomaly, another anomaly, less intense, can be noticed. The analysis of the total field anomaly map (Figure 4.2.7a) allows to easily associate it to the main circular anomaly further east. However, we tried to model only the anomaly clearly related to the dike, neglecting this feature as well as the South-Eastern tail of the main anomaly along this profile, clearly influenced by the effects of other sources. The resulting model predicts a field that has a relative error of 6.68% (the error was computed only in the central part of the profile, including only the main anomaly).

The third profile (C-C in Figure 4.2.7a) crosses the main and most intense magnetic anomaly. Geologic field work allowed to relate it to the presence of Strombolian pyroclastic succession and welded spatter ramparts, probably associated to the eruption fed by the dike (Natale et al., 2023). Also in this case, we use the dike magnetization, thickness, and dip as a-priori information. We built a model where the dike is present at a depth of about 8 m while, at shallower depth and outcropping, a layer of welded spatter and pyroclastic deposits (having a maximum thickness of 10–15 m) is present. The magnetization of the volcanic products is considered to be the same of the main magmatic body. In this case the modelled sources in the direction of strike extend to 75 m. To the South of the main anomaly, another magnetic high is clearly visible. It is modelled with the presence of shallow to outcrop ping volcanic material, but it may be equally well justified by a deeper source, perhaps a branch of the main dike. We did not try to fit the magnetic profile south of this last anomaly, probably generated by other sources not crossed by the profile. The relative error for the data predicted by this model is 4.23% (the error was computed excluding the southern tail of the anomaly profile).

Finally, we tested the modelling sensitivity to the dike inclination. Thus, we varied the dip of the model dike along the profile B-B ' shown in Figure 4.2.7c by ±10°, leaving the other model parameters unchanged. The resulting models are presented in Figure 4.2.8. It is clear that the 10° variation in dip produces strong variations in the predicted field, with large relative errors of the field produced by these alternative models (44% for a vertical dike, 52% for a dip of 70°). Thus, the estimated dike inclination of 80°, obtained from the model along the A-A' profile, should be considered as a rather reliable indication about the true dike dip angle.

a

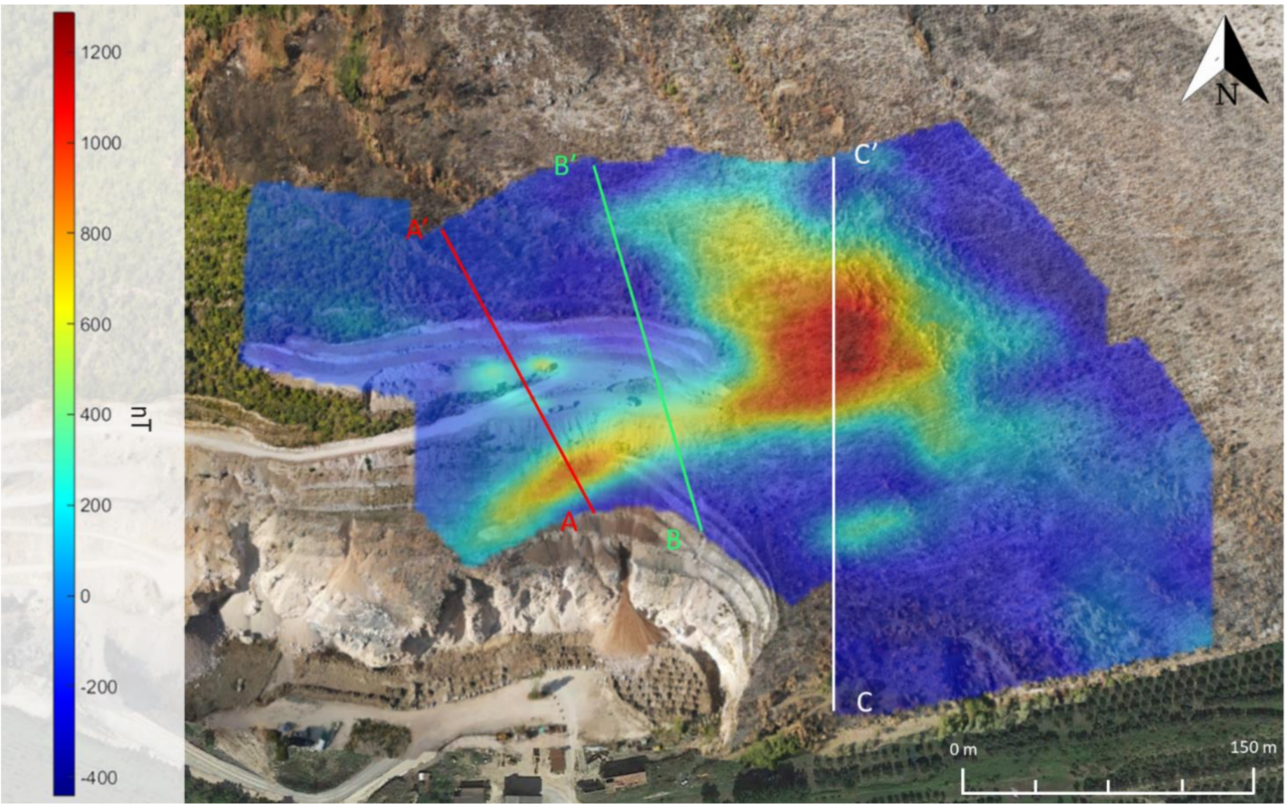

b

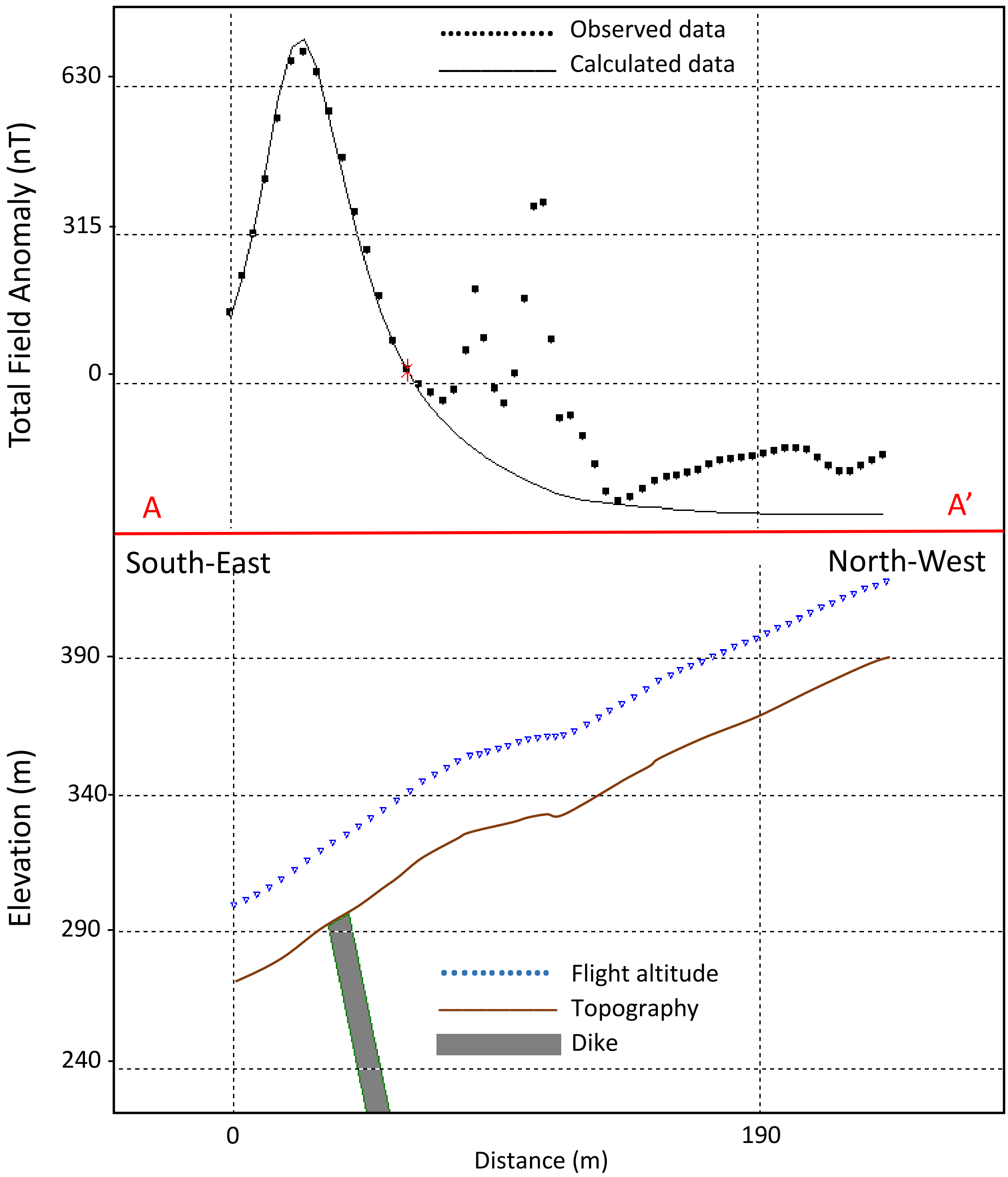

Observed data
Calculated data
Total Field Anomaly (nT)
630
315
0
A
A’
South-East
North-West
Elevation (m)
390
340
290
240
Flight altitude
Topography
Dike
0
190
Distance (m)

c

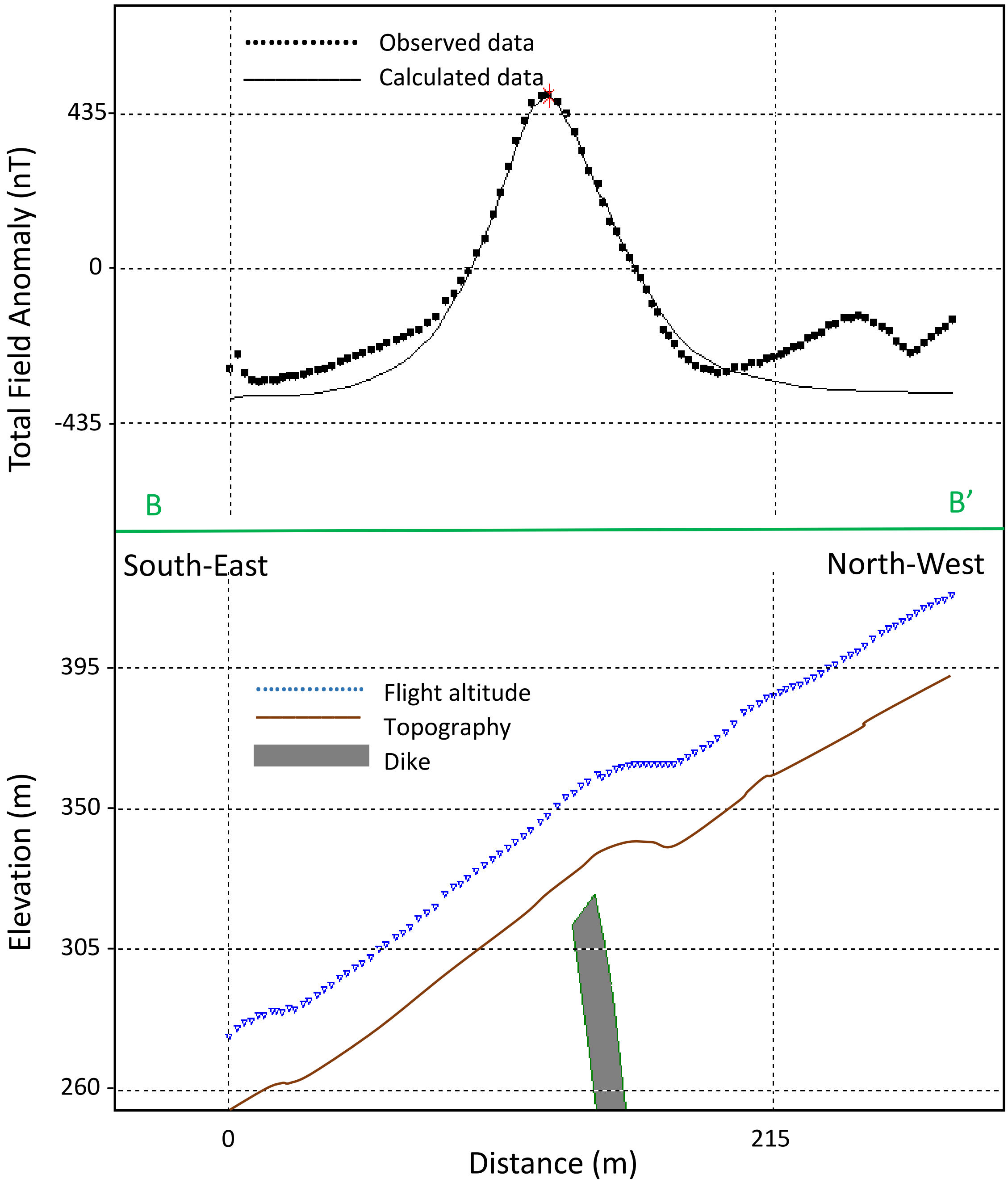

Observed data
Calculated data
435
0
-435
Total Field Anomaly (nT)
B
B’
South-East
North-West
Flight altitude
Topography
Dike
395
350
305
260
Elevation (m)
0
215
Distance (m)

d

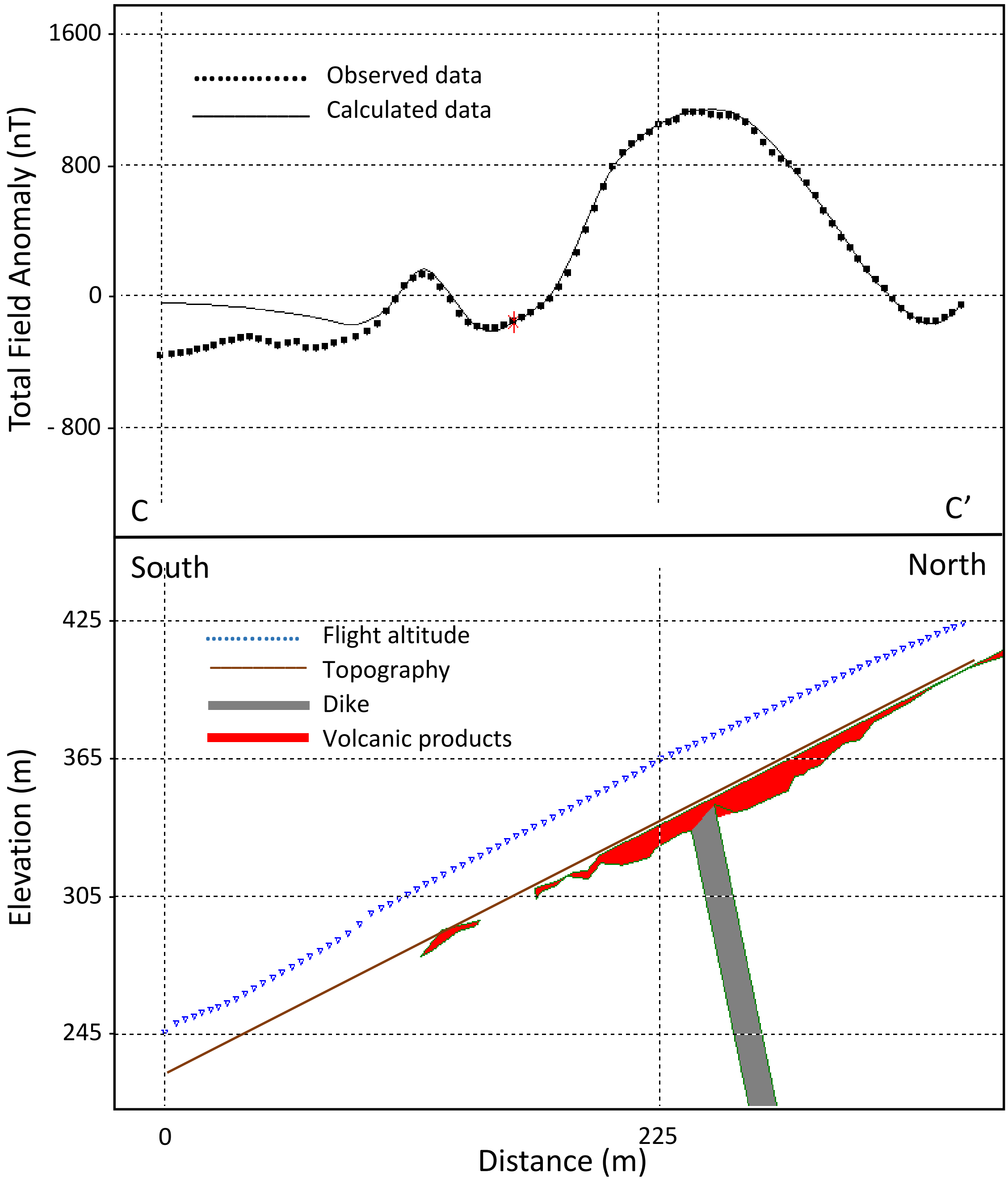

Figure 4.2.7. Forward modelling. **(a)** Total field magnetic anomalies superimposed on a satellite image of the survey area. The lines identify the positions of the three modelled profiles. **(b)** Source modelling along the profile A-A'. **(c)** Source modelling along the profile B-B'. **(d)** Source modelling along the profile C-C'.

a

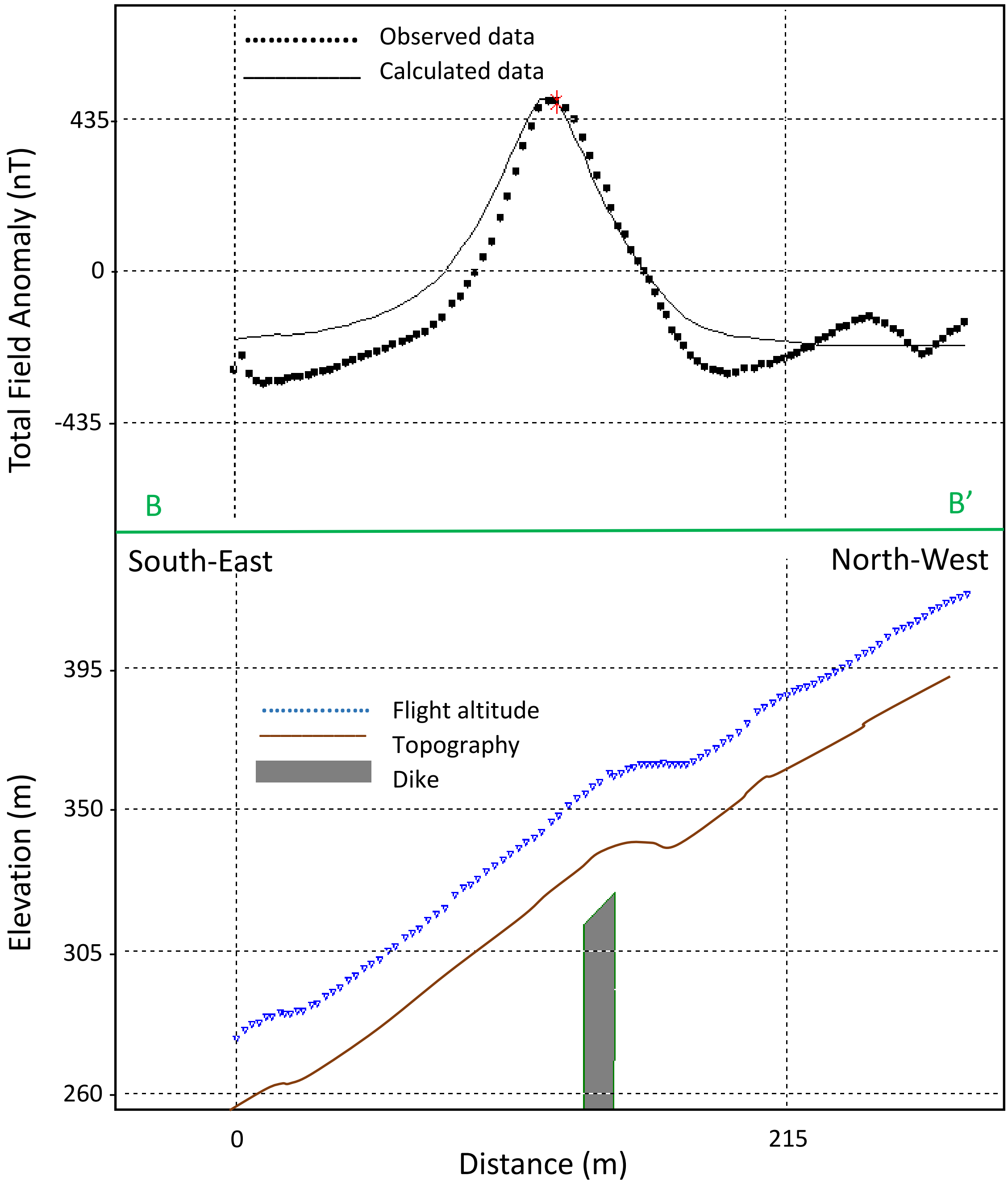

Observed data
Calculated data
435
0
-435
Total Field Anomaly (nT)
B
B'
South-East
North-West
395
350
305
260
Flight altitude
Topography
Dike
Elevation (m)
0
215
Distance (m)

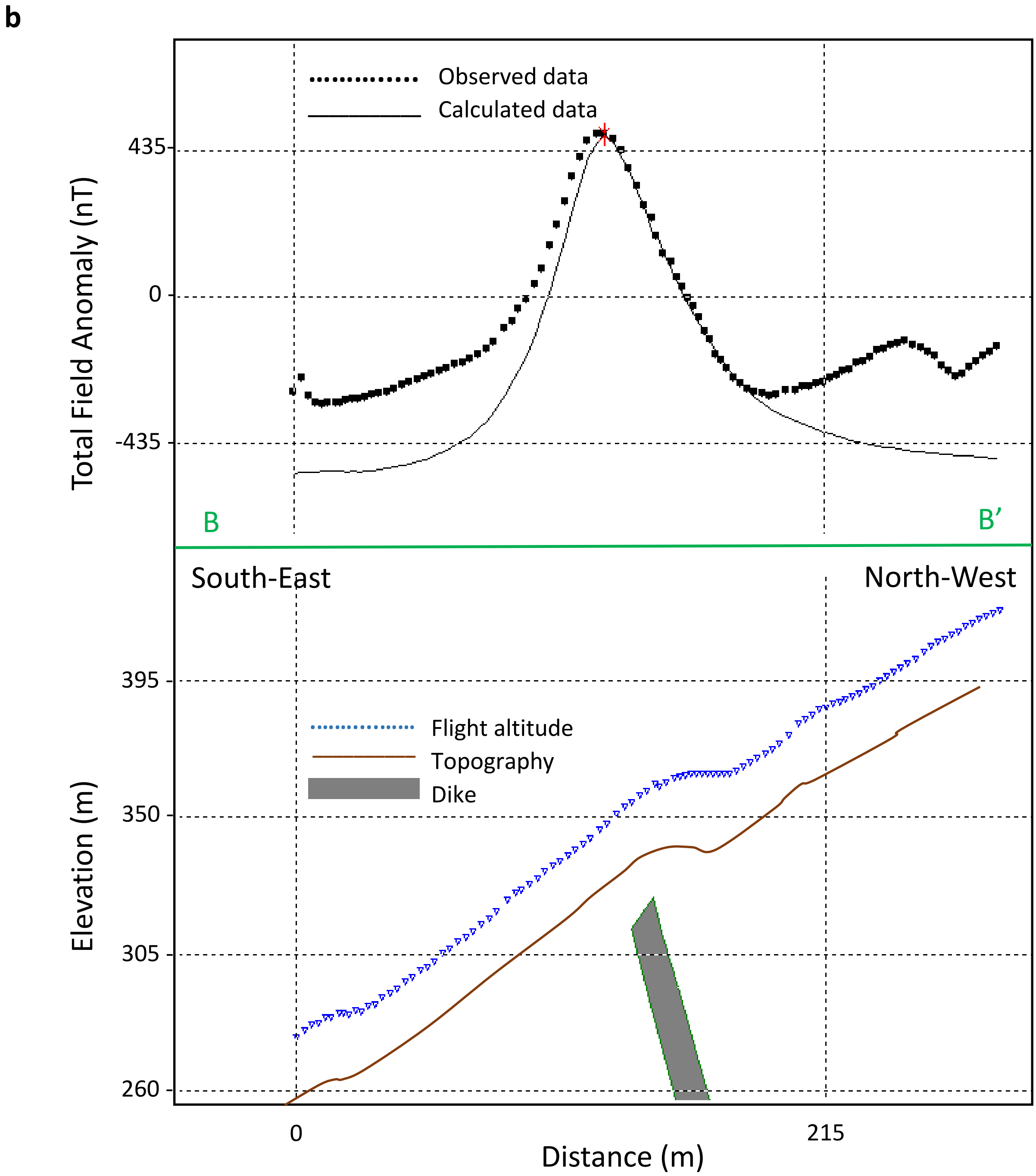

Figure 4.2.8. Test of the modelling sensitivity to the dike inclination along the profile B-B'. **(a)** Source modelling increasing the dike inclination of 10° (the dike is vertical); **(b)** Source modelling decreasing the dike inclination of 10° (the dike inclination is 70°).

4.2.5 Discussion

We mapped an igneous dike partially emerging along a quarry wall and could follow its trace and the related volcanic products on a steep mountain slope. The use of the drone allowed a high-resolution, safe, and rapid investigation despite the dangerous excavation areas of the quarry and the dense vegetation surrounding it. The MFAM-DK magnetometer was fixed directly to the drone landing sled. This solution increased the stability and security of the flight and is practicable from the signal-to- noise ratio point of view, considering the intense magnetic anomalies due to the strong magnetization contrast between volcanic and sedimentary rocks. However, flying with the sensor very close to the UAV engines amplifies the noise due to the magnetic and electromagnetic interference having a peak frequency at about 50 Hz, as shown in the scalogram of Figure 4.2.4. Walter et al. (2021) showed as the slightly nonsymmetric magnetic field of all permanent magnet pairs presents in the drone motors produces a magnetic interference signal equal to the mechanical rotation frequency of the rotor (which is around 50 Hz). This strong signal sums up to the power grid signal at around the same 50 Hz frequency. The use of a high-frequency sampling magnetometer such as the MFAM-DK (1000 Hz) allowed us to correctly sample and identify the intense high-frequency interference around 50 Hz. This signal can be removed effectively with a simply designed low-pass filter. However, in the case of magnetometers with lower sampling rates the magnetic and electromagnetic noise would be under sampled and aliased in the ac quired magnetic data. This aliased signal may require additional filtering that may degrade the data quality. Moreover, Walter et al. (2021) shows that there might be other interferences at frequencies even higher than the MFAM-DK Nyquist frequency (500 Hz), although with amplitude from 1/10 to 1/80 of that of the 50 Hz signal, so that the importance of these potentially aliased components is probably negligible.

For navigation, we decided to use the drone GNSS receiver without equipping the platform with RTK system. Especially in mountain areas, the probability of losing the radio link with the base station during a flight is high. In these cases, corrections would not be transmitted to the GNSS drone system, and this would result in a decrease in accuracy from 3 to a few dozen of meters. The largest error will be in the flight elevation, and this could be very dangerous in the case of surveys over terrain with dense and high vegetation for the entire flight system, with the risk of losing the instrumentation. Instead, before the magnetic acquisition, a photogrammetry survey was conducted, and a Digital Surface Model (DSM) of the terrain was obtained. This terrain model was used to plan the flight route and to choose a safe acquisition elevation.

These technical features of the UAV survey allow to acquire high- quality data. The strong high frequency noise due to the small distance from the platform, was characterized by a spectral analysis and removed without affecting the geologic signal of interest, which occurs at a much lower frequency band.

The filtered data showed the presence of an intense linear magnetic anomaly. This anomaly, very well correlated to the outcropping part of the dike, suggests a NE-SW orientation of the main intrusive body in the uppermost part of the quarry. At about 150 m from the quarry wall, an intense elliptical magnetic anomaly, with its major axis perpendicular to the dike direction (in an NNW direction) is well correlated to exposed Strombolian pyroclastic deposits (Figure 4.2.1d) and welded spatter ramparts. This evidence may indicate this area to be the site of the vent system fed by the dike. Interestingly, the linear dike anomaly stops in correspondence with this intense anomaly, constraining the eastern dike-tip position and the location of the vent system. The forward modelling of the anomaly related to the dike was constrained by a field estimate of the total magnetization of the dike samples, which confirmed the high values expected from the intense magnetic anomalies. A profile where the dike is outcropping was used to further constrain the dike model, which resulted to have an inclination of about 80° and with a thickness of about 8.5 m. In the area of the elliptical anomaly, the outcropping volcanic products were modelled with a material having the same magnetization as the dike and a maximum thick-ness of 10–15 m.

4.2.6 Conclusions

In recent years the possibility of acquiring magnetic data from UAVs flying at very low altitude is gaining more and more success, with many studies proposing various measurement and flying solutions. One may wonder if these UAV systems really represent a useful innovation, or they are essentially replicating ground measurements results with a lower resolution. We think that the UAV magnetometry plays a primary role especially in difficult ground conditions (e.g., presence of dense vegetation, cultivated areas, swamps, glaciers, lakes, foreshore areas or steep mountain slopes). In this paper we presented a successful application of drone magnetometry that emphasizes its utility in conditions of inaccessibility of the investigated area.

We showed how a drone-borne magnetic dataset, acquired with a careful selection of parameters and after a simple processing, allowed an efficient mapping of an igneous dike intruded in sedimentary rocks, which was exposed by excavation activities in an active quarry, highlighting its direction and its eastern termination. Furthermore, it allowed the identification of a vent area with the presence of volcanic products. Therefore, in the presented case, we think that the drone magnetometry represents a unique tool for a fast and accurate identification of volcanic and sub-volcanic bodies across the entire mountain slope. We expect that in many other instances our strategy to set up the UAV magnetometry could represent an optimal solution for a cheap and fast exploration in fields such as volcanology, mining, or structural geology.

4.3 A drone-borne magnetic survey for the Irpinia Fault detection at Pantano di San Gregorio Magno.

4.3.1 Introduction

A good approach for the exploration is to conduct diverse array of geophysical surveys, using more than one investigation method.

In this study, a UAV magnetic survey was conducted as a complementary exploration method for the high-resolution geophysical investigation of the third segment surface rupture of the Irpinia Fault within the Pantano di San Gregorio Magno intramontane basin, located in the Southern Apennines region of Italy. A drone borne magnetic survey was performed to check if magnetic data could be useful to define the basement geometry or even the fault trace. This is one of the most seismically active structures in the Mediterranean region and is recently remembered for the 1980 Ms 6.9 earthquake which caused significant damage and loss of life. The project, aimed to study the area, is known with the acronym TESIRA (TEst Site IRpinia fAult) and received financial support by the University of Napoli Federico II. The project respond to the need to better evaluate the seismic hazard generated by young seismogenic faults. The studies of Improta et al. (2003); Bruno et al. (2010); Bruno et al. (2013) through 2D seismic surveys, showed the complex three-dimensional feature of this fault segment and called for a multivariate subsurface imaging techniques integration. The main geophysical acquisition method was a 3D high-resolution seismic, the first pilot study conducted over an active fault in mainland Italy with the goal to assess the near-surface structure, age, and kinematics of seismogenic faults. In addition to the seismic imaging, CO_2 soil degassing measurement, electric and microgravity surveys were done. The UAV magnetic data that we present here completed the goal to address a 3D high-resolution sub-surface data, taking part to the first multidisciplinary attempt of subsurface imaging for an active fault.

Considering the geologic context, we expect that a magnetization contrast may arise between the non-magnetic carbonate basement and the basin fill enriched by volcanic material or even in correspondence to a fault displacing the magnetized filling layers. The survey area presents a few houses or other structures (e.g., a solar panel array, channels and roads) that could produce intense magnetic fields.

4.3.2 Geological setting

The Quaternary intermontane tectono-karstic basin of Pantano di San Gregorio Magno is located in Southern Apennines, imposed to Mesozoic limestones and made of lacustrine deposits dated Upper Pleistocene - Holocene, which pass laterally and/or partially covered by Upper Pleistocene - Holocene debris coming from the carbonates slope (Aiello et al., 2006). Starting from the Middle Pleistocene, the range-bounding normal faults with a WNW-ESE trending opened and controlled the evolution of the depression. The works of Hippolyte et al., 1994; Montone 1997, and Caiazzo et al. (2006), showed a NE trending extension, still active.

Munno and Petrosino (2007), studied the tephra layers within lacustrine sediments, describing that the sedimentation started before 170,000 years ago at least up to 15,000 years ago, coincident with the Neapolitan Yellow Tuff eruption of Campi Flegrei. Petrosino et al. (2019) improved the study of the tephra layer started in Munno and Petrosino (2007). The author showed the core of 60 m drilled from the depocenter of San Gregorio Magno Basin (which not reached the bedrock) in which 21 tephra layers (Figure 4.3.1) were recognized and analyzed. The authors described the core as made of lacustrine sediments, mainly clays and silts, alternating with pyroclastic sandy layers. The tephra horizons present thickness from 5 to 80 cm with predominant sand-sized fractions

(Munno and Petrosino, 2007). These tephra layers are regularly distributed throughout the core body with a gap between 30 and 40 m depth.

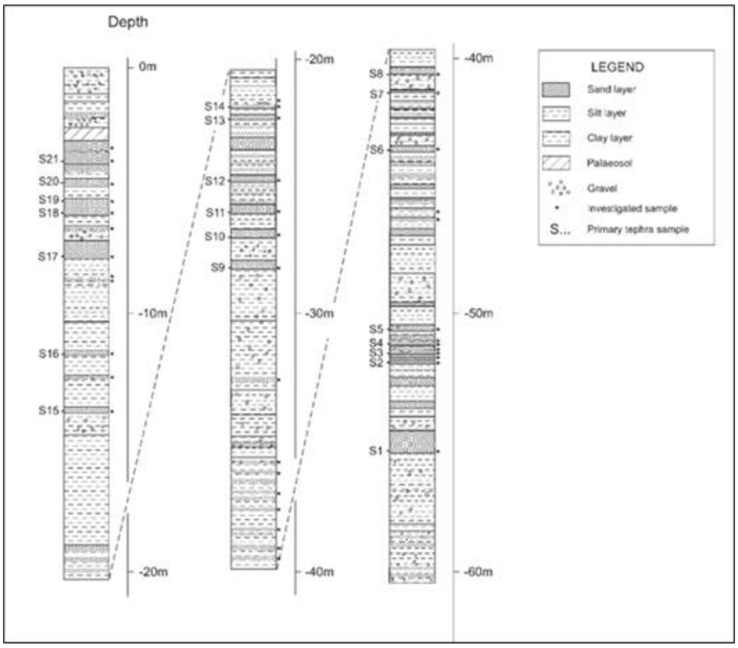

Figure 4.3.1. Stratigraphic sequence of the San Gregorio Magno basin drill hole after Munno and Petrosino (2007)

A precedent work of D'Addezio et al. (1991) described the recent stratigraphic sequence with direct information obtained through two excavated trenches which cross the scarp fragment of the Irpinia Fault running in the middle of the basin. The two trenches, 30 m long, 3.5 m wide, and 5/6 m deep, have a distance to each other of 35 m and were excavated perpendicular to the local trend of the scarp. Lithological and sedimentological characteristics allowed the authors to divide the stratigraphic sequence in seven main units (from A to G displayed in Figure 4.3.2) and for some of them several sub-layers were identified, ranging in age between 12,000 years ago and present.

Despite the presumed depth of the San Gregorio Magno basin being greater than 100 m, we lack information about the stratigraphic sequence at depths greater than 60 m, which is the length of the drilled core (Munno and Petrosino, 2007). As a result, there is a significant information gap regarding the tephra layers deeper than 60 m. Furthermore, the studies conducted by Munno and Petrosino (2007) and D'Addezio et al. (1991) did not provide useful information about the magnetic susceptibility of the tephra horizons. Totaro et al. (2022) used magnetic susceptibility measurements to correlate the tephra and cryptotephra of three cores located in the southern Adriatic Sea (offshore the Gargano promontory). They identified the distal counterparts of several explosive events by correlating the tephra detected in the three cores. Additionally, Totaro et al. (2022) integrated their results with those of previous studies, including San Gregorio Magno records. Two of the horizons identified in Munno and Petrosino (2007), the sample S21 representative of the Neapolitan Yellow Tuff, and the sample S20 related to the Greenish Pumice eruption, were also detected in the three cores analyzed by Totaro et al. (2022). Crocitti et al. (2009) conducted magnetic susceptibility measurements on tephrostratigraphic data from three cores drilled around southern Italy's coastline, which were then correlated with regional explosive eruption events. The age of the proximal deposits indicated by Crocitti et al. (2009) is younger than 12,000 years, making them comparable only with tephra horizons dated by D'Addezio et al. (1991). Following the sections of trenches 3 and 4, D'Addezio et al. (1991) dated units A (1,720 ± 90 years ago), B (2,570 ± 70 years ago), D2 (6,620 ± 90 years ago), D4 (9,420 ± 90 years ago), and E (11,180 ± 200 years ago). This time range is covered by the tephrostratigraphic data and the main activities of Vesuvius and Campi Flegrei indicated by Crocitti et al. (2009).

Therefore, susceptibility values cannot be attributed to each tephra layer for the San Gregorio Magno sequence, except for samples S21 and S20 (Figure 4.3.1). The pyroclastic material is diluted throughout the package of lacustrine sediments. However, thanks to the measurements by Totaro et al. (2022) and Crocitti et al. (2009) magnetic susceptibility values ranging between 10-500 x 10^{-5} SI can be hypothesized for the tephra layers in the S. Gregorio Magno basin.

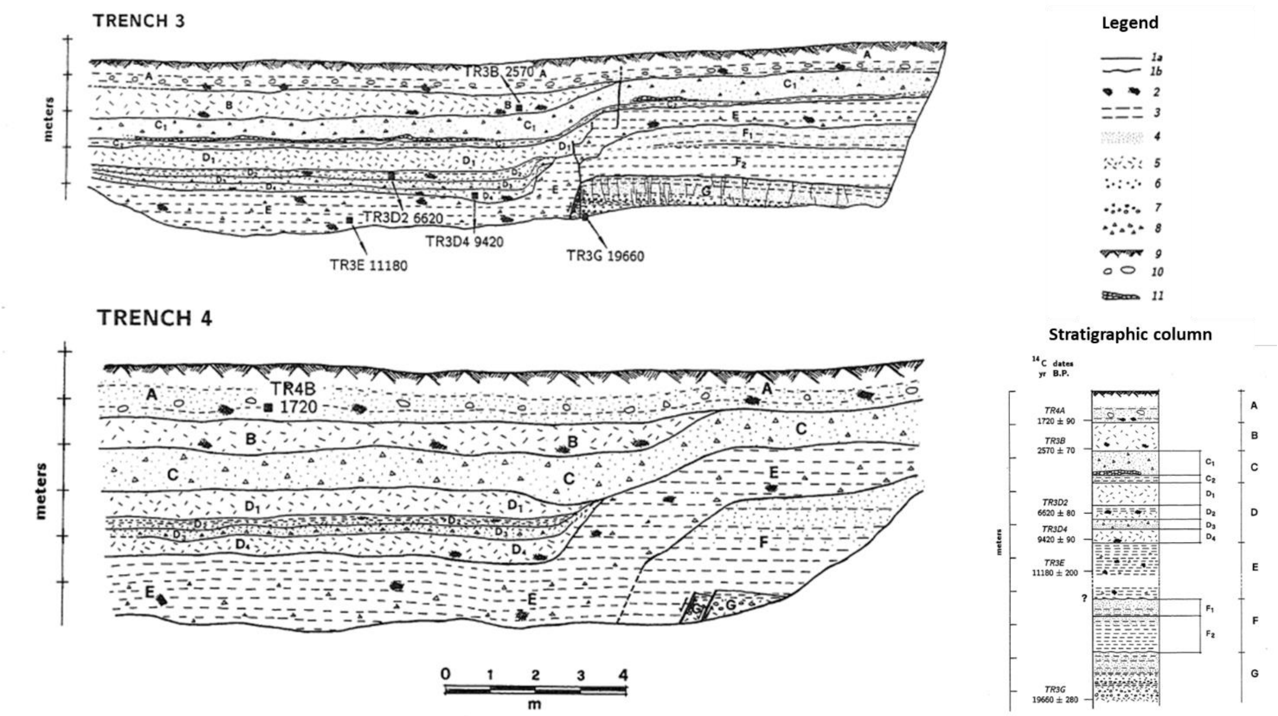

Figure 4.3.2. Sections of the trenches 3 and 4 modify after D'Addezio et al., 1991. Legend: 1a) conformable contact; 1b) angular or erosive disconformity; 2) organic substance; 3) clay; 4) silt; 5) colluvium; 6) sand; 7) pumices; 8) volcanic materials; 9) ground surface; 10) limestones pebbles; 11) conglomerate layer. The squares in black indicate the sample position collected for ^{14}C dating.

4.3.3 Measurements and survey design

The drone-borne magnetic surveys were conducted during the last two weeks of July 2023, mainly in the first hours of light and before the sunset considering the very hot temperature which could generates problems for the system in flight.

We used the MFAM in the "Development kit" version but arranged in a different flight configuration. The polystyrene cover and the Nomex honeycomb sandwich panel, which made the light, aereodynamic, and nonmagnetic custom bird, were maintained. However, considering the very weak magnetic response expected from the volcanic materials which fill the depression, the magnetic sensors were suspended 3 m below the UAV. The platform used for the acquisition was an electric-powered DJI Matrice M600 pro hexacopter and the total payload weight was less than 2.0 kg.

Seventeen individual flight surveys were needed to cover the study area at an elevation of 40 m AGL (above ground level), and 38 parallel survey lines spaced of 60 m with a speed of 2 m/s were flown (Figure 4.3.3). We used a DEM for the planning of the flight paths generated with photogrammetric data surveyed just before the magnetic acquisitions to ensure a constant acquisition altitude above the terrain. Despite the profiles were not acquired perfectly along a North–South direction, the sensors dead zones were avoided, and the magnetometer performance maximized. Flights were performed without a 180◦ turn at the end of each survey line to prevent the heading error problems. Overall, an area of about 1.5 km^2 was investigated. The acquired magnetic data were georeferenced using the UAV's GPS receiver.

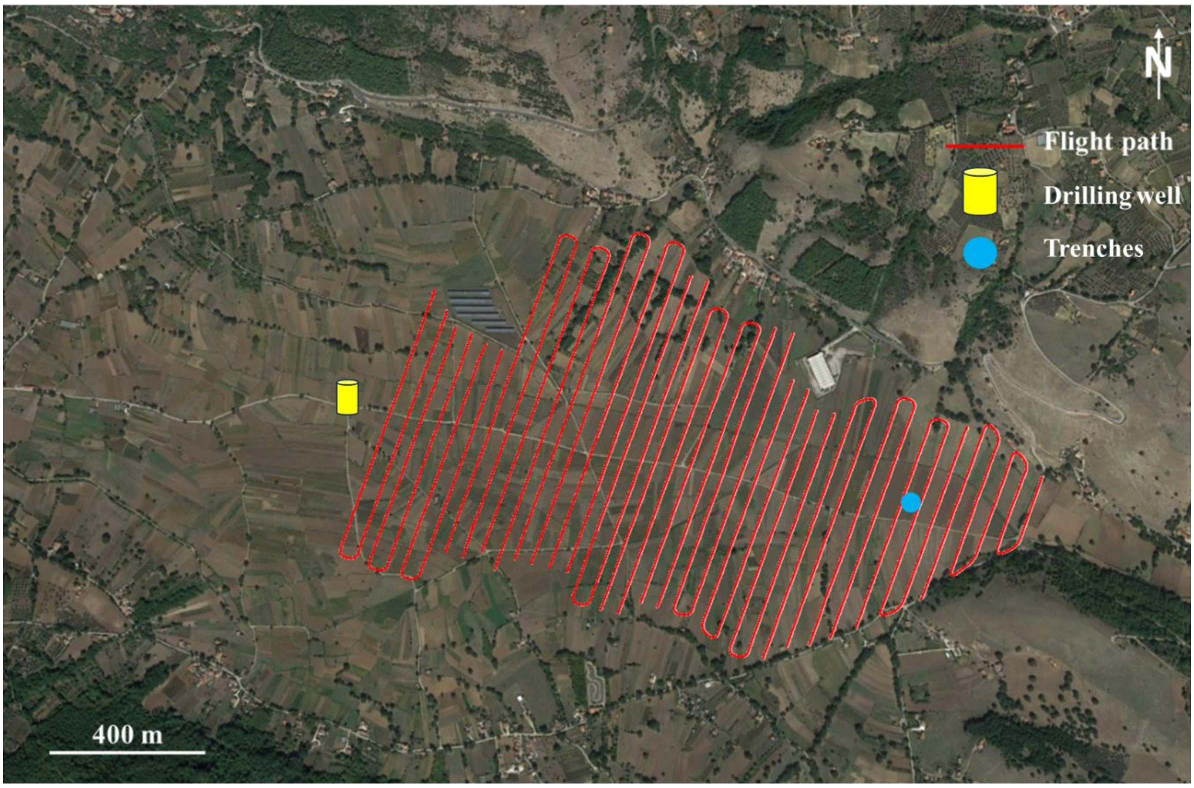

Figure 4.3.3. Flight paths of the UAV magnetic survey and position of the drilling well and trenches

4.3.4 Results, discussion and conclusions

The first step of the data analysis was the removal of the IGRF (a single constant value of 46,649.1 nT, as the area as a limited extension) and of the magnetic measurements collected at the end of each surveys lines where the drone turns. However, we needed to adjust for a constant of a few nT all the data collected in the flights conducted in the same day or in different days to compensate for the diurnal variation of the magnetic field.

We analyzed the spectral content of the acquired signal by performing a continuous wavelet transform in the time domain. The sum of the scalogram at each frequency for both sensors is shown in Figure 4.3.4. The most prominent spectral peak is around 50 Hz. This peak is due to the presence of alternate fields generated by the AC power lines present in the area and, to a lesser extent, due to the magnetic and electromagnetic fields generated by the UAV platform. At lower frequencies, the peaks at 0.45 Hz (with a very small amplitude) and 0.3 Hz could be instead associated with the oscillation of the MFAM, which is consistent with the tests described in Figure 3.5 and 3.6.

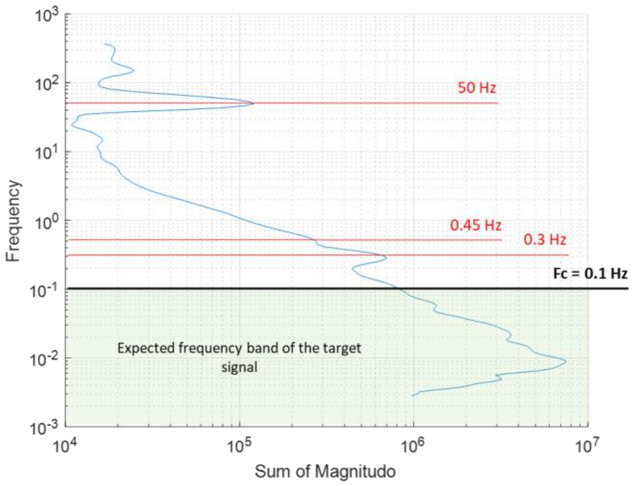

Figure 4.3.4 Sum of power of the scalogram for each frequency of data. The line is referred to the mean field value obtained from the first and second sensor signals. The red lines indicate the mean noise peaks: 1) 50 Hz relative to the power lines; 2) 0.45 Hz and 0.3 Hz are due to the oscillation of the system. The green area is associated to the target signal at frequencies lower than 0.1 Hz which will be used as the cut-off frequency for the low-pass filter.

Thus, we designed a Hanning-window low-pass filter in the time-domain with a cut-off frequency of 0.1 Hz, which removes the noise and preserves the lower frequency signal associated to the geological sources.

The filtered data collected along the 38 profiles were interpolated on a 15 m × 15 m grid to have a map of the magnetic anomalies in the area. However, due to the bi-directional flight mode, we compensated the heading error by subtracting the mean value of the magnetic field for each profile and by applying a directional filter based on the discrete wavelet transform DWT (Fedi et al., 1998; Fedi et al., 2003).

Figure 4.3.5 shows the filtered TFA map. It presents a maximum amplitude variation of about 40 nT, ranging from about − 20 to 20 nT. The northern part of the area is characterized by several anomalies with strong field amplitude values. However, all these features appear as the effect of modern buildings like houses and some solar panels (visible in the arial image of Google Earth of Figure 4.3.3). A second high magnetic feature, W-E trending, is present in the east side of the area and it results similar in amplitude with the ones just described. Moreover, looking the aerial photo, the anomaly follows a road that crosses the entire area investigated. For these reasons, it may be associated with human activity and not with a geological source. The TFA map also presents a random distribution of small circular anomalies which may correlate with the presence of some tractors since the area is constantly cultivated. Before a final interpretation can be made, additional flights are required to complete the entire basin with the aim of verify if a thinning of the sediments that fill the basin could be associated to total field magnetic gradients.

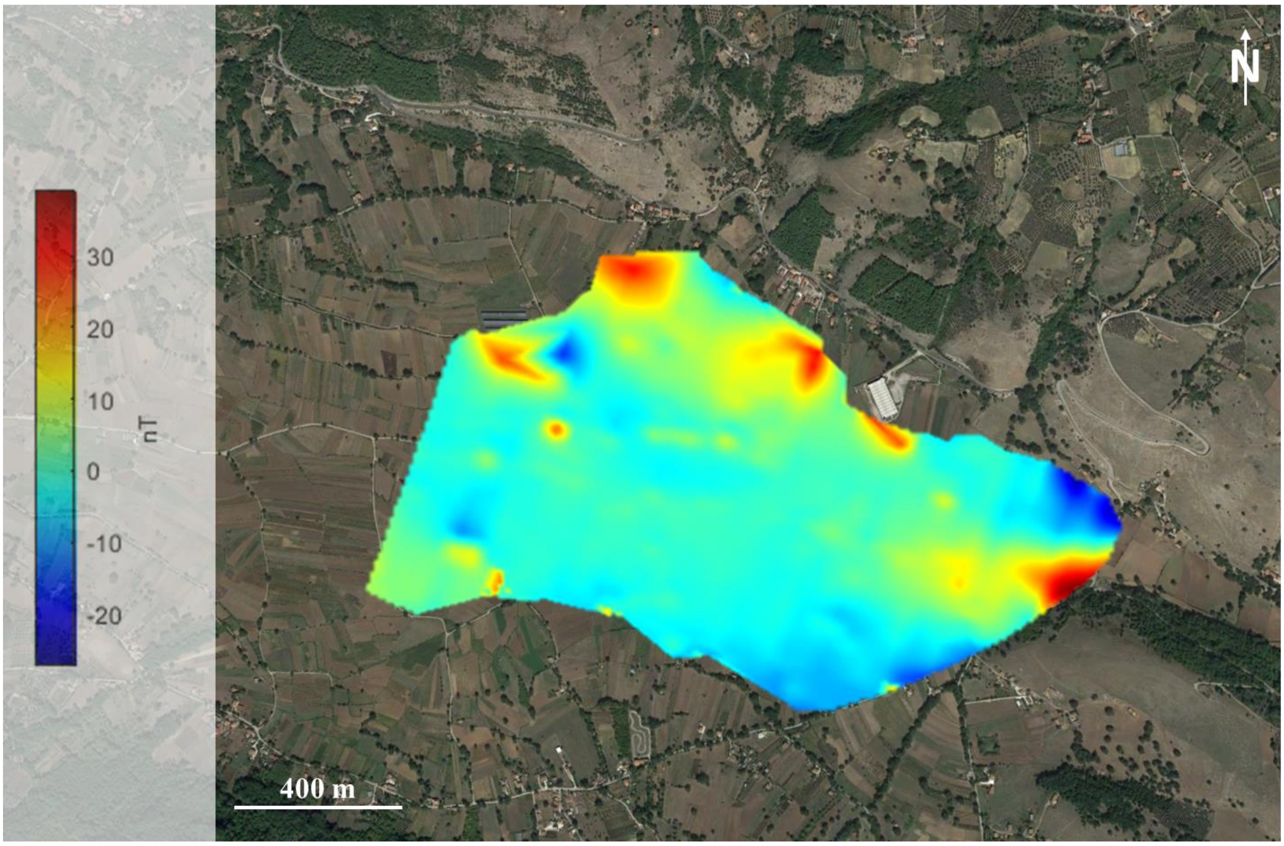

Figure 4.3.5 Total field magnetic anomalies superimposed on a satellite image of the survey area.

Chapter 4.3, 4.4, 4.5 and 4.6 have been omitted from the text as they are in submission phase.

Chapter 5 – Conclusion

In this final chapter, we outline the major conclusions of this thesis, which were established after a series of tests and applications of different interests. Chapter 1 introduced the main principles of the magnetic method and finished with a focus on the importance of magnetic gradiometry, which will be one of the main topics of our research. Chapter 2 presented a technical background on the main components (magnetometers and drones) of a UAV-borne aeromagnetic system and the main solutions found to resolve the key issues that could make the use of UAVs a reliable strategy for magnetic acquisition. Chapter 3 described the magnetometer used for our studies, how it was integrated into the UAVs, and useful tests for the flights. The body of Chapter 4 included the applications conducted during the three years of this thesis, presenting in detail the design and integration implemented for the characterization of targets of engineering, geological, and archaeological interest. Moreover, these studies suggest how to characterize and then minimize the magnetic interference of UAVs according to the flight solution and magnetic target.

UAVs and geophysical sensors, like magnetometers, will continue to advance at a fast pace. The tests and applications mentioned in this research improve the technical background concerning UAV magnetic surveys, revealing that for each specific target and survey, the UAV-sensor integration and processing workflow must be adjusted.

Below, we listed the major concluding points and recommendations obtained from each study:

- We designed a versatile, light, and non-magnetic custom bird for the MFAM to adjust depending on the targets.
- In the case of surveys over intense magnetic anomalies, the MFAM could be fixed directly to the drone landing gear to ensure more security and stability. This point was demonstrated in Chapter 4.1, where two flight configurations favoring the stability of the system during flight or the minimization of mobile platform noise (F0.5 and F3.0), showed similar results for magnetic data collected over buried metal pipelines. Careful processing can return high-quality drone-borne data using both flight configurations. The magnetic response was analogous to a ground magnetic dataset collected in the same area.
- The primary role of drone magnetometry is emphasized in Chapter 4.2, where the conditions of inaccessibility of the investigated area made the use of the drone the only investigation possibility. The presence of dense vegetation, cultivated areas, swamps, glaciers, lakes, foreshore areas, or steep mountain slopes are real examples where UAV magnetometry could represent a unique tool for fast and accurate acquisition. The conclusions made in the first point above allow mounting the MFAM directly to the aerial platform for the identification of volcanic and sub-volcanic bodies hosted in carbonate rock along a mountain slope.
- The use of a magnetometer operating at a fast acquisition rate (that in the case of the MFAM is 1000 Hz) is strongly advised to adequately sample the high frequencies associated to UAV magnetic and electromagnetic noise, typically represented by the 50 Hz or more.
- In case of weaker magnetic effects, the magnetometer needs to be maintained 3–5 m away from the UAV motors to avoid the magnetic and electromagnetic noise due to the drone and its engines. The interferences at frequencies even higher than the MFAM-DK Nyquist frequency (500 Hz) would be aliased in the acquired magnetic data degrading their quality.

The payload suspended below the UAV could compromise the stability of the flight and create unwanted periodic variations in the acquired magnetic data generated by the inevitable oscillations of the magnetometer sensors. In this thesis, we provided an additional contribution by characterizing the frequency spectral content of the swinging motion and finding solutions to remove it:

- We introduced a wooden frame under the custom MFAM bird and the drone landing gear to distance the rope anchor points further. This upgrade allowed us to minimize the swing of the system in flight, especially with respect to the yaw axis.

- The spectral analysis conducted on several tests revealed that the swinging motion is characterized by more than one frequency. External forces, like windy conditions, influence the attitude of the suspended payloads that is not constant along all the flight profiles. Therefore, we did not assume that the magnetometer predominantly acts as a pendulum.
- To avoid the swinging frequency contribution overlapping the expected target frequency band, the flight speed should be sufficiently slow as to favor a good spectral separation. Therefore, we used a low pass filter aimed at removing the noise due to oscillations and preserving the lowest frequency signals associated with the sources.

An important contribution of this research is the implementation, for the first time with the MFAM, of a vertical gradient configuration. Thanks to the availability of the Development kit version, we designed new magnetometer custom birds to distance the sensors of 0.25 m and 1 m. We conducted several UAV magnetic surveys for archaeological purpose. The following is a list of the main conclusions resulting from these applications:

- For the first time with the MFAM, a vertical gradient configuration was implemented both for ground and UAV surveys.
- A baseline of 0.25 m was tested and worked well both for ground and UAVs surveys.
- A distance between the sensors of 1 m, useful for deeper targets or acquisitions at higher altitude, was successfully tested only for ground surveys.
- Considering the MFAM arranged in a vertical gradient configuration, the distance of the sensors from the UAVs will be different even with a baseline of 0.25 cm. However, the spectral analysis revealed that the peaks due to the swinging motion are at the same frequencies for both sensors.

There are final considerations to be done concerning the common features of noise. To compensate them, we suggest practical logistic aspects to take into account before a flight and processing steps:

- We suggest programming the survey lines along a direction approximately North–South and maintaining one constant heading throughout the entire survey.
- The second benefit of maintaining one constant heading throughout the entire survey, without performing the 180◦ turn at the end of each line, is the minimization of the heading error. This procedure is simply implemented using flight programming software. The best way to prevent the heading error is to not acquire in a bi-directional mode but it would cause a slowdown in the data acquisition both for ground and UAV surveys. Therefore, it may happen that some directional noise still effects the result and, in this case, could be necessary use a directional filtering after the removal from each profile of field mean value.
- Most geophysical methods, like the magnetic one, are extremely sensitive to the altitude above the investigation target. The use of a DEM or a laser/radar altimeter, which allow to follow the correct terrain topography, guarantees the requested resolution for the magnetic investigations.

References

Accomando, F., Vitale, A., Bonfante, A., Buonanno, M., & Florio, G. (2021). Performance of two different flight configurations for drone-borne magnetic data. *Sensors*, *21*(17), 5736. https://doi.org/10.3390/s21175736.

Accomando, F., Bonfante, A., Buonanno, M., Natale, J., Vitale, S., & Florio, G. (2023). The drone-borne magnetic survey as the optimal strategy for high-resolution investigations in presence of extremely rough terrains: The case study of the Taverna San Felice quarry dike. *Journal of Applied Geophysics*, *217*, 105186.

Anderson, D., & Pita, A. (2005). Geophysical surveying with georanger uav. In *Infotech@ Aerospace* (p. 6952). https://doi.org/10.2514/6.2005-6952

Aiello, G., Ascione, A., Barra, D., Munno, R., Petrosino, P., Ermolli, E. R., & Villani, F. (2007). Evolution of the late Quaternary San Gregorio Magno tectono-karstic basin (southern Italy) inferred from geomorphological, tephrostratigraphical and palaeoecological analyses: tectonic implications. *Journal of Quaternary Science*, *22*(3), 233-245.

Barnard, J. The use of unmanned aircraft in oil, gas and mineral exploration and production activities. In Proceedings of the 23rd Bristol International UAV Systems Conference 2008, Bristol, UK, 7–9 April 2008.

Blakely, R. J.(1996). Potential theory in gravity and magnetic applications: Cambridge University Press, Cambridge.

Breiner, S. (1973). *Applications manual for portable magnetometers* (Vol. 395). Sunnyvale, California: Geometrics.

Bruno, P. P., Castiello, A., & Improta, L. (2010). Ultrashallow seismic imaging of the causative fault of the 1980, M6. 9, southern Italy earthquake by pre-stack depth migration of dense wide-aperture data. *Geophysical Research Letters*, *37*(19).doi:10.1029/2010GL044721.

Bruno, P. P., Castiello, A., Villani, F., & Improta, L. (2013). High-resolution densely spaced wide-aperture seismic profiling as a tool to aid seismic hazard assessment of fault-bounded intramontane basins: application to Vallo Di Diano, Southern Italy. *Bulletin of the Seismological Society of America*, *103*(3), 1969-1980.

Budker, D., and Kimball, D. F. J. (2013). Optical Magnetometry, Cambridge University Press, Cambridge, UK, pp. 1-405.

Campbell, W. H. (2003). *Introduction to geomagnetic fields*. Cambridge University Press.Conticelli, S., Marchionni, S., Rosa, D., Giordano, G., Boari, E., & Avanzinelli, R. (2009). Shoshonite and sub-alkaline magmas from an ultrapotassic volcano: Sr–Nd–Pb isotope data on the Roccamonfina volcanic rocks, Roman Magmatic Province, Southern Italy. *Contributions to Mineralogy and Petrology*, *157*, 41-63.

CANCELLIERE, S., & LAZZARINI, L. (2019). Le calcareniti mediterranee, con particolare riferimento a quelle della Magna Grecia, e un esempio di studio: le Tavole Palatine The Mediterranean Calcarenites, with particular reference to Magna Graecia, a case study: the Tavole Palatine. Segni, Immagini e Storia dei centri costieri euro-mediterranei, 4, 27.

Cao, W., Qing, H., Xu, X., Liu, C., Chen, S., Zhong, Y., ... & Liu, Q. (2022). Pre-Archaeological Investigation by Integrating Unmanned Aerial Vehicle Aeromagnetic Surveys and Soil Analyses. *Drones*, *6*(9), 243. **https://doi.org/10.3390/drones6090243**

Coyle, M., Dumont, R., Keating, P., Kiss, F., & Miles, W. (2014). Geological Survey of Canada aeromagnetic surveys: Design, quality assurance, and data dissemination.

Crocitti, M. A. R. C. O., Sulpizio, R., Insinga, D. D., De Rosa, R., Donato, P., Iorio, M., ... & Lubritto, C. (2019). On ash dispersal from moderately explosive volcanic eruptions: Examples from Holocene and Late Pleistocene eruptions of Italian volcanoes. Journal of Volcanology and Geothermal Research, 385, 198-221. https://doi.org/10.1016/j.jvolgeores.2018.07.009

Cunningham, M. (2016). *Aeromagnetic surveying with unmanned aircraft systems* (Doctoral dissertation, Carleton University).

Cunningham, M., Samson, C., Wood, A., & Cook, I. (2018). Aeromagnetic surveying with a rotary-wing unmanned aircraft system: A case study from a zinc deposit in Nash Creek, New Brunswick, Canada. *Pure and Applied Geophysics*, *175*, 3145-3158.

Cunningham, M., Samson, C., Laliberté, J., Goldie, M., Wood, A., & Birkett, D. (2021). Inversion of magnetic data acquired with a rotary-wing unmanned aircraft system for gold exploration. *Pure and Applied Geophysics*, *178*, 501-516.

d'Addezio, G., Pantosti, D., & Valensise, G. (1991). Paleoearthquakes along the Irpinia fault at Pantano di San Gregorio Magno (southern Italy). *Il Quaternario*, *4*(1a), 121-136.

De Rita, D., & Giordano, G. (1996). Volcanological and structural evolution of Roccamonfina volcano (Italy): origin of the summit caldera. *Geological Society, London, Special Publications*, *110*(1), 209-224.

de Lépinay, J. M., Fréville, T., Gavazzi, B., Kiemes, B., Sanabria, L. M., Munschy, M., & Reiller, H. (2021). A versatile solution for high-quality UAV fluxgate magnetic acquisitions. *First Break*, *39*(8), 57-62. DOI: 10.3997/1365-2397.fb2021061.

de Smet, T. S., Nikulin, A., Romanzo, N., Graber, N., Dietrich, C., & Puliaiev, A. (2021). Successful application of drone-based aeromagnetic surveys to locate legacy oil and gas wells in Cattaraugus county, New York. *Journal of Applied Geophysics*, *186*, 104250.https:// doi.org/10.1016/j.jappgeo.2020.104250.

Døssing, A., Lima Simoes da Silva, E., Martelet, G., Maack Rasmussen, T., Gloaguen, E., Thejll Petersen, J., & Linde, J. (2021). A high-speed, light-weight scalar magnetometer bird for km scale UAV magnetic surveying: On sensor choice, bird design, and quality of output data. *Remote Sensing*, *13*(4), 649. DOI:10.3390/rs13040649

Dual MagS ystem. Available online: http://www.mgt-geo.com/dual%20mag%20system.htm (accessed on 22 July 2021).

Eck, C., & Imbach, B. (2012). Aerial magnetic sensing with an UAV helicopter. *The International Archives of the Photogrammetry, Remote Sensing and Spatial Information Sciences*, *38*, 81-85.Fedi, M., & Quarta, T. (1998). Wavelet analysis for the regional-residual and local separation of potential field anomalies [Link]. *Geophysical prospecting*, *46*(5), 507-525.

Fedi M, Florio G (2003) Decorrugation and removal of directional trends of magnetic fields by the wavelet transform: application to archeological areas. Geophys Prospect 51(4):261–272

Fedi, M., Cella, F., Florio, G., Manna, M. L., & Paoletti, V. (2017). Geomagnetometry for archaeology. *Sensing the Past: From artifact to historical site*, 203-230.Florio, G., Fedi, M., & Pašteka, R.

(2014). On the estimation of the structural index from low-pass filtered magnetic data. *Geophysics*, *79*(6), J67-J80.

Fixed Wing MagSystem. Available online: http://www.mgt-geo.com/fixed%20wing%20mag.htm (accessed on 21 July 2021).

Funaki, M., Higashino, S. I., Sakanaka, S., Iwata, N., Nakamura, N., Hirasawa, N., ... & Kuwabara, M. (2014). Small unmanned aerial vehicles for aeromagnetic surveys and their flights in the South Shetland Islands, Antarctica. *Polar Science*, *8*(4), 342-356. DOI: 10.1016/j.polar.2014.07.001.

Gavazzi, B., Le Maire, P., Munschy, M., & Dechamp, A. (2016). Fluxgate vector magnetometers: A multisensor device for ground, UAV, and airborne magnetic surveys. *The Leading Edge*, *35*(9), 795-797. DOI:10.1190/tle35090795.1

Gavazzi, B., Le Maire, P., de Lépinay, J. M., Calou, P., & Munschy, M. (2019). Fluxgate three-component magnetometers for cost-effective ground, UAV and airborne magnetic surveys for industrial and academic geoscience applications and comparison with current industrial standards through case studies. *Geomechanics for Energy and the Environment*, *20*, 100117. DOI: 10.1016/j.gete.2019.03.002.

Gee, J. S., Cande, S. C., Kent, D. V., Partner, R., & Heckman, K. (2008). Mapping geomagnetic field variations with unmanned airborne vehicles. *Eos, Transactions American Geophysical Union*, *89*(19), 178-179. https://doi.org/10.1029/2008EO190002

Ge, J., Li, H., Luo, W., Dong, H., Liu, H., Wang, H., ... & Zhang, H. (2019). Aeromagnetic system for a Multi-rotor unmanned aerial vehicle based on the Overhauser sensor. *Journal of Instrumentation*, *14*(01), P01015. DOI: 10.1088/1748-0221/14/01/P01015.

GIROLAMO, P. D., MELLUSO, L., & Morra, V. (1991). Magmatic activity northeast of Roccamonfina volcano (Southern Italy):. Petrology, geochemistry and relationships with campanian volcanics. *Neues Jahrbuch für Mineralogie. Abhandlungen*, *163*, 271-289.

Glen, J. M., Egger, A. E., Ippolito, C., & Athens, N. (2013, February). Correlation of geothermal springs with sub-surface fault terminations revealed by high-resolution, UAV-acquired magnetic data. In *Proceedings of the 38th Workshop on Geothermal Reservoir Engineering: Stanford Geothermal Program Workshop Report SGP-TR-198* (pp. 1233-1242).

Goussev S. (2022). Gravity and Magnetic Encyclopedic Dictionary. Society of Exploration Geophysicists, 362 pages.

Hashimoto, T., Koyama, T., Kaneko, T., Ohminato, T., Yanagisawa, T., Yoshimoto, M., & Suzuki, E. (2014). Aeromagnetic survey using an unmanned autonomous helicopter over Tarumae Volcano, northern Japan. *Exploration Geophysics*, *45*(1), 37-42.

Hinze, W. J., Von Frese, R. R., Von Frese, R., & Saad, A. H. (2013). *Gravity and magnetic exploration: Principles, practices, and applications*. Cambridge University Press.

Hood, P. J., & Teskey, D. J. (1989). Aeromagnetic gradiometer program of the Geological Survey of Canada. *Geophysics*, *54*(8), 1012-1022.

Hovde, D., Prouty, M., Hrvoic, I., and Slocum, R, 2013, Optical Magnetometry - 20 Commercial magnetometers and their application, Cambridge University Press, Cambridge, UK, pp. 387-405.

Improta, L., Zollo, A., Bruno, P. P., Herrero, A., & Villani, F. (2003). High-resolution seismic tomography across the 1980 (Ms 6.9) Southern Italy earthquake fault scarp. *Geophysical research letters*, *30*(10).doi:10.1029/2003GL017077.

Jackisch, R., Madriz, Y., Zimmermann, R., Pirttijärvi, M., Saartenoja, A., Heincke, B. H., ... & Gloaguen, R. (2019). Drone-borne hyperspectral and magnetic data integration: Otanmäki Fe-Ti-V deposit in Finland. *Remote sensing*, *11*(18), 2084. DOI: https://doi.org/10.3390/rs11182084

Jackisch, R., Lorenz, S., Kirsch, M., Zimmermann, R., Tusa, L., Pirttijärvi, M., ... & Gloaguen, R. (2020). Integrated geological and geophysical mapping of a carbonatite-hosting outcrop in siilinjärvi, finland, using unmanned aerial systems. *Remote Sensing*, *12*(18), 2998.

Kearey, P., Brooks, M., & Hill, I. (2002). *An introduction to geophysical exploration* (Vol. 4). John Wiley & Sons. **https://doi.org/10.3390/rs12182998**

Jiang, D., Zeng, Z., Zhou, S., Guan, Y., & Lin, T. (2020). Integration of an aeromagnetic measurement system based on an unmanned aerial vehicle platform and its application in the exploration of the Ma'anshan magnetite deposit. *IEEE Access*, *8*, 189576-189586. Doi:10.1109/ACCESS.2020.3031395

Josephson, B. D., 1962, Possible new effect in superconductive tunnelling, Physics Letters, 1, no. 7, pp. 251-253. DOI: 10.1016/0031-9163(62)91369-0

Josephson, B. D., 1974, The discovery of tunnelling supercurrents, Reviews of Modern Physics, 46, no. 2, pp. 251-254. DOI:10.1103/REVMODPHYS.46.251

JU, X., NIU, H. B., GUO, H., HAN, S., WANG, Y. Z., LÜ, C., & ZHENG, Q. (2020). Safety analysis and quality evaluation of the aeromagnetic measurement system of CH-4 UAV. *Progress in Geophysics*, *35*(4), 1565-1571. DOI: 10.6038/pg2020EE0004

Kaub, L., Keller, G., Bouligand, C., & Glen, J. M. (2021). Magnetic surveys with Unmanned Aerial Systems: Software for assessing and comparing the accuracy of different sensor systems, suspension designs and compensation methods. *Geochemistry, Geophysics, Geosystems*, *22*(7), e2021GC009745. DOI: 10.1029/2021GC009745

Klüwer, L. D. (1823). Norske Mindesmærker, aftegnede paa en Reise igjennem en Deel af det Nordenfjeldske. Hvüd.

Kolster, M. E., Wigh, M. D., Lima Simões da Silva, E., Bjerg Vilhelmsen, T., & Døssing, A. (2022). High-speed magnetic surveying for unexploded ordnance using UAV systems. *Remote Sensing*, *14*(5), 1134. **https://doi.org/10.3390/rs14051134**

Koyama, T., Kaneko, T., Ohminato, T., Yanagisawa, T., Watanabe, A., & Takeo, M. (2013). An aeromagnetic survey of Shinmoe-dake volcano, Kirishima, Japan, after the 2011 eruption using an unmanned autonomous helicopter. *Earth, Planets and Space*, *65*(6), 657-666.

Lanza, R., & Meloni, A. (2009). The earth's magnetism: an introduction for geologists. *(No Title)*.

Le Maire, P., Bertrand, L., Munschy, M., Diraison, M., & Géraud, Y. (2020). Aerial magnetic mapping with an unmanned aerial vehicle and a fluxgate magnetometer: A new method for rapid mapping and upscaling from the field to regional scale. *Geophysical prospecting*, *68*(7), 2307-2319. DOI: https://doi.org/10.1111/1365-2478.12991

Le Maire, P., Martelet, G., Billy, J., Bernon, N., Nuns, S., & Thieblemont, D. (2023, June). Magnetic surveying with UAV to fill the gap between ground and airborne magnetic surveys. In *84th EAGE Annual Conference & Exhibition* (Vol. 2023, No. 1, pp. 1-5). European Association of Geoscientists & Engineers.

Leliak, P. (1961). Identification and evaluation of magnetic-field sources of magnetic airborne detector equipped aircraft. IRE Transactions on Aerospace and Navigational Electronics, (3), 95-105. 10.1109/TANE3.1961.4201799

Lee, M., Madriz, Y., Gloaguen, R., & McEnroe, S. (2023). UAV magnetics over the Bjerkreim-Sokndal Intrusion, Rogaland, Norway: A first look. *The Leading Edge*, *42*(2), 90-97. https://doi.org/10.1190/tle42020090.1

Li, W. J., Qin, X. W., & Gan, X. P. (2014, September). The IGGE UAV aero magnetic and radiometric survey system. In *Near Surface Geoscience 2014-20th European Meeting of Environmental and Engineering Geophysics* (Vol. 2014, No. 1, pp. 1-5). European Association of Geoscientists & Engineers. **DOI:** https://doi.org/10.3997/2214-4609.20141981

LI, Z., GAO, S., & WANG, X. (2018). New method of aeromagnetic surveys with rotorcraft UAV in particular areas. *Chinese Journal of Geophysics*, *61*(9), 3825-3834.

Li, H., Ge, J., Dong, H., Qiu, X., Luo, W., Liu, H., ... & Zhang, H. (2018, July). Aeromagnetic compensation of rotor UAV based on least squares. In *2018 37th Chinese Control Conference (CCC)* (pp. 10248-10253). IEEE. https://doi.org/10.23919/ChiCC.2018.8483068.

Luoma, S., & Zhou, X. (2020). Construction of a fluxgate magnetic gradiometer for integration with an unmanned aircraft system. *Remote Sensing*, *12*(16), 2551. DOI: https://doi.org/10.3390/rs12162551

Macharet, D. G., Perez-Imaz, H. I., Rezeck, P. A., Potje, G. A., Benyosef, L. C., Wiermann, A., ... & Campos, M. F. (2016). Autonomous aeromagnetic surveys using a fluxgate magnetometer. *Sensors*, *16*(12), 2169. DOI: https://doi.org/10.3390/s16122169

Malehmir, A., Dynesius, L., Paulusson, K., Paulusson, A., Johansson, H., Bastani, M., ... & Marsden, P. (2017). The potential of rotary-wing UAV-based magnetic surveys for mineral exploration: A case study from central Sweden. *The Leading Edge*, *36*(7), 552-557. DOI: 10.1190/tle36070552.1.

McKay, M. D., & Anderson, M. O. (2011). *Development of Autonomous Magnetometer Rotorcraft for Wide Area Assessment* (No. INL/CON-11-22005). Idaho National Lab.(INL), Idaho Falls, ID (United States).

Mu, Y., Zhang, X., Xie, W., & Zheng, Y. (2020). Automatic detection of near-surface targets for unmanned aerial vehicle (UAV) magnetic survey. *Remote Sensing*, *12*(3), 452. DOI: 10.3390/rs12030452.

Naprstek, T., & Lee, M. D. (2017, December). Aeromagnetic compensation for UAVs. In AGU Fall Meeting Abstracts (Vol. 2017, pp. NS31A-0005).

Natale, J., Vitale, S., Giordano, G., Fedele, L., Lucci, F., Vona, A., ... & Ciarcia, S. (2023). The Taverna San Felice Dike (NE of Roccamonfina Volcano): Unraveling Magmatic Intrusion Processes and Volcano-Tectonics in the Tyrrhenian Margin of the Southern Apennines. *Geochemistry, Geophysics, Geosystems*, *24*(8), e2023GC010994.

Nikulin, A., & de Smet, T. S. (2019). A UAV-based magnetic survey method to detect and identify orphaned oil and gas wells. *The Leading Edge*, *38*(6), 447-452. https://doi.org/10.1190/tle38060447.1

Nikulin, P. D., deSmet, P. D., Puliaiev, A., Zhurakhov, V., Fasullo, S., Chen, G., ... & Cappuccio, K. (2020). Automated UAS aeromagnetic surveys to detect MBRL unexploded ordnance. *The Journal of Conventional Weapons Destruction*, *24*(1), 13.

Noriega, G., & Marszalkowski, A. (2017). Adaptive techniques and other recent developments in aeromagnetic compensation. *First Break*, *35*(9).

Packard, M., and Varian, R., 1954, Proton gyromagnetic ratio, Physical Reviews, 93, pp. 941

Paoletti, V., Fedi, M., Florio, G., & Rapolla, A. (2007). Localized cultural denoising of high-resolution aeromagnetic data. *Geophysical Prospecting*, *55*(3), 421-432.

Parshin, A. V., Morozov, V. A., Blinov, A. V., Kosterev, A. N., & Budyak, A. E. (2018). Low-altitude geophysical magnetic prospecting based on multirotor UAV as a promising replacement for traditional ground survey. *Geo-spatial information science*, *21*(1), 67-74.doi: 10.1080/10095020.2017.1420508.

Parshin, A., Gatilov, M., Davidenko, Y., Bashkeev, A., Snegirev, N., & Milgunov, A. (2022, September). Using the “triad” of UAV-TEM, UAV-magnetic prospecting and UAV-gamma-spectrometry: Case of prospecting for blind ore deposits. In *Proceedings of the NSG2022 3rd Conference on Airborne, Drone and Robotic Geophysics, Belgrade, Serbia* (pp. 18-22).

Parvar, K. (2016). *Development and evaluation of unmanned aerial vehicle (UAV) magnetometry systems* (Doctoral dissertation, Queen's University (Canada)).

Parvar, K., Braun, A., Layton-Matthews, D., & Burns, M. (2017). UAV magnetometry for chromite exploration in the Samail ophiolite sequence, Oman. *Journal of Unmanned Vehicle Systems*, *6*(1), 57-69. https://doi.org/10.1139/juvs-2017-0015

Pei, Y., Liu, B., Hua, Q., Liu, C., & Ji, Y. (2017). An aeromagnetic survey system based on an unmanned autonomous helicopter: Development, experiment, and analysis. *International Journal of Remote Sensing*, *38*(8-10), 3068-3083. https://doi.org/10.1080/01431161.2016.1274448

Petersen, T.H. 1927. “Ekne, Gustad I Skogn Prestegjeld”. Letter in the topographical archives of The Museum of Archaeology and Natural History in Trondheim. Document number 000572.

Petzke, M., Hofmeister, P., Hördt, A., Glaßmeier, K. H., & Auster, H. U. (2013, September). Aeromagnetics with an unmanned airship. In *Near Surface Geoscience 2013-19th EAGE European Meeting of Environmental and Engineering Geophysics* (pp. cp-354). European Association of Geoscientists & Engineers.

Phelps, G., Bracken, R., Spritzer, J., & White, D. (2022). Achieving sub-nanoTesla precision in multirotor UAV aeromagnetic surveys. *Journal of Applied Geophysics*, *206*, 104779.https://doi.org/10.1016/j.jappgeo.2022.104779.

Ranalli, G. (1995). Rheology of the Earth, Second Edition. London: Chapman & Hall.

Pisciotta, A., Vitale, G., Scudero, S., Martorana, R., Capizzi, P., & D’Alessandro, A. (2021). A lightweight prototype of a magnetometric system for unmanned aerial vehicles. *Sensors*, *21*(14), 4691. DOI:https://doi.org/10.3390/s21144691.

Poliachenko, I., Kozak, V., Bakhmutov, V., Cherkes, S., & Varava, I. (2023). Preliminary results of UAV magnetic surveys for unexploded ordnance de-tection in Ukraine: effectiveness and challenges. *Geofizicheskiy Zhurnal*, *45*(5). DOI: https://doi.org/10.24028/gj.v45i5.289117

QIAO, Z., MA, G., ZHOU, W., YU, P., ZHOU, S., WANG, T., ... & ZHANG, Z. (2020). Research on the comprehensive compensation of aeromagnetic system error of multi-rotor UAV. *Chinese Journal of Geophysics*, *63*(12), 4604-4612.

Reeves, C. (2005). Aeromagnetic Surveys Principles, Practice & Interpretation. An online book Published by Geosoft

Reid, A. B., Allsop, J. M., Granser, H., Millett, A. T., & Somerton, I. W. (1990). Magnetic interpretation in three dimensions using Euler deconvolution. *Geophysics*, *55*(1), 80-91.

Reynolds, R. L. (1977). *Magnetic titanohematite minerals in uranium-bearing sandstones* (Vol. 77). Reston, VA, USA: US Geological Survey.

Roest, W. R., Verhoef, J., & Pilkington, M. (1992). Magnetic interpretation using the 3-D analytic signal. *Geophysics*, *57*(1), 116-125.

Samson, C., Straznicky, P., Laliberté, J., Caron, R., Ferguson, S., & Archer, R. (2010, October). Designing and building an unmanned aircraft system for aeromagnetic surveying. In *SEG International Exposition and Annual Meeting* (pp. SEG-2010). SEG.

Schmidt, P., Clark, D., Leslie, K., Bick, M., Tilbrook, D., & Foley, C. (2004). GETMAG? a SQUID magnetic tensor gradiometer for mineral and oil exploration. Exploration Geophysics, 35(4), 297-305.

Schmidt, P. W., & Clark, D. A. (2006). The magnetic gradient tensor: Its properties and uses in source characterization. The Leading Edge, 25(1), 75-78.

Schmidt, V., Becken, M., and Schmalzl, J. A., 2020, UAV-borne magnetic survey for archaeological prospection of a Celtic burial site, First Break, 38, no. 8, pp. 61-66. DOI: 10.3997/1365 2397.fb2020061

Schmidt, V., & Coolen, J. (2021). Potential and Challenges of UAV-Borne Magnetic Measurements for Archaeological Prospection. *ArcheoSciences*, *45*, 207-209.

Skillman, T. L., & Bender, P. L. (1958). Measurement of the earth's magnetic field with a rubidium vapor magnetometer. Journal of Geophysical Research, 63(3), 513-515.

Single Mag System. Available online: http://www.mgt-geo.com/single%20mag%20system.htm (accessed on 22 July 2021).

Sivertsen, M. 1965. Skogns historie band III. Om Skognområdet i førhistorisk tid. Published by ”Nembda for Skogn Historie”. Levanger. Verdal Boktrykkeri.

Slack, H., Lynch, V. M., & Langan, L. (1967). The geomagnetic gradiometer. Geophysics, 32(5), 877-892.

Solberg, B. (2000). Jernalderen i Norge: ca. 500 f. Kr.-1030 e. Kr. *(No Title)*.

Sowerbutts, W. T. C. (1988). The use of geophysical methods to locate joints in underground metal pipelines. *Quarterly Journal of Engineering Geology and Hydrogeology*, *21*(3), 273-281.

Stamnes, A. A. (2008). Jernalderens jordbruksbosetning i Nord-Trøndelag. Utvikling og testing av en prediktiv modell. *Unpublished master thesis, Norwegian University of Science and Technology, Trondheim*.

Stamnes, A. A. (2010). Developing a Sequential Geophysical Survey Design for Norwegian Iron Age Settlements. *MSc. Division of Archaeological, Geophysical and Environmental Sciences. University of Bradford. Bradford*.

Stele, A., Linck, R., Schikorra, M., & Fassbinder, J. W. (2022). UAV magnetometer survey in low-level flight for archaeology: Case study of a Second World War airfield at Ganacker (Lower Bavaria, Germany). *Archaeological Prospection*, *29*(4), 645-650. DOI:10.1002/arp.1877.

Stoll, J., & Moritz, D. (2013, June). Unmanned aircraft systems for rapid near surface geophysical measurements. In *75th EAGE Conference & Exhibition-Workshops* (pp. cp-349). European Association of Geoscientists & Engineers. Cunningham, M.; Samson, C.; Wood, A.; Cook, I.; Doyle, B. Detecting mineral ore bodies with UASs instrumented with magnetometers. In Proceedings of the Unmanned Systems Canada Conference, Halifax, NS, Canada, 2–5 November 2015.

Stolz, R., Zakosarenko, V., Schulz, M., Chwala, A., Fritzsch, L., Meyer, H. G., & Köstlin, E. O. (2006). Magnetic full-tensor SQUID gradiometer system for geophysical applications. *The Leading Edge*, *25*(2), 178-180.

Talwani, M. (1964). Computation of magnetic anomalies caused by two dimensional structures of arbitary shape. *Computers in the mineral industries*, *1*, 464-480.Won, I. J., and Bevis, M., Computing the gravitational and magnetic anomalies due to a polygon: Algorithms and Fortran subroutines: Geophysics, 52, 232-238, 1987.

Taylor, H. A., 1989, Fairey Aircraft since 1915, Naval Institute Press, Reprint edition. pp. 450. ISBN-10: 0870212087

Teskey, D. J., Barlow, R., Hood, P. J., Lefebvre, D., Paterson, N., Reford, M., & Watson, D. (1991). Guide to aeromagnetic specifications and contracts. *Geol. Surv. Can*, *2349*.

Thompson, D. T. (1982). EULDPH: A new technique for making computer-assisted depth estimates from magnetic data. *Geophysics*, *47*(1), 31-37.

Tolles, W. E., & Lawson, J. D. (1950). Magnetic compensation of MAD equipped aircraft. Airborne Instruments Lab. Inc., Mineola, NY, Rept, 201-1.

Totaro, F., Insinga, D. D., Lirer, F., Margaritelli, G., i Caparrós, A. C., de la Fuente, M., & Petrosino, P. (2022). The Late Pleistocene to Holocene tephra record of ND14Q site (southern Adriatic Sea): Traceability and preservation of Neapolitan explosive products in the marine realm. Journal of Volcanology and Geothermal Research, 423, 107461. https://doi.org/10.1016/j.jvolgeores.2021.107461

Tuck, L., Samson, C., Polowick, C., & Laliberte, J. (2019). Real-time compensation of magnetic data acquired by a single-rotor unmanned aircraft system. *Geophysical Prospecting*, *67*(6-Geophysical Instrumentation and Acquisition), 1637-1651.

UAV Platforms—GemSystems. Available online: https://www.gemsys.ca/uav-platforms/ (accessed on 21 July 2021).

Vacquier, V. V., 1941, Measuring direction or magnitude of magnetic fields or magnetic flux using the flux-gate principle, U.S. Patent 2,406,870.

Vacquier, V. V., 1943, Three-component magnetometers, U.S. Patent 2,555,209.

Veloski, G. A., Hammack, R. G., Sams III, J. I., Wylie, L. D., & Heirendt, K. (2018, October). Evaluation of the Micro-Fabricated Atomic Magnetometer Deployed from a Small Autonomous Rotorcraft for Locating Legacy Oil & Gas Wells. In *Symposium on the Application of Geophysics to Engineering and Environmental Problems 2018* (pp. 202-209). Society of Exploration Geophysicists and Environment and Engineering Geophysical Society. DOI: 10.4133/sageep.31-002

Versteeg, R., McKay, M., Anderson, M., Johnson, R., Selfridge, B., & Bennett, J. (2007). Feasibility study for an Autonomous UAV-Magnetometer system. *Idaho National Laboratory*, 1-53.

Walter, C. A., Braun, A., & Fotopoulos, G. (2019). Impact of three-dimensional attitude variations of an unmanned aerial vehicle magnetometry system on magnetic data quality. *Geophysical Prospecting*, *67*(2), 465-479.https://doi.org/10.1111/1365-2478.12727.

Walter, C., Braun, A., & Fotopoulos, G. (2019, February). Spectral analysis of magnetometer swing in high-resolution UAV-borne aeromagnetic surveys. In *2019 IEEE Systems and Technologies for Remote Sensing Applications Through Unmanned Aerial Systems (STRATUS)* (pp. 1-4). IEEE. https://doi.org/10.1109/STRATUS.2019.8713313.

Walter, C., Braun, A., & Fotopoulos, G. (2020). High-resolution unmanned aerial vehicle aeromagnetic surveys for mineral exploration targets. *Geophysical Prospecting*, *68*(1-Cost-Effective and Innovative Mineral Exploration Solutions), 334-349.https://doi.org/10.1111/1365-2478.12914.

Walter, C., Braun, A., & Fotopoulos, G. (2021). Characterizing electromagnetic interference signals for unmanned aerial vehicle geophysical surveys. *Geophysics*, *86*(6), J21-J32.

Wang, B., Jia, X. T., Liu, J. S., Zhao, G., Sun, X., & Lu, D. (2016). The trial and application of the aeromagnetic system based on unmanned blimp platform. *Geophysical and Geochemical Exploration*, *40*(6), 1138-1143.

Wood, A., Cook, I., Doyle, B., Cunningham, M., & Samson, C. (2016). Experimental aeromagnetic survey using an unmanned air system. *The Leading Edge*, *35*(3), 270-273. https://doi.org/10.1190/tle35030270.1

Xu, Q., Liu, L., Huang, S., & Wu, F. (2020). Research and test of compensation method for cesium optical pump aeromagnetic system of domestic UAV helicopter. *J. Nav. Inst. Aeronaut. Eng*, *35*, 141-148.

Yoo, L. S., Lee, J. H., Lee, Y. K., Jung, S. K., & Choi, Y. (2021). Application of a drone magnetometer system to military mine detection in the demilitarized zone. *Sensors*, *21*(9), 3175. DOI: https://doi.org/10.3390/s21093175

Yu, P., Zhao, X., Jia, J., & Zhou, S. (2021). An improved neural network method for aeromagnetic compensation. Measurement Science and Technology, 32(4), 045106.

ZHANG, F. M., WEN, J. L., ZHAO, X. H., & FANG, W. L. (2019). Development and application of aeromagnetic measurement system for unmanned helicopter. *Progress in Geophysics*, *34*(4), 1694-1699. DOI: 10.6038/pg2019CC0189.

Zheng, Y., Li, S., Xing, K., & Zhang, X. (2021). Unmanned aerial vehicles for magnetic surveys: A review on platform selection and interference suppression. *Drones*, *5*(3), 93. https://doi.org/10.3390/drones 5030093.

Acknowledgements

I would like to express my sincere gratitude to my supervisor, Prof. G. Florio. His guidance, expertise, and support have been the key to my success throughout my graduate studies.

Moreover, I would like to express my appreciation to the other components of the research group, especially to the prof. M. Fedi. His passion for geophysics was contagious.

I would also like to thank the numerous Research Institutes that have helped and provided equipment throughout the field works. This foremost includes: 1) Istituto per i Sistemi Agricoli e Forestali del Mediterraneo (CNR - ISAFOM); 2) Istituto per il Rilevamento Elettromagnetico dell'Ambiente (CNR - IREA); 3) Istituto nazionale di Geofisica e Vulcanologia (INGV), Sezione Grottaminarda; 4) SINTEF.

I would like to thank all the colleagues, components and friends of geophysics research group that have shared with me the past three years (maybe more) and supported my scientific challenges.